DEVELOPMENT OF VISIBLE-TO-ULTRAVIOLET UPCONVERSION PHOSPHORS FOR LIGHT-ACTIVATED ANTIMICROBIAL TECHNOLOGY

A Dissertation
Presented to
The Academic Faculty

By

Ezra Lucas Hoyt Cates

In Partial Fulfillment
Of the Requirements for the Degree
Doctor of Philosophy in Environmental Engineering

Georgia Institute of Technology

May, 2013

DEVELOPMENT OF VISIBLE-TO-ULTRAVIOLET UPCONVERSION PHOSPHORS FOR LIGHT-ACTIVATED ANTIMICROBIAL TECHNOLOGY

Approved by:

Dr. Jaehong Kim, Advisor
School of Civil and Environmental Engineering
Georgia Institute of Technology

Dr. Seung Soon Jang
School of Materials Science and Engineering
Georgia Institute of Technology

Dr. Ching-hua Huang
School of Civil and Environmental Engineering
Georgia Institute of Technology

Dr. Angus P. Wilkinson
School of Chemistry and Biochemistry
Georgia Institute of Technology

Dr. John C. Crittenden
School of Civil and Environmental Engineering
Georgia Institute of Technology

Date Approved: March 13, 2013

To my parents, who gave me everything

ACKNOWLEDGEMENTS

My achievements in graduate school would not have been possible without the outstanding hard work, advice, encouragement, and emotional support of my advisor, Dr. Jaehong Kim. His dedication to his students, research, teaching, family, and desire to help others is humbling, and I could ask for no greater role model. I feel extremely lucky to have worked in his lab and spent the last five years in such a supportive environment where I could grow as a scientist and as a human being. (And thanks for all the dinners, karaoke, and for finding me a wife).

I wish to thank the members of my committee – Dr. Ching-hua Huang, Dr. John Crittenden, Dr. Seung Soon Jang, and Dr. Angus Wilkinson – for volunteering to provide me with guidance on numerous occasions, despite their chaotic schedules. I am especially indebted to Dr. Wilkinson who donated so much of his time to helping me with experiments and discussing ideas, despite the lack of any real obligation to do so, aside from a genuine love of science. He is a truly gifted lecturer whose teachings made it possible for me to succeed in this research.

I would like to express my sincere appreciation to Dr. Guangxuan Zhu for working tirelessly to keep things in the Daniel Laboratory working smoothly, and for keeping everyone safe. I hope I always have someone of his caliber working close by. Also, thanks to Jenny Eaton for her consistent work and dependability as a critical support beam for our entire department.

Special thanks to everyone else who assisted with my research: Dr. Min Cho for training me and making my the first publication possible; Dr. Felix Castellano and Fan Deng at Bowling Green State University for welcoming me into your lab and helping me acquire data; and everyone in the Kim group for all their calming presence and good times in the office.

I am forever grateful to Stephanie, my coworker and soon-to-be wife, for filling both my home life and work life with joy. She has helped me with countless experiments and worked to expand this research into new areas while providing unending support and affirmation.

Finally and foremost, I thank my parents for their sacrifice and hard work, which has enabled me to make it this far.

CONTENTS

LIST OF TABLES

LIST OF FIGURES

ABBREVIATIONS

AM-1.5 – "Air mass 1.5", Optical path length 1.5 times vertical depth of Earth's atmosphere.

AMS – Antimicrobial surface

a-Si – Amorphous silicon

ATCC – American type culture collection

CDC – U.S. Centers for Disease Control and Prevention

cfu – Colony-forming units

CR – Cross-relaxation

c-Si – Crystalline silicon

CSLM – Confocal scanning laser microscopy

CT – Charge transfer

DNA – Deoxyribonucleic acid

DPA – diphenylanthracene

DPSS – Diode-pumped solid state (laser)

DSSC – Dye-sensitized solar cell

$\boldsymbol{E_g}$ - Band gap energy

EQE – External quantum efficiency

ESA – Excited state absorption

ETU – Energy transfer upconversion

HD – Hexadecane

ICP-OES – Inductively coupled plasma optical emission spectroscopy

IR – Infrared radiation

Ln^{3+} –Lanthanide ion

LS – Spin angular momentum/Total angular momentum interaction

NIR – Near infrared radiation

O:F – Oxide:fluoride, *i.e.* RE_2O_3:REF_3 ratio

PBS – Phosphate-buffered saline

PdOEP - palladium(II) octaethylporphyrin

PIB – Polyisobutylene

PLE – Photoluminescence excitation

PLS – Photoluminescence spectroscopy

PMT – Photomultiplier tube

PV – Photovoltaic

QE – Quantum efficiency

RE – Rare earth

REOF – Rare earth oxyfluoride

RNA – Ribonucleic acid

SEM – Scanning electron microscopy

SODIS – Solar water disinfection

TEOS – Tetraethoxysilane, a.k.a. tetraethyl orthosilicate

THF – Tetrahydrofuran

TSB – Tryptic soy broth

TTA – Triplet-triplet annihilation

UC – Upconversion

UC-AMS – Upconversion antimicrobial surface

UVA/UVB/UVC – Ultraviolet radiation subcategories

$\boldsymbol{V_O^{\cdot\cdot}}$ – Oxygen vacancy

x – Stoichiometric value in $RE_xO_{x-1}F_{x+2}$

X2-1500º – X2-Y_2SiO_5:Pr^{3+} prepared by annealing at 1500 ºC

XRD – X-ray diffraction

SUMMARY

Ultraviolet radiation remains an indispensible tool in combating pathogenic microorganisms as a result of its direct mutagenic effects on DNA and lack of harmful or environmentally persistent chemical residuals. Fortunately for all life on Earth, the germicidal UV wavelengths present in sunlight are blocked by the atmosphere; thus, electricity-powered UV lamps are required for application to water, air, or surface disinfection. However, a material that passively emits small quantities of UVC without electricity or devices would allow more widespread use of this tool for protecting public health, particularly with regards to the prevention of fomitic disease transfer in hospitals, food processing, and public facilities. The work described in this dissertation represents the first material development studies dedicated to achieving this goal. A biocidal surface that functions effectively through an all-optical mechanism may not only show distinct advantages over current antimicrobial concepts, but the potential for application to point-of-use water disinfection for the developing world is also a possibility discussed herein.

By utilizing the photoluminescence process of upconversion (UC), phosphor materials that sequentially absorb low energy photons and emit a lesser number of higher energy, anti-Stokes photons may be synthesized. Lanthanide-doped crystalline systems capable of infrared-to-visible UC have thus been the subject of considerable research in recent decades; however, materials that convert visible light into germicidal UV may be engineered using the same fundamental concepts, though no significant research has been dedicated to this task. Using praseodymium as a UC activator, $Y_2SiO_5:Pr^{3+}$ phosphors

capable of emitting UVC upon excitation by blue light were successfully prepared herein and studied using photoluminescence spectroscopy. Initial proof-of-concept surface microbial inactivation and biofilm inhibition studies indicated successful achievement of a light-activated antimicrobial material based on UV emission through UC; however, conversion efficiency and inactivation rate were inadequate for practical application.

Material optimization and development of $Y_2SiO_5:Pr^{3+}$ was conducted through compositional modification, monitored via laser spectroscopy, electron microscopy, and diffraction experiments. Addition of lithium as a codopant was found to significantly enhance UC efficiency. Changes in optical behavior and energy flow were examined in detail and correlated to modifications in crystal structure imparted by Li^+. Several concurrent enhancement mechanisms were revealed and delineated quantitatively. Apart from chemical modification, the effects of different excitation qualities on $Y_2SiO_5:Pr^{3+}$ visible-to-UVC conversion were also investigated using combined polychromatic laser beams. Results indicated that certain visible wavelengths in addition to the violet/blue range were capable of inducing UVC emission under specific conditions; such potential for added efficiency is relevant to the broad spectrum ambient or sunlight excitation in the proposed light-activated antimicrobial surface concept.

Optimization of the $Y_2SiO_5:Pr^{3+}$ system for increasingly efficient UC eventually reached a plateau, warranting development of a second-generation phosphor for UC antimicrobial technology. Due to the unique host crystal restrictions encountered in Pr^{3+} UC materials, originating from ligand-dependent d-orbital excited states of this ion, unconventional oxyfluoride crystals were synthesized by solid state reaction in inert atmosphere and their UC capabilities were studied. One system in particular – Lu_xO_{x-}

$_1F_{x+2}$ – resulted in UC emission that was several times more efficient than $Y_2SiO_5:Pr^{3+}$ with a higher fraction of emitted photons in the germicidal range.

The successful proof-of-concept experiments together with considerable gains in UC efficiency, achieved over a relatively short time scale, demonstrate the strong potential for realizing practical UC antimicrobial surfaces. These studies lay substantial groundwork for advancing technology that may serve to reduce the transfer and occurrence of nosocomial and waterborne infections while providing a sustainable alternative to current methods of sterilization.

CHAPTER 1

INTRODUCTION

1.1. Statement of Problem

Minimizing the occurrence and transmission of pathogenic microorganisms in water, food, and the indoor environment has been of utmost priority to human beings since the earliest civilizations. Despite the application of modern technology, pharmaceuticals, and public health practices, we are still faced with numerous dangerous microbial diseases that are resistant to control strategies. Of particular modern significance is the threat of nosocomial infections involving antibiotic resistant pathogens such as methicillin-resistant *Staphylococcus aureus* [1] and carbapenem-resistant *Enterobacteriaceae* [2]. The Centers for Disease Control and Prevention estimated in 2010 that approximately 1.7 million hospital-acquired infections occur in the United States each year, resulting in 99,000 deaths [3]. Pathogens frequently prevail over control strategies in our food processing and distributions systems, as well. While the microbiological safety of food in the United States has improved over the last decade, over 19,000 food-borne infections were confirmed in 2010 [4] and cases involving the well-known *Salmonella* bacteria have seen no decline over the past 15 years [5]. Furthermore, outside of the developed world, roughly 1 billion people face pathogen exposure due to

the lack of unsafe drinking water, which results in 2 million deaths each year, according to the World Health Organization [6].

In addition to medical, microbiological, and pharmaceutical research, materials engineering is beginning to play an important role in combating disease transfer. Many bacterial and viral diseases are transferred simply via inanimate objects (fomites), such as doorknobs, handrails, and tabletops. Development of material surfaces that possess inherent antimicrobial qualities is a paramount task for controlling nosocomial infections [7], in addition to fomitic disease transfer in the workplace, schools, cruise ships, and other public facilities. Antimicrobial surfaces (AMS's) also have their place in the food industry, wherein packaging materials have been engineered to inactivate microbial contaminants upon contact [8-10]. While the objective is to develop surfaces that deter microbes – in both hospital and food packaging sectors – the specific application to which a material is deployed will determine important specifications, such as strength, durability, and chemical safety.

In regards to water disinfection, material technology has the potential to benefit communities that lack sanitation infrastructure and treatment plants by providing point-of-use disinfection options. One established method of obtaining safe drinking water in areas with insufficient electricity or access to chemical disinfectants is solar water disinfection (SODIS) – a practice that has been actively promoted by the Swiss Federal

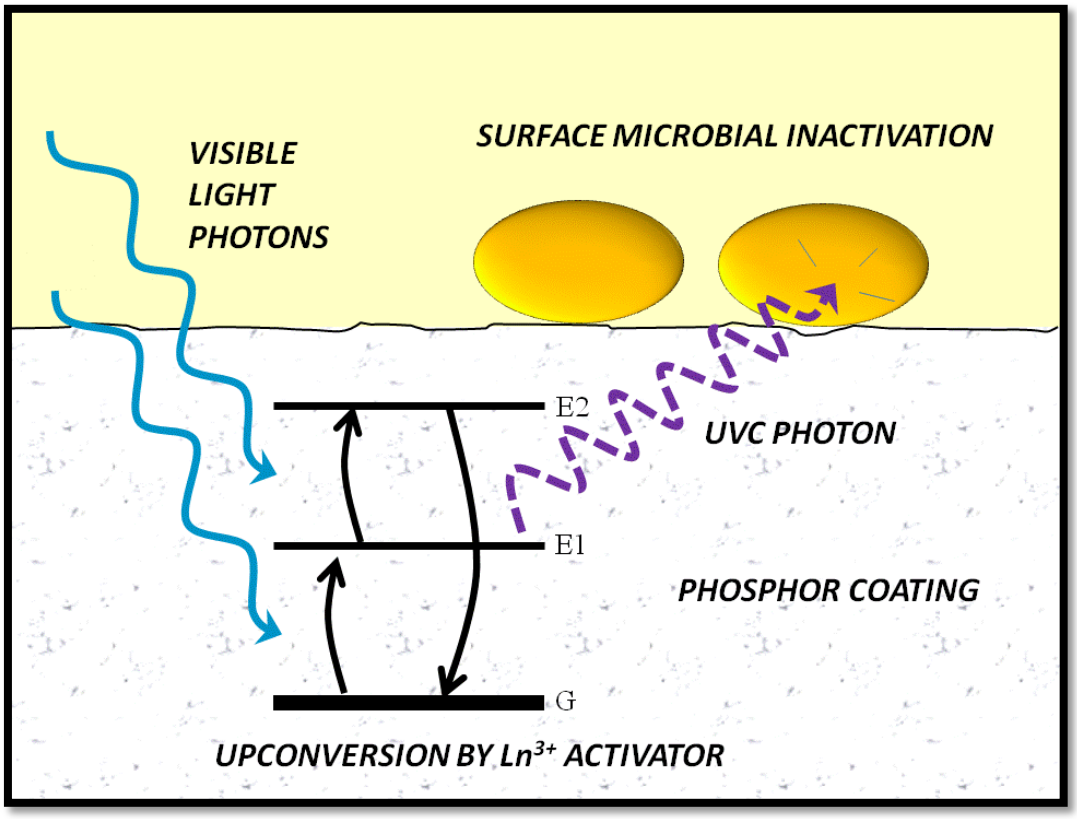

Figure 1. The upconversion antimicrobial surface concept. Reprinted with permission from Cates, E. L., M. Cho, et al. (2011). *Environ. Sci. Technol* 45(8): 3680-3686. Copyright 2011, American Chemical Society.

Institute of Aquatic Science and Technology (Eawag) for preventing diarrheal diseases in the developing world. Therein, water is placed in clear plastic bottles which are positioned in direct sunlight for at least 6 hours, during which adequate log-reduction of key microorganisms is achieved as a result of UVA/UVB exposure [11, 12]. Because of the limiting drawback of long treatment times (particularly on cloudy days or at higher latitudes), the application of photocatalysts to SODIS reactors has been pursued as a means of increasing inactivation rates [13-15]. Thus, development of new antimicrobial material technologies may serve to prevent waterborne diseases, in addition to fomite transmission.

1.2. Research Objective

The research described in the present work was pursued with the intent of introducing and developing a novel form of widely applicable antimicrobial technology. The primary hypothesis resulted through recognizing the need for new AMS concepts and by combining the following principles: (1) UVC radiation is highly effective at inactivating microorganisms; (2) lanthanide-doped phosphor materials can potentially convert visible light into UVC radiation; and, (3) such upconversion (UC) phosphors may be prepared in the form of surface coatings. It is thus hypothesized that a surface consisting of a visible-to-UVC upconversion luminescent coating will inactivate microorganisms upon exposure to visible light. Given adequate conversion efficiency by the phosphor system, this material could function when stimulated by sunlight or ambient fluorescent light, providing a unique AMS that functions purely by optical means, rather

than a chemical mechanism. This concept is referred to hereafter as the upconversion antimicrobial surface technology (UC-AMS), shown in
Figure 1, and is the focus of this work. In addition to the public health benefits of realizing effective UC-AMS, this research serves to advance more fundamental knowledge of visible-to-UVC upconversion phosphors. Unlike the well-studied infrared-to-visible conversion systems, this form of UC is scarcely reported in the literature and its successful application for practical means must be preceded by substantial materials research and development. Because of the intentions to both fundamentally advance a material concept while simultaneously pursuing a specific application, progress herein must be structured to address both of these areas. Objectives include:

1. Synthesize first-generation visible-to-UVC UC phosphors based on existing literature.
2. Establish instrumentation capabilities for conducting photoluminescence spectroscopy of UV-emitting samples.
3. Develop surface coating procedures and appropriate antimicrobial assessment methods.
4. Demonstrate proof-of-concept by observing surface microbial inactivation resulting from visible-to-UVC UC.
5. Establish phosphor design principles and develop of second-generation UC surfaces.

By meeting these objectives, the UC-AMS concept will likely become established as a notable form of AMS and legitimize an expansion of research on this topic by additional researchers working toward successful real world application.

CHAPTER 2

BACKGROUND

2.1. Existing Antimicrobial Surface Technologies

Because of the ability of many microorganisms to cause local infections, systemic disease, material degradation, and biofouling, the application of AMS's spans numerous sectors. In addition to the aforementioned applications of food packaging and hospital surfaces, much research into AMS technology has been devoted to preventing infections related to implantable medical devices, namely catheters [16-18]. Additionally, athletic wear containing antibacterial compounds are marketed to reduce odors [19] and antifungal shower curtains are available for prevention against mildew. Biofouling poses a significant challenge for many industrial processes and is of great concern to the shipping industry, wherein biofilm growth on ship hulls results in considerable drag and increased fuel consumption [20, 21]. The wide variation in utilization of antimicrobial* materials has resulted in several classes of surfaces, each employing different modes of action.

Many AMS's consist of polymer matrices impregnated with a biocidal agent, which leaches slowly from the material. Organic biocides, including quaternary ammonium species [22, 23] and phenolic species, such as triclosan [23, 24], are typical additives, in addition to inorganic agents such as silver ions/nanoparticles [17, 19, 25-27]. Leaching

* *While the term 'antimicrobial' may refer to any effect that discourages microbial residence on a surface, it is used herein to designate biocidal properties, which result in inactivation of the bacteria or viruses.*

surfaces, however, possess three critical drawbacks that make them non-ideal for widespread use. First off, public health concerns arise out of the potential for such AMS's to promote antibiotic resistance and the possibility of harmful effects after human exposure. Triclosan, for example, is known to form carcinogenic dioxin compounds upon photodegradation [28]. Furthermore, environmental persistence of biocidal agents is already well documented, and leaching AMS's contribute to their release into soil and water [19, 28, 29]. Lastly, the mere existence of a leaching mechanism implies a finite supply of active compound within the material – hence, limited longevity and diminished sustainability. Even prior to depletion, the efficacy is limited by diffusion of biocide to the surface; this aspect is problematic in the food industry, wherein the cold temperatures employed in storage can lead to ineffective diffusion rates [30].

Departing from an active biocide release strategy, contact-type AMS's utilize covalently attached chemical moieties on a material surface that interact with microbial cell membranes upon direct contact. Such surfaces most commonly contain long-chain cationic functionalities, such as those in Figure 2, that can weaken cell membranes through ion exchange or cause lysis by "spear-like" penetration [16, 31, 32]. While able to achieve near-complete inactivation in just minutes [31], the surface functional groups are rendered ineffective by any fouling residue that disables direct contact between a microorganism and the surface, including dead bacteria. This aspect was reported in a study by Murata et al. [32], who deduced that poly-quaternary ammonium functionalized surfaces could only inactivate a monolayer of *E. coli*, at most, prior to any cleaning. Overall, the long-term efficacy of this AMS class has yet to be determined.

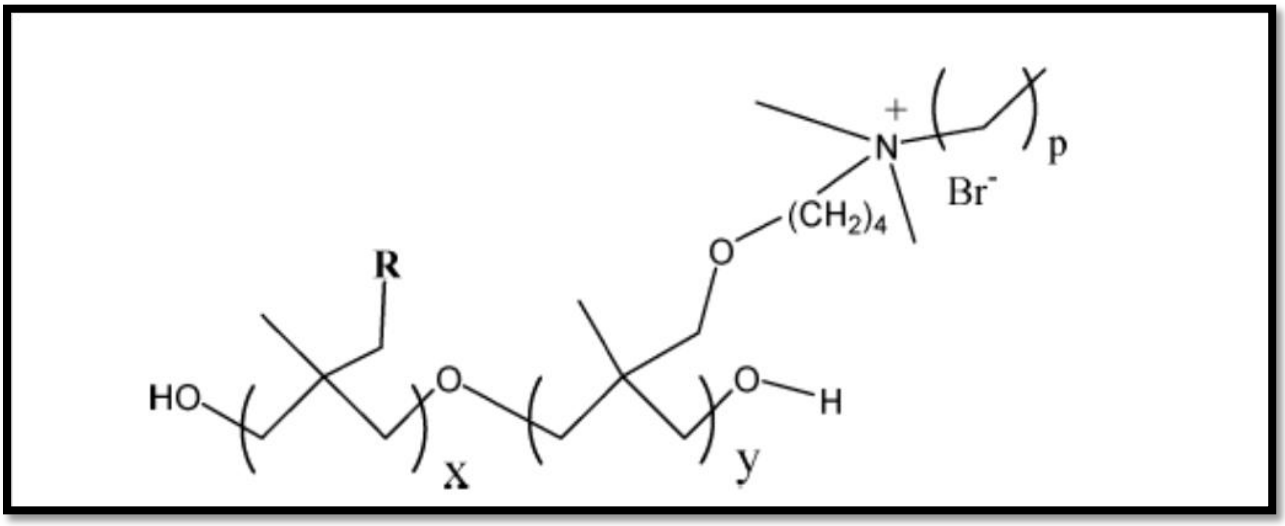

Figure 2. Example long-chain cationic surface moiety for antimicrobial materials. Reprinted with permission from Kurt et al. (2007) *Langmuir* 23(9) 4719-4723. Copyright 2007, American Chemical Society.

Considered the most practically applicable surfaces, metallic copper is the only solid material that the U.S. Environmental Protection Agency has approved to be marketed for preventing disease [33]. The approval and registration allows suppliers to claim 99.9 % bacterial kills within two hours, but in commercial and healthcare settings it must be used in addition to, and not as a replacement for standard cleaning and disinfection [33]. These materials include pure copper metal (99%) as well as a number of registered alloys and may technically be considered leaching surfaces as most studies point to dissolution of copper ions from the surface as the primary mode of action [34, 35]. The ions are then taken up by bacterial cells where they result in membrane damage and lysis, possibly due to Fenton-like production of radical species [34, 36]. Clinical trials have shown that antimicrobial copper is effective in reducing microbial burden on healthcare surfaces such as doorknobs and armrests within several hours during normal usage practices [35, 37, 38]. Nevertheless, there exist many indications that AMS research for public health settings cannot simply conclude with the advent of the antimicrobial copper industry. Weaknesses of copper include reduced effectiveness on under dry conditions, lower susceptibility by spores, lower susceptibility by some bacteria possessing mechanisms for pumping copper ions out of the cell, and protection of bacteria by fouling layers [34, 39].

The final existing strategy for imparting biocidal properties on a surface lies in photoactive materials that produce reactive oxygen species. These surfaces can be the most effective at eradicating microbial burdens, assuming adequate incident light energy belonging to a particular wavelength range is reaching the material. Researchers have

demonstrated the biocidal capabilities of semiconductor photocatalytic surfaces on numerous occasions including both TiO_2 and modified TiO_2 with greater visible light activity [7, 30, 40, 41]. Most such studies employ polycrystalline thin films prepared through simple techniques; while these films preserve the exposed nature of the high-surface area nanoparticles, the resultant surface is fragile and impractical for long-term use. Other light-activated AMS's consist of polymers containing singlet oxygen photosensitizers, which are incorporated through either impregnation or covalent bonding [7, 42, 43]. Upon excitation of the sensitizers, energy transfer to O_2 results in excited $^1O_2$, capable of oxidizing many biomolecules and inactivating microorganisms [44, 45]. Organic photosensitizers, however, may degrade over time due to photobleaching and self-oxidation, leading to reduced efficacy [46, 47].

2.2. Microbial Inactivation by UVC Radiation and Advantages of UC-AMS

In the realm of disinfection technology, UVC radiation ($\lambda < 280$ nm) provides one of the most direct means of inactivating microorganisms. Photons in this range are heavily absorbed by DNA and RNA, causing formation of covalent linkages between nucleic acid components to form a variety of detrimental photoproducts [48-50]. Of greatest significance are pyrimidine dimers (Figure 3), which are formed when cytosine, uracil, or thymine components absorb UVC and bond with one another to create a molecular lesion; if left unrepaired, these mutations prevent transcription and can ultimately lead to cell death [50, 51]. Fluorescent UVC lamps have thus been employed in water disinfection for decades because of the minimal byproduct formation and effectiveness against a wide

range of microorganisms including gram-positive and gram-negative bacteria, bacterial spores, viruses, and unicellular eukaryotes [50]. Oftentimes, the UVC absorption spectrum of microbial DNA is used to indicate the most effective wavelengths for inactivating microbes; however, absorption of radiation does not necessarily indicate inactivation. A more useful graph is thus an *action spectrum*, which plots inactivation efficacy versus wavelength. As an example, Figure 4 shows data obtained by Chen and coworkers, which contrasts the UVC action spectrum of *Bacillus subtilis* spores to the various absorption spectra [48].

Utilization of UVC as the biocidal mechanism in the proposed UC-AMS technology provides distinct advantages over other AMS's described above. Since microbes are inactivated solely by optical means, there is no threat of biocide depletion or environmental contamination. Furthermore, typical biological residues have non-zero UVC transmittances, allowing surface-emitted photons to overcome fouling layers and affect organisms that would otherwise be protected from chemical agents or reactive oxygen species. Also, UC-AMS could potentially be used in conjunction with other antimicrobial mechanisms to create the most effective tool possible for deterring surface microorganisms.

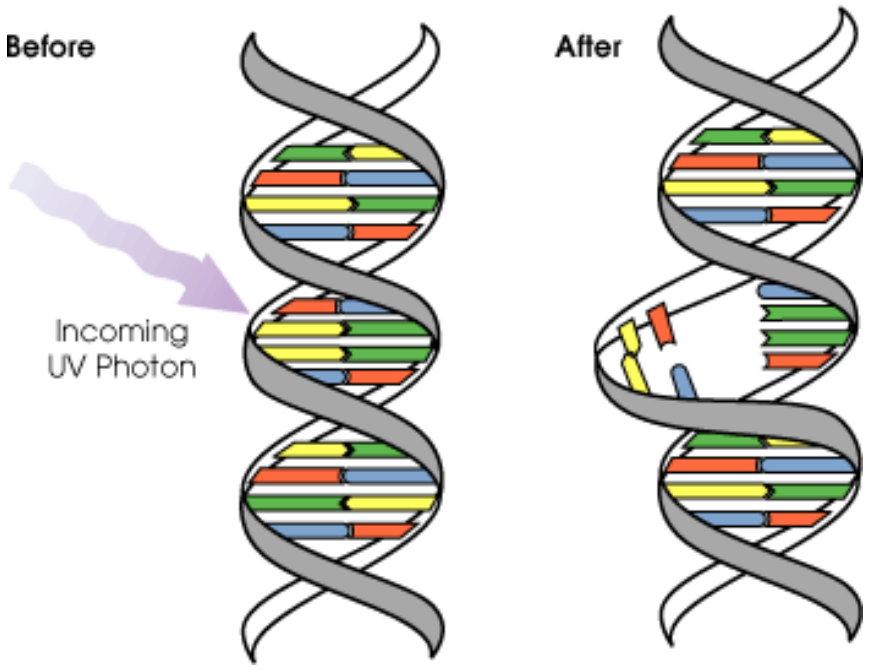

Figure 3. Molecular lesion induced by dimerization of pyrimidine groups upon absorption of UV radiation by DNA. (Image: Public domain)

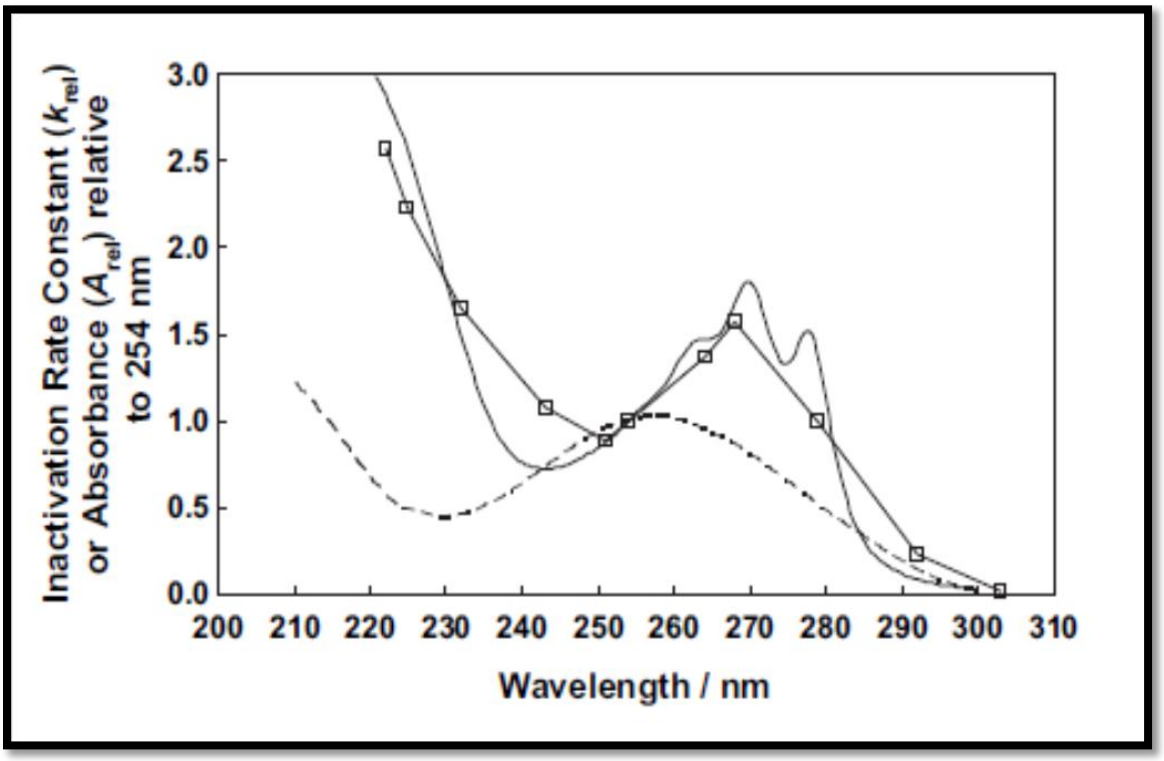

Figure 4. UV action spectrum of *B. subtilis* spores (squares), absorption spectrum of decoated spores (dashed), and absorption spectrum of isolated DNA (solid). Reprinted with permission from Chen et al. (2009). *Water Res.* 43(20): 5087-5096. Copyright 2009, Elsevier.

2.3. Upconversion Photoluminescence

2.3.1. Upconversion Mechanisms in Lanthanide Phosphors

The proposed UC-AMS acts to kill microorganisms by converting visible light into UVC through the unique photoluminescence process of upconversion. Most of the photoluminescence we are likely to encounter obeys Stokes law, in that absorption of excitation light by a material occurs, a portion of the energy is lost as heat, and the emitted photon is always of lower energy and longer wavelength, as shown in Figure 5A. In order to convert low energy photons into higher energy photons, *i.e.* frequency amplification, numerous optical tools have been developed. These include the well-known second harmonic generation and simultaneous two-photon absorption effect – both of which require high intensity excitation by laser beams to be observed to any significant extent [52]. For the purposes of amplifying sunlight or ambient light, a more efficient process that can utilize incoherent, low power excitation is required.

Upconversion refers to a system sequentially absorbing two or more photons, combining their energies, and emitting one higher energy photon [52, 53]. Materials capable of UC reported thus far can be divided into two classes, which rely on different mechanisms: lanthanide-doped inorganic phosphors and organic sensitizer/acceptor systems. In the former group, basic material form involves a transparent crystalline substance – such as a powder, single crystal, or ceramic – that has been doped with optically active ions which are incorporated into the host structure as substitutional defects, depicted in Figure 6. Figure 5B and C show the two simplest forms of UC occurring in inorganic phosphors. The excited state absorption (ESA) mechanism

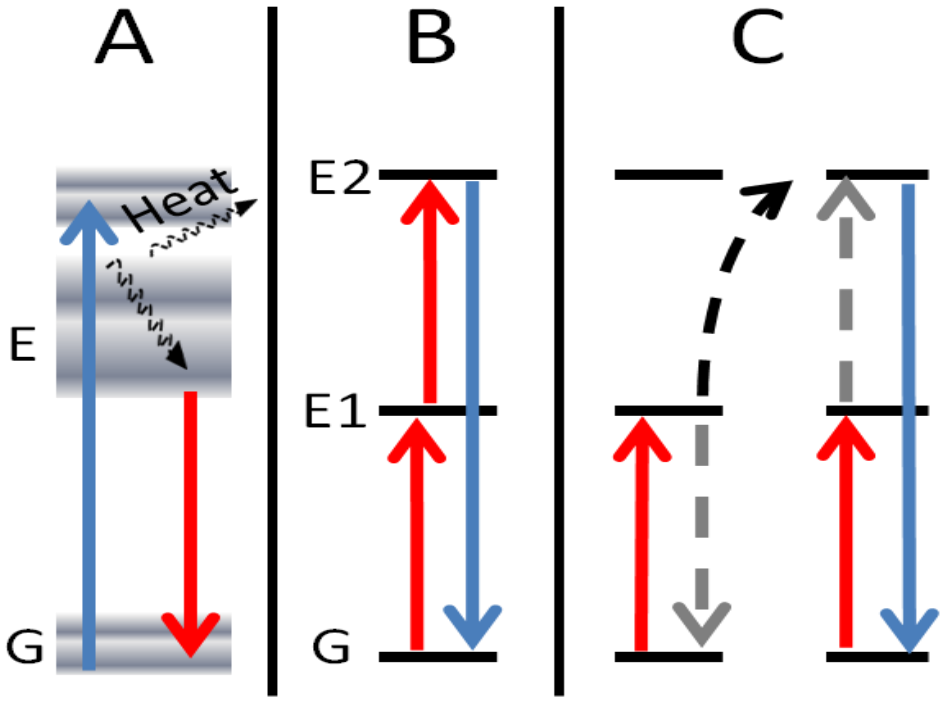

Figure 5. Photoluminescence mechanisms, including (A) Stokes emission, (B) Excited state absorption, and (C) Energy transfer upconversion. Ground state is designated with "G" and excited states with "E". Solid arrows depict light absorption/emission while dashed arrows show non-radiative relaxation and energy transfer. Reprinted with permission from Cates et al. (2012). *Environ. Sci. Technol.* 46(22): 12316 – 12328. Copyright 2012, American Chemical Society.

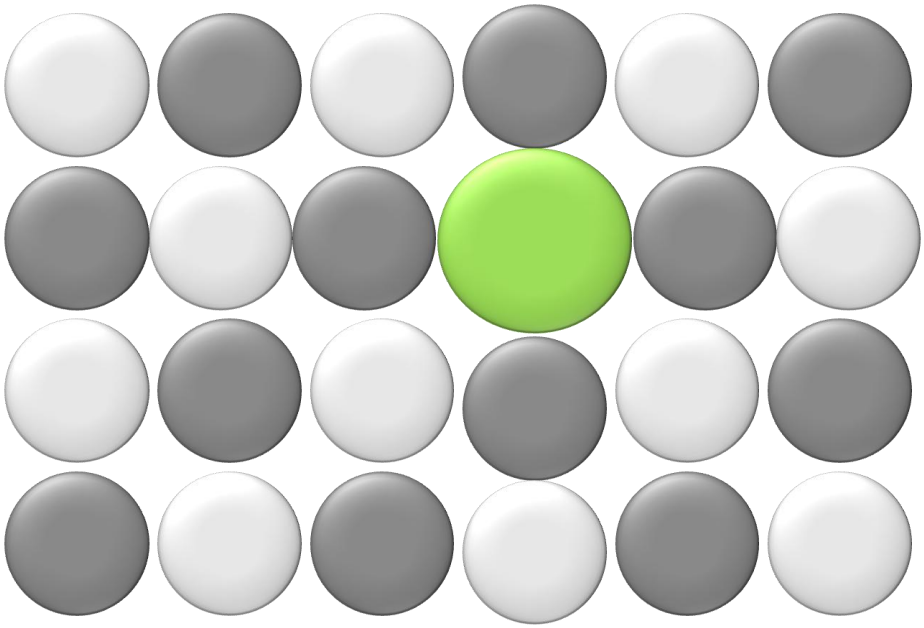

Figure 6. Substitutional incorporation of an optically active ion into a transparent host crystal.

involves sequential absorption of two photons by an ion using an intermediate excited state. Efficiency increases as the intermediate state lifetime increases and, as with all UC mechanisms, emission intensity shows a nonlinear dependence on excitation intensity (two-photon processes show quandratic dependence, three-photon processes show cubic dependence, etc.). The second mechanism, energy transfer UC (ETU), occurs when an ion becomes excited and transfers energy to a neighboring excited ion (on the order of 10^1 Å apart [54]) in the crystal, resulting in relaxation of the donor and double excitation of the acceptor, which then may emit a higher energy photon. This mechanism is more efficient than ESA, since the transfer step may be induced by surrounding ions and does not required a second photon to strike the same ion withinthe lifetime of the excited state [52, 53]. The ability of the optically active ion(s) to sequentially absorb photons or accept energy via long-lived intermediate states in this fashion is critical, as it allows the capture of multiple photons to occur over a longer timescale, thereby permitting the use of low power excitation sources such as sunlight. For this reason, UC phosphors almost exclusively employ lanthanide (Ln^{3+}) ion dopants which have excited state lifetimes in the microsecond to millisecond range[†] [52, 53]. The electron configurations of the trivalent forms of this series may be written in ascending order of distance from the nucleus as $[Kr]4d^{10}4f^n5s^25p^6$. Electrons in the partially filled 4f subshell are optically active and can absorb infrared, visible, and UV radiation to reach many possible excited state configurations. Because the 4f electrons are closer to the nucleus than those in the filled 5s and 5p subshells, they are shielded from crystal field splitting and vibronic interactions

[†] The term lanthanide (Ln^{3+}) is used herein to refer ions with partially filled 4f suborbitals, i.e. Ce^{3+}-Yb^{3+}. The term "rare earth" (RE) typically includes the entire 4f block of the periodic table and the chemically similar Y and Sc. Herein, RE will be used to designate the host cations of Sc^{3+}, Y^{3+}, La^{3+}, and/or Lu^{3+}.

with the host crystal, which would otherwise result in rapid radiative and non-radiative relaxation processes[54, 55]. Furthermore, the reduced perturbation by the host crystal field implies that the Ln^{3+} ions in crystals have 4f electronic states that are relatively discrete and differ little from those of the same ions in a vacuum; thus, the so-called "free ion approximation" of the Ln^{3+} energy levels, shown in Figure 7, may used to show the approximate 4f excited state positions of Ln^{3+} ions in any material [53, 54, 56, 57]. While the energy level spacing and excited state lifetimes of many Ln^{3+}'s are conducive to UC processes, a substantial limitation lies in the parity-forbidden nature of intra-4f transitions, which results in poor absorption of excitation radiation and limits external optical efficiency [58].

2.3.2. History and Applications

While the optical efficiencies of UC processes are generally much lower than those of typical Stokes emissions, copious research over the past 50 years has improved our understanding of the underlying causes of efficiency loss and moved UC out of the realm of solid state physics and into more practical, material applications. Upconversion was first proposed by Bloembergen in 1959 as a means of IR photon counting by converting to visible light using lanthanide-doped crystals; this concept could not be realized, however, until several years later when lasers were used for excitation [52, 59]. Auzel was the first to report the most effective UC activator/sensitizer pair, which comprises Yb^{3+} dopants that absorb IR photons and transfer energy to an Er^{3+} emitter [60], as shown in Figure 8. In 1972, Menyuk et al. reported efficient IR-to-visible UC in

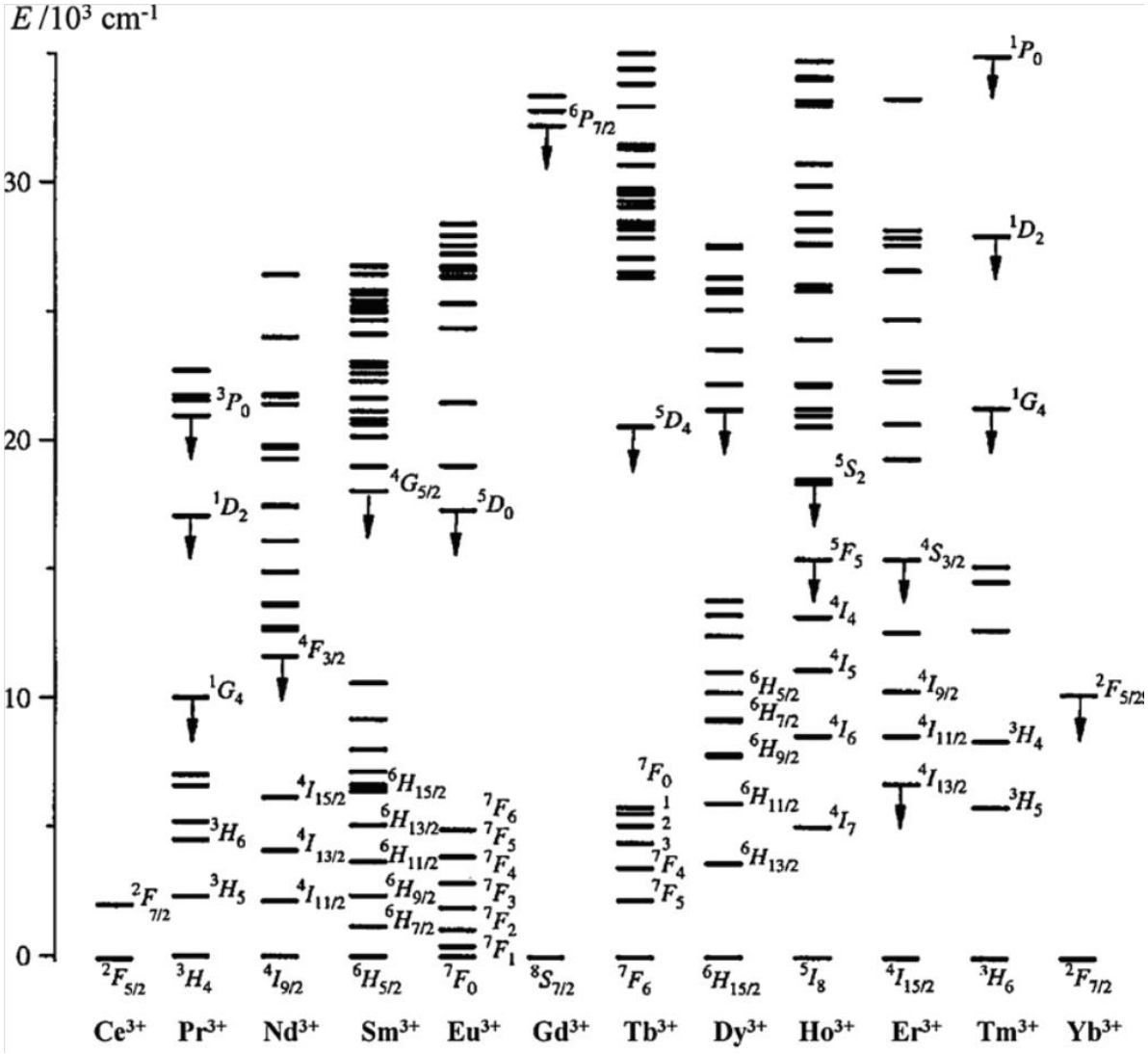

Figure 7. 4f energy levels of the trivalent lanthanide ions. Downward arrows show dominant emitting levels. Reprinted with permission from Aboshyan-Sorgho et al. (2012), *Cooridinat. Chem. Rev.* (15-16) 256: 1644-1663. Copyright 2012, Elsevier.

$NaYF_4:Er^{3+},Yb^{3+}$, which is still regarded among the most efficient Ln^{3+} UC phosphors with conversion efficiencies of up to 4% [61].

To date, the vast majority of research and application has focused on infrared-to-visible conversion. There are three main reasons for this: (i) the advent of compact, powerful fiber diode lasers has made IR, particularly at ~980 nm, the most practical excitation source [53]; (ii) Yb^{3+} conveniently absorbs strongly at this wavelength and provides efficient ETU when used with an erbium activator as mentioned above; and (iii) such phosphors work effectively in biological applications, as they can be synthesized precisely on the nanoscale and IR radiation easily penetrates biological tissues [53, 62, 63]. Thus, research is active in the application of UC nanoparticles to bioimaging, detection, and photodynamic therapy, wherein nanoparticles are surface-functionalized to interact with specific cells or tissues [63-67]. An IR laser source may then excite the particles through the tissue to induce visible light emission that results in imaging or photosensitization. Other applications include use of UC for spectral conversion in solar cells and photocatalysis systems – described in detail in a later section – and finally, UC phosphors are already being employed for anti-counterfeiting in UC luminescent inks [68, 69].

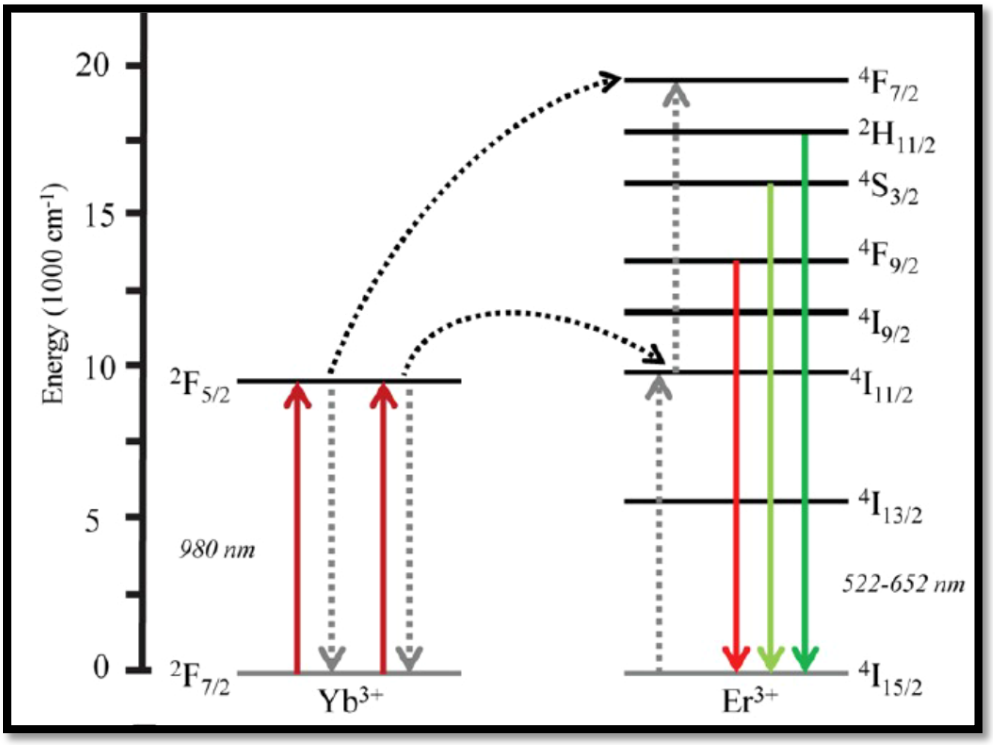

Figure 8. Infrared-to-visible upconversion in the Yb^{3+} sensitizer/Er^{3+} activator system. Reprinted with permission from Cates et al. (2012). *Environ. Sci. Technol.* 46(22): 12316 – 12328. Copyright 2012, American Chemical Society.

2.3.3. Phosphor Design Considerations

Inorganic UC phosphors are synthesized in a variety of forms, including nanocrystal suspensions, nano/microcrystalline powders, and polycrystalline ceramics; however, any UC phosphor can be defined by three parameters: (1) the activators, sensitizers, and codopants employed and their concentrations; (2) the host crystal; and (3) the crystallite size or morphology. The most common naming convention entails listing the host formula followed by the dopant ions as follows: $A_nB_nC_n$:Ln^{3+}. Occasionally, host polymorph and dopant concentrations may also be stated. In designing UC phosphors many material parameters have been shown to significantly affect UC efficiency, summarized below:

Host Crystal – The host crystal determines the crystal field environment of the Ln^{3+} activators and also affects their distribution. One key consideration is the maximum phonon energy of the host as determined by the atomic weights and bonding of the constituent atoms [52-54, 70]. Because the rate constants for non-radiative depopulation of excited electrons are competitive even in Ln^{3+}-doped materials, choosing a host of low vibrational energy increases the lifetimes of intermediate excited states and improves UC quantum yield. In decreasing order of phonon cut-off frequencies, hosts include *oxides* > *oxyhalides* > *fluorides* > *chlorides/bromides*; however, the final class is hygroscopic and thus impractical, making fluorides a preferred class of hosts [53, 71]. Moreover, the ionic radius of the host cation component should be similar to that of the Ln^{3+} dopant(s) to encourage substitutional incorporation into the host structure [54, 72-74].

Impurities – Cations possessing electrons with unpaired spins show strong absorption throughout the optical regime and may interfere with phosphor functionality by absorbing excitation energy and dissipating it in the form of heat [46]. Thus, ions such as Fe^{2+} and Cu^{2+} may exist as impurities in reagent-grade precursors at concentrations high enough to be detrimental to luminescence. For this reason, stock chemicals of at least 99.99% purity are typically used for phosphor synthesis.

Dopant Concentration – The amount of activator and/or sensitizer ions substituted into the cation sites of the host crystal significantly affects photoluminescence and must be finely tuned, depending on the type of Ln^{3+}/host. Low concentrations provide insufficient absorption of excitation photons, whereas excessive concentrations lead to quenching by migration of energy to defect traps [54, 72]. Lanthanide activators are generally most effective at concentrations between 0.1 and 5 atomic percent (% of host cations substituted with the dopant), whereas sensitizers can be effective at 10-20% [54, 75].

Crystallite Size – The surfaces of crystals contain many defects and chemisorbed impurities, namely –OH groups, which may accept energy transfers from excited activator ions due to their high frequency vibrational modes [53, 76-79]. In bulk crystals, the majority of activator ions exist within the interior of the crystal and of sufficient distance from the surface to prevent quenching by surface defects; in nanocrystals, however, a much larger fraction of activators is located within the range of resonant energy transfer of this nature. Resultantly, most UC phosphor materials show lower efficiency when prepared in nanocrystalline form, as opposed to microcrystalline [53, 76-79].

2.3.4. Organic Upconversion Systems

The second class of materials used in frequency amplification utilizes organic and metalloorganic compounds to achieve UC via the triplet-triplet annihilation mechanism (TTA) [80, 81]. This multistep process is shown in Figure 9d and is achieved by combining, in solution, sensitizer and acceptor molecules selected to have excited states with specific energy level spacing and spin multiplicity. First, a sensitizer molecule absorbs a low energy photon to achieve a singlet-to-singlet excitation, followed by intersystem crossing to reach a long-lived triplet excited state. Next, the excitation energy is transferred via triplet-triplet energy transfer to an acceptor molecule which has both a low energy triplet excited state and a higher energy singlet state. Triplet-triplet annihilation between two acceptors then populates the higher energy singlet state, from which a high energy photon may then be emitted through a spin-allowed radiative relaxation. The most effective sensitizers are metalloorganic complexes – namely porphyrin derivatives coordinated to platinum group cations – as these compounds result in exceptionally long excited state lifetimes due to metal-to-ligand charge transfer [82, 83]. Additionally, the excited state energy levels of the sensitizer should be sandwiched in-between those of the acceptor, as in the figure. Given the virtually limitless number of organic sensitizer and acceptor molecules which can be paired, engineered TTA UC systems can perform a variety of conversions, including IR-to-visible [84-87], visible-to-visible [80, 83, 85, 88-96], and visible-to-UVA [94, 97, 98]. Figure 9a-c provides the optical properties and structures of an example TTA system.

When compared to Ln^{3+} phosphors, organic TTA-based UC has both clear advantages and disadvantages. Inorganic phosphors are certainly more robust, arising from the fact that they comprise chemically and mechanically stable, nontoxic solids in the form of powders, ceramics, or composite materials. The TTA approach, however, requires constant intimate, yet mobile, interaction between sensitizer and acceptor molecules and is most effective in toxic solvents which have been purged of oxygen to prevent quenching [93]; this adds considerable difficulty in incorporating TTA systems into materials and devices. Recently, however, solid TTA materials have been made by embedding the lumiphores in rubbery polymer matrices and microparticles [80, 90-96, 99-101]. Furthermore, the anti-Stokes shift of TTA UC emission is relatively small, at 0.2-0.8 eV [81], whereas Ln^{3+} phosphors are capable of nearly doubling or tripling photon energies [70, 102, 103]. Nonetheless, TTA UC clearly dominates with respect to conversion efficiency under low power excitation, with external quantum yields over 1%, as seen in

Table 1. Lanthanide UC materials achieve similar efficiencies under laser excitation [52, 61], but for low power scenarios, conversion efficiency estimates are usually 1-2 orders of magnitude lower [104, 105]. Poor efficacy in this case is attributed mainly to low absorption coefficients rather than inadequate quantum yields. Organic molecules also have the added advantage of very broad absorption bands, when compared to the more discrete intra-4f transitions of Ln^{3+} ions and can typically utilize a wider range of excitation photon energies. However, relevant to the present research, it is unlikely that visible-to-UVC UC can be achieved by organic systems, since effective sensitizers and

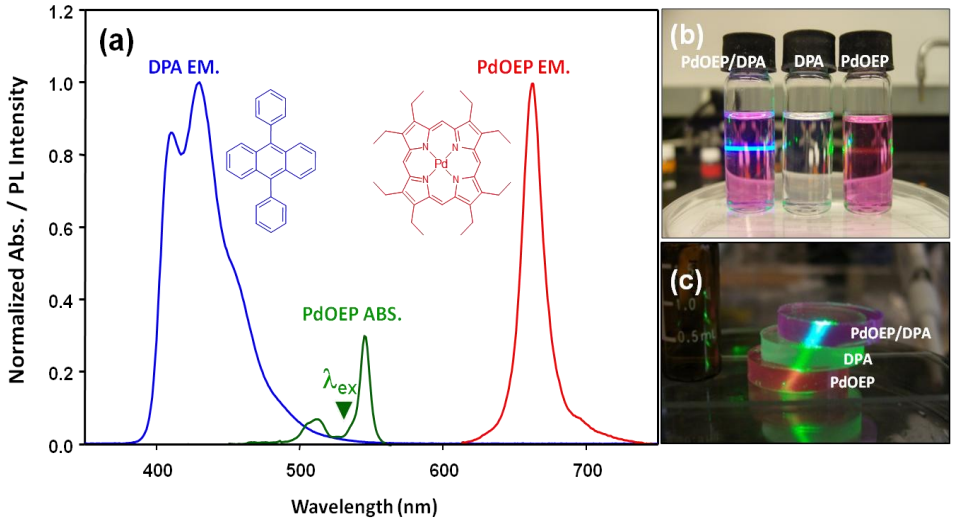

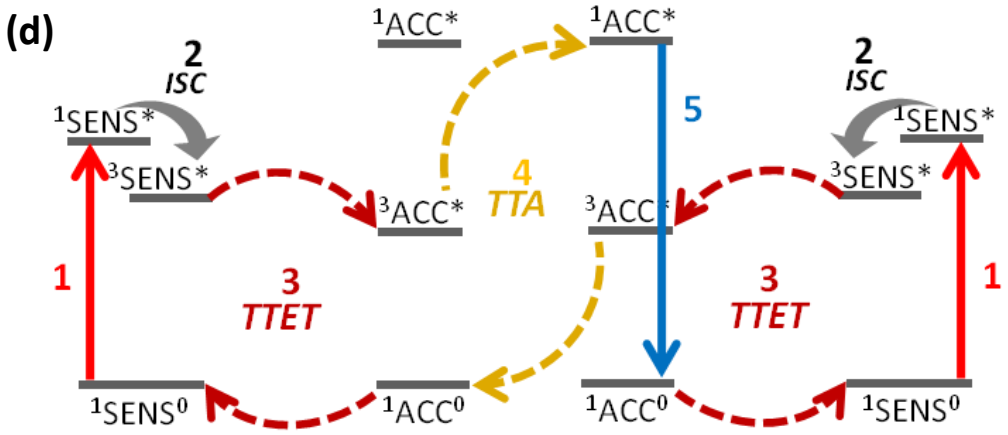

Figure 9. (A) Molecular structure and normalized emission spectra of 9,10-diphenylanthracene (DPA, blue) acceptor and palladium(II) octaethylporphyrin (PdOEP, red) sensitizer, and absorption spectra of PdOEP (green). Right: Photographs of (b) upconverted blue light and downshifted red light emission and (c) emission from rubbery polymer disks containing either DPA, PdOEP, or PdOEP/DPA irradiated by a green laser pointer. Bottom (d): depicts the steps of TTA UC by organic systems including (1) low energy photon absorption, (2) intersystem crossing, (3) triplet−triplet energy transfer, (4) triplet-triplet annihilation, and (5) high energy photon emission. Dashed colored arrows show energy transfer by direct (Dexter) electron exchange. Reprinted with permission from Cates et al. (2012). *Environ. Sci. Technol.* 46(22): 12316 – 12328. Copyright 2012, American Chemical Society.

Table 1. Studies reporting estimated absolute external optical conversion efficiencies of upconversion phosphors. *Ratio of incident excitation and emitted power intensities. **Ratio of incident excitation and emitted photons (EQE). Reprinted with permission from Cates et al. (2012). *Environ. Sci. Technol.* 46(22): 12316 – 12328. Copyright 2012, American Chemical Society.

Reference	Conversion Type	Material	Excitation (W/cm^2)	Conversion Efficiency
Page et al. 1998 [61]	NIR-to-visible	$NaYF_4:Er^{3+},Yb^{3+}$	20	5.5% *
de Wild et al. 2010 [105]	NIR-to-NIR and visible	$NaYF_4:Er^{3+},Yb^{3+}$	1.2	0.05% *
Fischer et al. 2010 [106]	NIR-to-visible	$NaYF_4$	0.2	5.1%**
Cates et al. 2011 [104]	Visible-to-UVC	$Y_2SiO_5:Pr^{3+},Gd^{3+},Li^+$	0.002	0.001% *
Balushev et al. 2008 [107]	Red-to-blue/green	BPEA and $PdPh_4TBP$	0.1	3.2% **

acceptor molecules – as well as the solvents – contain high densities of carbon-carbon double bonds and thus we can expect high UVC absorbances. Even if a system were designed that could achieve such a large anti-Stokes shift, internal absorption would attenuate the emitted photons.

A comparison between material costs of inorganic and organic UC is difficult at the present time, given that TTA-based solid materials and their application are still in their infancy. Many TTA pairs consist of costly, custom-synthesized metalloorganic complexes, yet as with any material, commercial production costs can be expected to be lower. Case in point, production costs of Ln^{3+} UC phosphors can be expected to be quite similar to the phosphors that are commonly found in commercial fluorescent lamps, of which the phosphor coating is responsible for only a fraction of the total cost. Both UC and conventional phosphors contain Ln^{3+} ions, and despite the misnomer "rare earth elements", the members of the lanthanoid family are relatively abundant in the Earth's crust; however, they are difficult to mine and purify [54] and are the subject of recent political disputes [108]. Table 2 summarizes and compares the attributes of inorganic and organic UC systems.

Table 2. Advantages (+) and disadvantages (-) of inorganic lanthanide-doped UC phosphors versus organic TTA UC systems. Reprinted with permission from Cates et al. (2012). *Environ. Sci. Technol.* 46(22): 12316 – 12328. Copyright 2012, American Chemical Society.

Ln^{3+} Phosphors	Organic TTA
+ Chemically stable	- Susceptible to O_2 quenching and photo-damage
+ Durable, solid materials	- Liquid or soft materials
+ Large anti-Stokes shifts	- Small anti-Stokes shifts
- Poor conversion at low powers	+ High conversion at low powers
- Narrow absorption bands	+ Broad absorption bands
+ Established affordable production methods	+/- Production costs unknown
- Contain valuable/ disputed elements	- Contain valuable elements

2.4. Literature Review: Application of Upconversion Materials to Energy and Environmental Technology

2.4.1. Introduction

The capture and utilization of solar electromagnetic radiation by engineered materials is a topic of immense research and continues to reside at the forefront of sustainable technology innovation. Therein, materials are most commonly employed for converting sunlight into electricity via the photovoltaic effect, though there is also great interest in using the photons of sunlight for photoelectrochemical hydrogen production and to catalyze the degradation of environmental contaminants. The materials at work in these processes are commonly semiconductors – most notably Si and TiO_2, for example – which function as electrons are excited from the valence band into the conduction band of the material through absorption of photons with energy greater than the band gap (E_g). Incident photons that have too little energy are thus not absorbed and not utilized (transmission loss) and those with energy greater than E_g dispense of the excess by heating the material, rather than contributing to the intended, more useful energy product (blackbody loss). Large fractions of the incident radiation are thus wasted.

In the realm of photovoltaics, the concept of multi-junction solar cells provides a solution to the problem of spectral mismatch by comprising layers of materials with differing E_g. Higher energy photons are absorbed at the top layer(s), reducing blackbody losses, while lower energy photons are absorbed in subsequent narrow-band gap layers. The resulting increase in maximum theoretical efficiency comes at significantly greater materials and manufacturing costs, compared to the less efficient single-junction cells [109].

Material compositions that are commonly used for double- and triple- junction cells consist of costly or toxic "III-V" elements, including indium, gallium, germanium, and arsenic [110].

Numerous tactics have also been established for enhancing the spectral response of photocatalysts, of which interest has been fueled by the inability of the benchmark material, TiO_2, to produce reactive oxygen species when irradiated with wavelengths longer than 387 nm (3.2 eV). Development of several catalysts with narrower indirect band gaps have resulted, including WO_3, Bi_2WO_6, and Bi_2MoO_6, with E_g = 2.8, 2.8, and 2.6 eV, respectively [111-113]. Other methods include doping of TiO_2 with impurities to induce midgap energy levels [114-120] and coupling of catalysts with narrower (direct) band gap semiconductor sensitizers [112, 121] or organic sensitizers [122, 123]. Absorption of lower energy light, however, implies less available chemical work per photon and lower quantum yields for the intended reactions when compared to the use of high energy photons and wider band gap photocatalysts. For the purposes of environmental application, such as water and air purification, photocatalytic effectiveness is often measured as the rate of ·OH generation; given the redox potential of 2.3 V (at pH = 7) for this radical species formed through the OH^-/O_2 redox pair, use of materials with E_g lower than 2.3 eV theoretically demands multiple photons per ·OH molecule generated and thus relies on more indirect reaction mechanisms. Additionally, the edges of the conduction and valence bands must have potentials more negative and more positive than the potentials of the $O_2^{\cdot-}/O_2$ and $\cdot OH/OH^-$ couples, respectively, which has been shown not to be the case for some modified semiconductors [124].

A much different strategy to more effectively harness broadband light is instead to use UC luminescent "helper materials" to decrease wavelengths of light that would normally be too long. This concept has drawn considerable attraction because it eliminates the burden of spectral matching from the semiconductor itself and transfers this task to a separate material component. Progress in the understanding and improvement of UC materials over the past decade has recently led to an increase in attempts at applying these materials to practical technologies, including solar energy harvesting and environmental application of photocatalysis. While substantial challenges have arisen, interest in wavelength conversion continues to grow due to the potential freedom that could be gained by adjusting photon energy to desired values.

2.4.2. Enhancing Spectral Response in Solar Cells

As mentioned above, a major obstacle to achieving higher efficiencies in solar cells is spectral mismatch, *i.e.*, the inefficient use of broadband solar radiation by the absorbing medium. Conventional single-junction photovoltaic (PV) cells employ crystalline silicon (c-Si), or amorphous silicon (a-Si) in thin film cells, which have E_g's of 1.1 eV (1100 nm) and 1.8 eV (690 nm), respectively. Optical-to-electrical energy conversion efficiency is thus highest when receiving photons with energies slightly above these values, while sub-band gap photons are not utilized and higher energy photons contribute to blackbody losses. The growing field surrounding dye-sensitized solar cells (DSSC's) is also worthy of mention, which typically show poor red/IR response[125]. Recent studies reveal that UC materials can enhance the efficiency of solar cells by

effectively increasing the number of photons of appropriate energy reaching the cell to enable theoretical efficiencies that exceed the Shockley-Queisser limit [109, 126-128]. As shown in Figure 10, an upconverting material can be applied as a backing layer in the cell such that sub-band gap photons are transmitted through a bifacial PV cell and absorbed by the UC layer. Emission from the luminescent layer is then emitted directly, or reflected, into the semiconductor.

Inorganic phosphor materials used in solar cell application research have included mainly fluoride-based crystals doped with an Er^{3+} activator [106, 109, 129-133]. This ion is particularly suitable for solar cell application because it can absorb sub-(Si)band gap radiation at 1500 nm through the $^4I_{13/2}$, $^4I_{9/2}$, and $^4S_{3/2}$ excited states to result in upconverted emissions ranging from 400-980 nm, as seen in Figure 10. Sensitization of Er^{3+} by Yb^{3+} is also highly effective at upconverting ~980 nm radiation for absorption by a-Si (Figure 8)[105, 134-136]. The most widely reported phosphor material for PV backings is nano- or microcrystalline β-$NaYF_4$:Er^{3+} (and β-$NaYF_4$:Er^{3+},Yb^{3+}), as it has already seen significant development and optimization for bioimaging applications [53, 57, 65, 137]. Specifically, the β-$NaYF_4$ host crystal has low phonon energies, thus minimizing non-radiative energy losses [53].

Prototypes of UC phosphor-modified solar cells have provided proofs-of-concept for enhanced spectral response and a summary of these reports is provided in Table 3. Many studies have employed UC-enhanced solar cells excited by IR lasers at intensities that were orders of magnitude higher than that found in sunlight [105, 131, 134, 138]. While significant optical-to-electrical power conversion efficiency (PV efficiency)

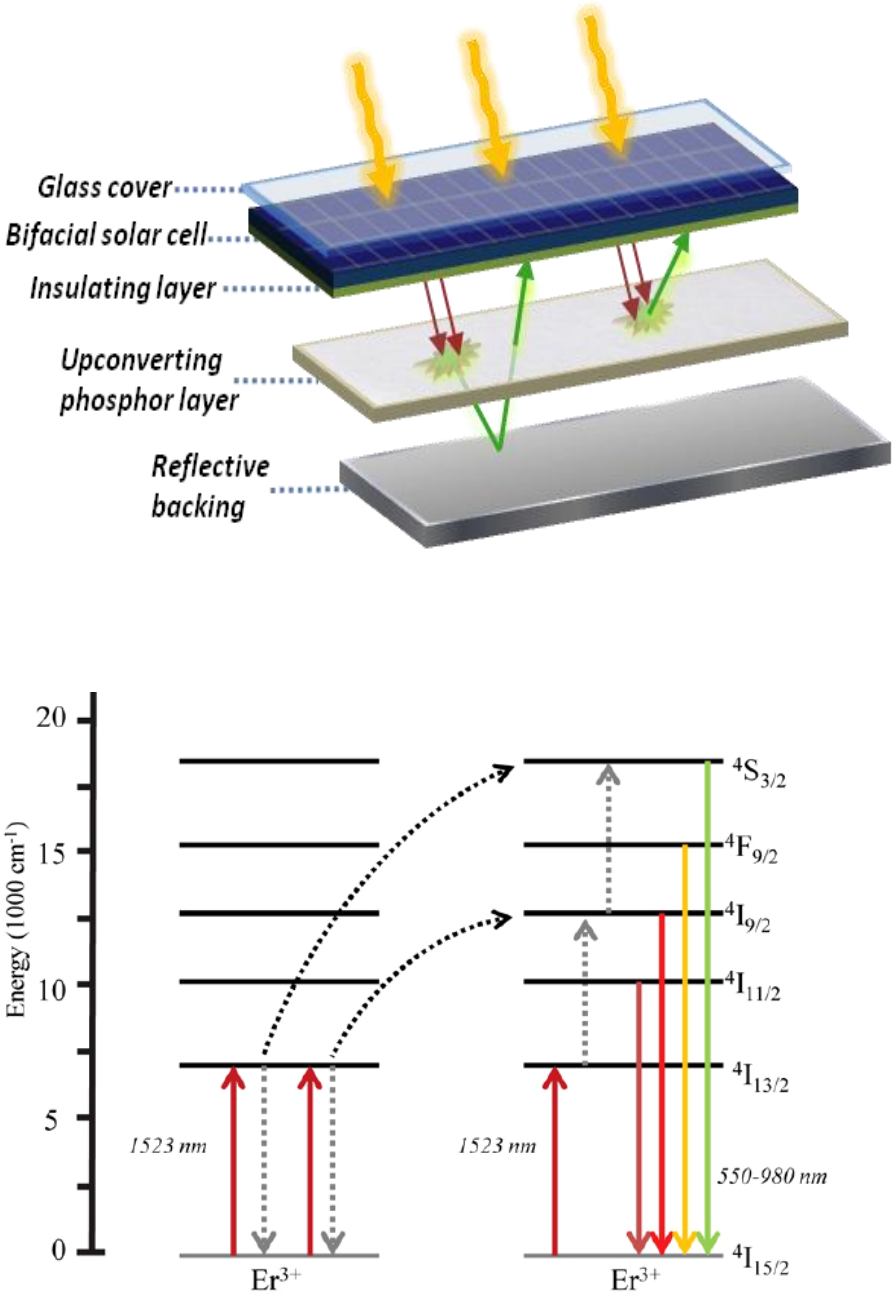

Figure 10. Top: The upconversion-enhanced solar cell concept for utilizing sub-band gap radiation. Bottom: Infrared-to-visible upconversion by Er^{3+}. Reprinted with permission from Cates et al. (2012). *Environ. Sci. Technol.* 46(22): 12316 – 12328. Copyright 2012, American Chemical Society.

enhancements were reported, the nonlinear nature of UC conversion efficiency implies a substantial difference in efficacy between high power (laser) and low power (sunlight) excitation scenarios, making these results somewhat uninformative with regards to practical application. Therefore, the table shows only results obtained using more realistic excitation intensities roughly equivalent to the solar irradiation reaching Earth's surface: ~0.1 W/cm^2. Several of the cited works reported small gains in PV efficiency of less than 1% or no gains at all [105, 106, 131, 135], however, Khan et al. [77], Yuan et al. [136], and Chen et al. [129], reported significant gains of 11.9%, 3.7%, and 8.6%, respectively. Percentage efficiency gains therein are defined as: $\% = 100\% \times [(\eta_{UC}/\eta_0) - 1]$, where η_{UC} is the PV efficiency of the UC enhanced cell and η_0 is the efficiency of the same cell without the UC layer.

A critical review of the methods employed in the three works mentioned above revealed varying degrees of soundness in experimental design. For the study reporting the highest increase in efficiency (11.9%), the UC materials were incorporated into a DSSC that the authors fabricated themselves [77]. Since the experiments therein were not repeated, the variation in efficiency between any two such fabricated cells is unknown, making it difficult to conclude that the observed improvement was due to the UC phosphors. Yuan et al. (also employing DSSCs and observing a median 3.7% enhancement over 5 samples) noted that efficiency of the UC-enhanced cells increased not just for infrared wavelengths, but for visible wavelengths as well, which was attributed to a scattering effect by the phosphors [136]. Hence, a significant portion of the enhancement was not due to UC emission. Chen et al. addressed this issue, however, by employing cells containing undoped $NaYF_4$ as controls and observed a 8.6% increase in

Table 3. Results of Recent Studies Reporting UC-Enhanced Solar Cells under Low Power Excitation sources. *Based on graphical interpretation of published figures. †Enhancements were observed for higher excitation intensities. Reprinted with permission from Cates et al. (2012). *Environ. Sci. Technol.* 46(22): 12316 – 12328. Copyright 2012, American Chemical Society.

Reference	Material	Cell configuration	Excitation	PV Enhancement (η/η_0 - 1)
de Wild 2010 [105]	β-$NaYF_4$:Er^{3+},Yb^{3+}	a-Si cell with spin-coated phosphor/polymer backing layer and rear reflector	~0.45 W/cm^2* 980 nm diode laser	No improvement over normal cell*†
Fischer 2010 [106]	β-$NaYF_4$:Er^{3+}	c-Si with phosphors in refractive index-matched liquid layer and reflective backing	0.11 W/cm^2 1522 nm laser	Achieved an efficiency of 0.34%, vs. 0% w/out UC
Goldschmidt 2011 [131]	β-$NaYF_4$:Er^{3+}	c-Si cell with phosphor-embedded varnish backing layer	Extrapolated for 0.1 W/cm^2 sunlight	Estimated at 0.014%
Khan 2011 [77]	β-$NaYF_4$:Er^{3+},Yb^{3+} core with undoped shell	Dye-sensitized ZnO cell with phosphor particles adsorbed onto electrode	0.1 W/cm^2 solar simulator	11.9%
Li 2012 [135]	β-$NaYF_4$:Er^{3+},Yb^{3+},Gd^{3+} with Au nanoparticles	a-Si cell with phosphors wet-deposited on front surface	0.1 W/cm^2 solar simulator	No improvement† (Supplementary data)
Schulze 2012 [139]	PQ4PdNA/Rubrene in toluene	a-Si cell with UC solution cuvette	720 nm laser equivalent to I_{720nm} of 24 suns	1% (higher with rear reflective bead layer).
Yuan 2012 [136]	β-$NaYF_4$:Er^{3+},Yb^{3+}	Dye-sensitized TiO_2 cell with top phosphor layer	0.1 W/cm^2 solar simulator	3.7%
Chen 2012 [129]	β-$NaYF_4$:Er^{3+}	c-Si cell with glass/phosphor backing and rear reflective layer	0.1 W/cm^2 solar simulator	8.6%

efficiency over the controls[129]. With respect to organic-based UC, Schulze et al. has provided the only demonstration of a UC-PV cell that employs TTA, and reported an enhancement of 2% when relatively high intensity 720 nm NIR radiation was upconverted to visible wavelengths [139].

2.4.3. Enhancing Spectral Response of Photocatalysts

Transmission losses of sub-band gap photons in semiconductor photocatalytic materials present similar efficiency hindrances to PV cells mentioned above, with the most common catalysts requiring UVA radiation to generate electron-hole pairs. Many researchers have thus sought to couple UC phosphors with TiO_2 and other catalysts to enhance their visible light and infrared response for application to sunlight-driven water and air purification (Figure 11). This concept was first reported by Wang et al. in 2005, utilizing a TiO_2/Er^{3+}-doped phosphor mixture to degrade methyl orange dye in solution under visible light, achieving ~45% degradation after 55 h of irradiation at an unspecified light intensity [140]. Feng et al. reported similar experiments in 2008, wherein 12% degradation of methylene blue over 2 h was observed, with the suspensions in close proximity to a 40 W commercial fluorescent lamp [141]. Both of these works performed control experiments using undoped UC host material or TiO_2-only suspensions in order to rule out any degradation by the light source, TiO_2, or phosphor host alone; however, they provide UC emission spectra that may have been artifactual. In the paper by Wang et al., 488 nm light was used to excite a novel amorphous Er^{3+} phosphor (referred to as

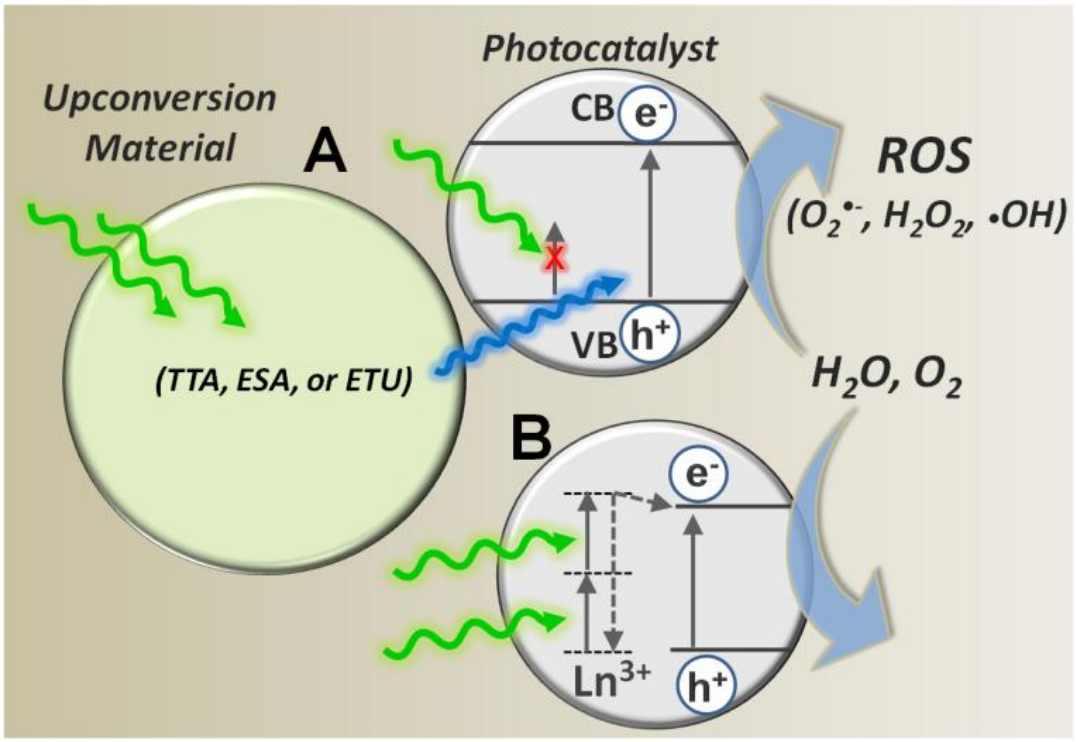

Figure 11. Conceptual diagram of photocatalysis using sub-band gap radiation and assistance by (A) TTA or lanthanide based UC particle or (B) internal UC by lanthanide-doped catalyst. Reprinted with permission from Cates et al. (2012). *Environ. Sci. Technol.* 46(22): 12316 – 12328. Copyright 2012, American Chemical Society.

$40CdF_2 \cdot 60BaF_2 \cdot 0.8Er_2O_3$) and produce upconverted emission in the UV range; however, the theoretical maximum photon energy of 488 nm radiation upconverted by a two-step process can be no greater than – and is typically much lower than – the energy sum of two 488 nm photons, *i.e.* a photon of $\lambda = 244$ nm. Yet, the emission spectrum shows emitted wavelengths less than 230 nm [140]. Furthermore, the emission spectrum of the $Y_3Al_5O_{12}:Er^{3+}$ nanocrystals employed by Feng et al. shows broad peaks that are uncharacteristic of Ln^{3+} 4f→4f emission. The peak locations are inconsistent with detailed spectroscopic studies of the same material in the literature, which also show that most of the emission from Er^{3+} upconversion is in the 400-420 nm range, with only weak emission in the UV region [142, 143]. While laser excitation and high-sensitivity detection systems are the standard for Ln^{3+}- UC research, bench-top spectrofluorometers were employed in both of these works [140, 141].

Criticisms aside, these publications reported successful enhancement of spectral response and initiated an uptick in research pertaining to the integration of UC into photocatalytic systems for utilization of both visible and IR wavelengths. In 2010, Qin et al. used a core-shell technique to synthesize TiO_2-coated $YF_3:Yb^{3+},Tm^{3+}$ particles capable of absorbing 980 nm radiation and emitting characteristic Tm^{3+} UV emission at ~290 and ~350 nm (Figure 12)[144]. For excitation, the group used both a 980 nm laser light source and natural NIR from sunlight (visible and UV light were filtered out and the container was repositioned as the sun moved), along with TiO_2-only and phosphor-only controls. Each excitation source enabled upconversion-induced photocatalytic degradation of methylene blue in solution, with the sunlight experiment resulting in 58% dye degradation after 9 h.

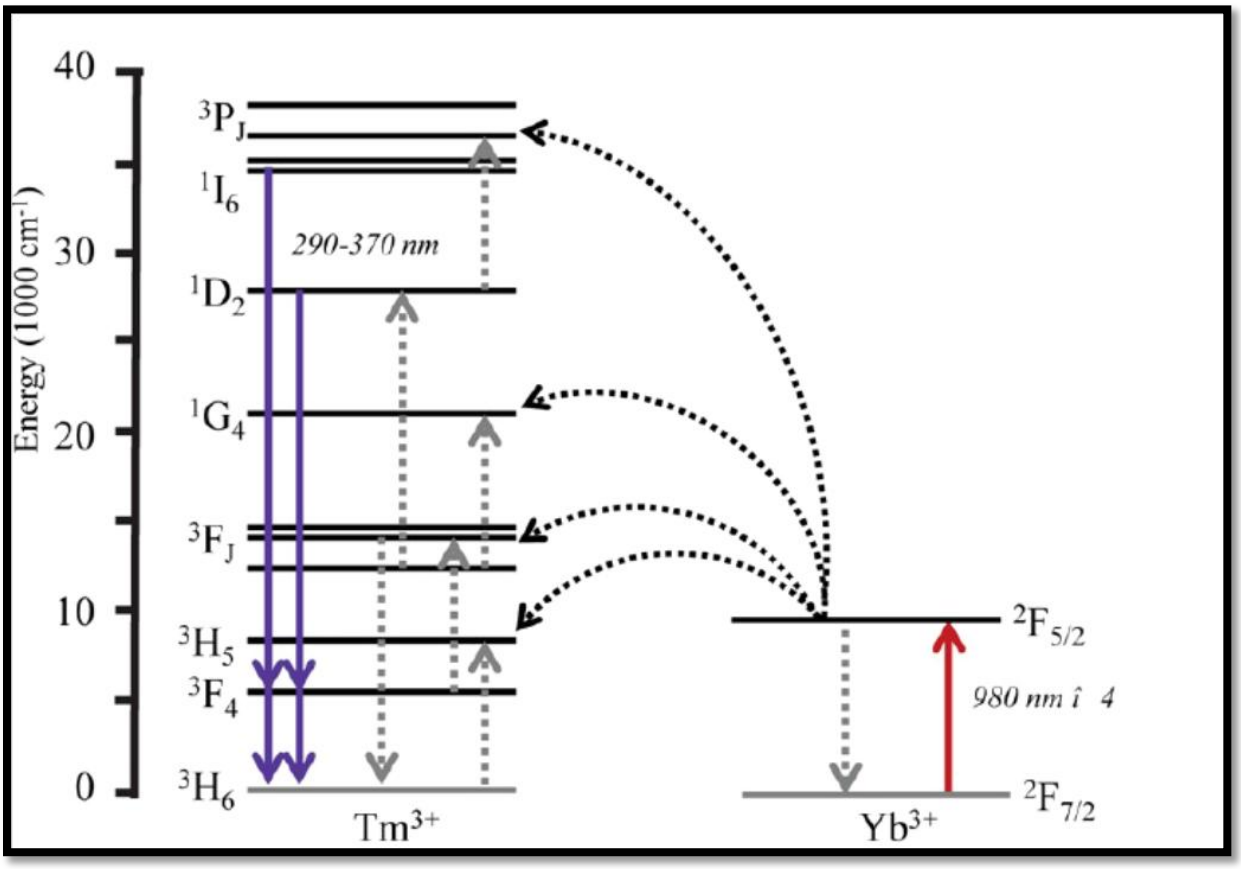

Figure 12. Infrared-to-UV upconversion in the Tm^{3+}/Yb^{3+} system. Reprinted with permission from Cates et al. (2012). *Environ. Sci. Technol.* 46(22): 12316 – 12328. Copyright 2012, American Chemical Society.

Li et al. used a slightly different strategy to activate mesoporous TiO_2 under IR radiation, wherein the catalyst itself was doped with Yb^{3+} and Tb^{3+}, instead of using a phosphor/catalyst mixture[145]. In addition to acting as a UC sensitizer, the presence of Yb^{3+} dopant stabilized the nanostructured mesoporous nature of the material at high temperature and prevented crystallite growth. We note, however, that Ti^{4+} and Yb^{3+} have significantly different ionic radii (0.61 and 0.86 Å, respectively for 6-coordinate [146]) and the authors' claim that the Yb^{3+} doped at 20 at.% was largely incorporated in the TiO_2 anatase structure is not fully supported; the XRD patterns that they measured showed the presence of anatase and absence of Yb_2O_3, but do not rule out the likely presence of a significant portion of amorphous material. The fact that Yb^{3+} also retarded crystallite growth is indicative of its low solubility in anatase, as well, and other works have reported appearance of a pyrochlore phase upon doping TiO_2 with Yb^{3+} [73, 74]. Nevertheless, results of the photocatalysis experiments indicated that internal UC by the Ln^{3+} dopants (illustrated in Figure 11) under 980 nm radiation was capable of generating electron-hole pairs in the TiO_2 and degrading ~45% of rhodamine B in solution after 3.5 h. Excitation intensity in this study was not indicated, but the group employed a 2 W laser diode, which implies very high intensity excitation, barring the use of de-focusing optics. It is likely that intense IR radiation was required to observe any UC, since a nano-sized material with poor crystallinity and dopant incorporation is not expected to be an effective UC host.

This direct doping of catalysts with Ln^{3+} has also been reported by other groups, including the use of $SrTiO_3$:Er^{3+} by Shi et al. to split water under ~0.4 W/cm^2 visible light irradiation from a xenon arc lamp [147]. Still others have studied the visible light

/infrared activity of $Bi_2MoO_6:Er^{3+}$ nanomaterials [113, 148]. While the band gap of this host is 2.6 eV, UC by the Er^{3+} dopant allows additional spectral response in the IR range; under simulated solar radiation, Zhou et al. observed 99% degradation of rhodamine B by $Bi_2MoO_6:Er^{3+}$ after 30 min, versus 67% by undoped Bi_2MoO_6 [113]. They also compared the sunlight-driven degradation of phenol by this material to Degussa P-25 TiO_2, resulting in 75% removal by the UC catalyst and 49% by the P-25 after 120 min.

Direct doping of photocatalyst materials per this method is advantageous in that it eliminates the process of radiative transfer between the phosphor and catalyst particles and simplifies the material system. Furthermore, in the case of TiO_2, doping with ~1% of certain Ln^{3+} species has been shown to enhance catalytic activity, irrespective of UC, by causing slight narrowing of E_g and reducing electron/hole recombination rates [149, 150]. In the previously mentioned studies which employed specific UC activators, however, proper experimental designs ensured that the observed enhancements were in fact due to UC.

In the first report of a UC-enhanced photocatalytic system employing TTA UC, Khnayzer and coauthors constructed a photoelectrochemical cell containing a WO_3 anode capable of absorbing blue wavelengths to achieve hydrogen evolution at a Pt cathode [151]. Incorporated into the cell was a container of palladium(II) octaethylporphyrin (Pd-OEP) and 9,10-diphenylanthracene (DPA) in toluene that absorbed incident broadband light of $\lambda>500$ nm and partially converted it into blue wavelengths through the TTA mechanism. The UC emission was absorbed by the adjacent WO_3 electrode, as clearly evidenced by current density readings that matched the modulation of the green excitation light [151].

The use of TTA UC to achieve sub-band gap photocatalysis by Pt-loaded WO_3 was also reported recently in a communication by Kim et al.[152]. Representing another notable advancement in environmental application of TTA UC, this is the first report of incorporating TTA into an aqueous system, achieved via fabrication of dispersible rigid polymer microcapsules. The ~200 μm capsules consisted of a photo-cured ethoxylated trimethylolpropane triacylate ester shell and a core containing a mixture of hexadecane (HD) and polyisobutylene (PIB). Dissolved within this mixture was a Pt-OEP/DPA sensitizer/acceptor pair that was capable of green-to-blue UC. Remarkably, the authors reported that the core mixture produced efficient UC emission even when exposed to atmospheric oxygen, which was made possible by an unknown consequence of the HD/PIB solvent combination [152]. Photocatalysis experiments were conducted using microcapsules and Pt-WO_3 in aqueous suspensions containing coumarin – the oxidation of which was monitored semi-quantitatively by an increase in the fluorescence signal of the 7-hydroxycoumarin reaction product. This study, together with Khnayzer et al., highlights the recent developments in blue light-activated semiconductor catalysts, and given the existence of efficient green-to-blue organic UC systems [93, 94], coupling of these two technologies is an attractive route for further study.

2.4.4. Challenges

The relatively young field of energy and environmental UC-modified technologies presents exciting possibilities in achieving enhancements of spectral responses. For continued advancement of the field, however, it is necessary to recognize

the unique challenges that exist in using wavelength conversion materials for the purposes described herein. Arising foremost is the issue of poor conversion efficiency under low power excitation, particularly with respect to the more robust Ln^{3+} UC phosphors. The major underlying root cause of this problem is the low absorption coefficients of Ln^{3+} materials originating from two factors: (1) the parity-forbidden nature of the intra-4f electronic transitions; and (2) the low doping concentrations that are necessary in order to minimize numerous self-quenching mechanisms. Several strategies have emerged for designing more efficient Ln^{3+} UC phosphors including core-shell structuring [153-155], field enhancement by metallic nanoparticles [156-158], and codoping [159-161], but these methods do not address this root problem.

In addition to low absorption coefficients, Ln^{3+} ions often show narrow absorption bands and many of the abovementioned works took into consideration only one absorption wavelength in their analysis [105, 135, 144]. Ideally, large fractions of the solar spectrum would be utilized, which exists over a smooth continuum of photon energies; yet in sunlight scenarios UC phosphors can themselves suffer from spectral mismatch. This is a particular flaw in Yb^{3+}-sensitized UC phosphors, the success of which is precluded by the assumption that the majority of the excitation light is resonant with a Stark state of the ion's one and only 4f excited state energy level, *i.e.* ~960-980 nm. Thus, ions containing higher numbers of intermediate states may be more suitable for converting broad spectrum radiation.

In a major breakthrough in improving absorbance by Ln^{3+}-doped materials, Zou et al. recently introduced the concept of dye-sensitized Ln^{3+} upconversion, wherein dye molecules were bound to the surface of β-$NaYF_4$:Er^{3+},Yb^{3+} particles [58]. Capable of

strongly absorbing NIR radiation of ~800-875 nm, the cyanine dye antennae transferred the excitation energy to the Ln^{3+} ions via Förster resonant energy transfer which resulted in a 3,300× enhancement of emission. This strategy not only served to increase the absorbance of the material but also dramatically widened the UC excitation spectrum [58]. This type of UC system has not yet been tested in a solar cell, although the paper was written within the context of this application and rapid expansion of the technique into many areas of UC research might be expected in the near future.

As mentioned previously, organic UC systems are capable of high conversion efficiencies in the low power regime, but achievement of chemically stable, solid-state TTA systems has been elusive. Kim et al. recently reported progress in overcoming this challenge by embedding the UC molecules in a rubbery CLRFLX polymer which was relatively impermeable to oxygen [93]. In addition to obtaining a moldable solid UC material, favorable interstitial diffusion and interaction of sensitizer and acceptor molecules within the polymer matrix resulted in a record-breaking quantum yield of 22%. The aforementioned UC microcapsules created by the same group [152] also demonstrate significant progress in developing practical material forms for TTA UC, though evaluation of the long-term stability of polymer UC materials is currently lacking.

As advances in conversion efficiency continue to push this technology towards critical applicability, further research into engineering considerations is required. Consensus on which is the most effective method of incorporating wavelength conversion into photovoltaics is far from being achieved. Authors have used widely different techniques for fabricating the UC layers, including phosphor-resin composites

[131], glasses [138], and organic liquid systems [139]. Detailed investigations into optimum thickness and placement/integration should also be included in future research.

For photocatalysis enhancement, methods of coupling UC with catalysts deserve further study as well. The aforementioned approach of directly doping catalytic crystals with Ln^{3+} activators is a promising, yet immature area of research. Considering that the catalyst in this case also acts as the UC host, the same detailed crystal structure engineering that has been conducted for phosphors is also warranted herein, in order to optimize UC while preserving catalytic properties. Since the internal UC emission of Ln^{3+}-activated semiconductors cannot easily be observed due to absorption by the host, Stokes luminescence intensity and lifetime of the intermediate excited state could be used as an indicator of optical performance to assist in designing effective materials. Depending on the particular material in question, chemical stability and toxicity also requires attention for any application of Ln^{3+} wavelength conversion to environmental technology. Oxide and oxyanion-type phosphors likely do not present any challenges in this respect, as these materials are of low toxicity/highly stable and are even being explored for *in vivo* bioimaging applications [64]; however, the slightly hygroscopic nature of fluoride phosphor hosts has already incited concerns over long term stability in the context of the lighting industry [162].

Organic TTA-enhanced photocatalysis is largely unexplored, with wide-ranging opportunities for further research existing in suitable photocatalyst/conversion system pairs and effective techniques for coupling UC polymers with catalytic particles. As mentioned, toxicity is a larger concern for this class of UC. Recent literature has not

ignored this aspect and the use of safer solvents, as well as the push toward solid systems, is helping to improve the safety and stability of organic photochemical conversion.

In conclusion, recent research efforts on applying UC materials to energy and environmental technologies have resulted in notable advances. At this stage, successful proofs-of-concept have been reported on all fronts and research in this field may continue to expand to include more detailed engineering tasks and new materials. Such efforts can proceed even as new fundamental advancements in UC materials continue to arise, in addition to more advanced photocatalysts and PV systems. The capacity to combine all these tools, as needed, represents a significant achievement in the ability to manipulate and convert light energy for sustainability purposes. Further application to other environmental technologies is also a real possibility with potential to benefit the developing world, wherein sunlight remains the most prevalent source of energy.

2.5. Literature Review: Optical Properties of Praseodymium

2.5.1. Background on Visible-to-UVC Upconversion

While the vast majority of UC research has focused on converting IR radiation to visible light, a limited number of studies have reported visible-to-UV or IR-to-UV conversion wherein a portion of the observed emission fell within the UVC range. This literature is useful in selecting the most viable material system to pursue for application to UC-AMS. In a 2005 publication, Hai-Gui et al. studied UC of green light by $YAlO_3:Er^{3+}$ and observed an emission peak at 275 nm [163]. They asserted that peak arose

due to population of the $^2H_{9/2}$ level after two-step ESA involving the $^2H_{11/2}$ level as an intermediate; however, the majority of the radiative relaxations from the upper excited state were in the form of lower energy visible or UVA photons [163]. Because of the relatively dense energy level structure of Er^{3+} throughout the visible and UV energy range, many optical transitions are possible and visible-to-UVC conversion by this activator is inevitably an inefficient process.

Unlike Er^{3+}, the first excited LS level of Gd^{3+} lies well above the ground state at ~32,154 cm^{-1} making high-energy radiative transitions highly probable. There also exist several groups of energy levels, at even higher energy, which are capable of producing UVC emission. Cao and coworkers have published numerous reports involving IR-to-UVC upconverison by Gd^{3+} systems with Tm^{3+} and Yb^{3+} acting as sensitizers and ETU involving up to six photons [103, 164-166]. While emitted photons with wavelengths as low as 245 nm were observed [103], in all cases the UVC emission accounted for only a small fraction of the emission when compared to the intensity of the $^6P_{7/2} \rightarrow {}^8S_{7/2}$ Gd^{3+} emission at 311 nm and the UVB, UVA, and visible emission by Tm^{3+}. Additionally, the requirement of four, five, or six photon processes to accumulate sufficient energy for UV emission makes such UC highly excitation intensity-dependent and is likely inefficient in practical, non-laser excitation scenarios.

The final Ln^{3+} ion with which UVC emission has been achieved through a UC process is praseodymium. Visible-to-UVC UC by Pr^{3+} was first reported by Lee et al. in 1984, involving an inefficient cooperative self-sensitization mechanism [167]. Subsequently, Nicolas, Laroche, and coworkers conducted significant research on UV-emitting Pr^{3+}-doped crystals excited by two-step processes with the intent of pursuing

tunable UV lasers; however, to our knowledge, their experiments all involved ground-state absorption of visible light, then ESA of UV photons to achieve upconverted, higher energy UV emission [168-171]. In 2006, Hu, Sun, and coauthors published a pair of papers marking the first report of relatively efficient visible-to-UVC emission by Pr^{3+} through a straight-forward ETU mechanism in $Y_2SiO_5:Pr^{3+}$ single crystals [172, 173]. Shown in Figure 13, the ^3P_J intermediate states absorb visible photons in the blue-violet range and through ETU – or to a lesser extent, ESA – populate the 4f5d band of Pr^{3+} located in the UVC energy range [172, 173]. These experiments employed a Y_2SiO_5 host, which is a highly stable oxide used in a variety of optical and coating applications; however, this mechanism is generally possible for any host material wherein the 4f5d band energy is low enough such that it may be populated by a two-visible photon process. Still, many other host-related factors determine the efficiency of UC by Pr^{3+} in a given host crystal. Figure 14 shows the absorption and UC excitation spectra of $Y_2SiO_5:Pr^{3+}$, indicating that this system can utilize a fairly wide range of visible wavelengths including violet, blue, and cyan.

2.5.2. Phosphor Design Considerations

The energy levels of Pr^{3+} (Figure 13), comprise a large number of 4f states in the infrared to visible range, most of which are split into multiple Stark components. At higher energy, there is a $^1S_0$ state of Pr^{3+} that resides at >40,000 cm^{-1} for most hosts; however, this is not seen in Figure 13 since it is overlapped by the 5d band, hence the term 4f5d band. Because the 5d orbital is located further from the nucleus than the filled 5s and 5p orbitals, it is not protected by the same shielding effects experienced by electrons in the

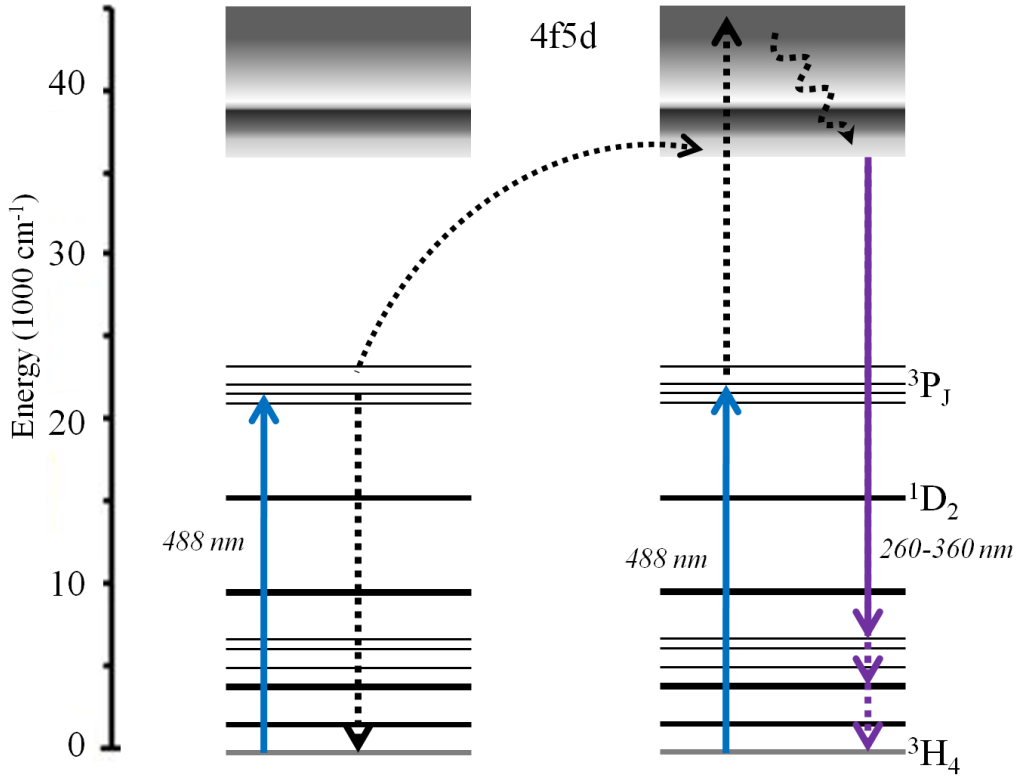

Figure 13. Visible-to-UVC upconversion by Pr^{3+} ETU. Reprinted with permission from Cates et al. (2012). *Environ. Sci. Technol.* 46(22): 12316 – 12328. Copyright 2012, American Chemical Society.

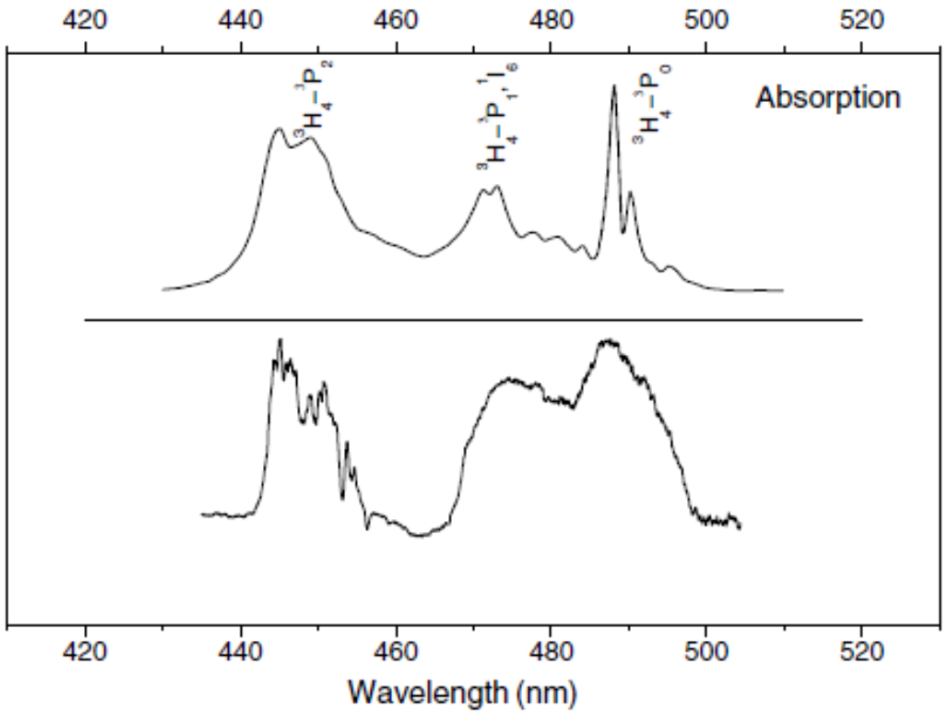

Figure 14. Absorption spectrum of X2-Y_2SiO_5:Pr^{3+} single crystal (top) and two-photon UV excitation spectrum (bottom, λ_{em}=280 nm). Reprinted with permission from Hu et al. (2006). *Chem. Phys.* 325(2-3): 563-566. Copyright 2006, Elsevier.

4f orbital and thus this energy level is heavily split by the crystal field, forming the band structure with a high density of states [173].

Since the electronic levels of Pr^{3+} are well-spaced and exist at infrared, visible, and UV energies, this ion has been studied for use in a variety of phosphor materials. These include long-persistent red-emitting phosphors [174], orange-to-blue upconversion phosphors [175], VUV quantum splitting phosphors [162], and the visible-to-ultraviolet UC materials employed in this research [172, 173]. All of these areas of research have illuminated optical behavior of Pr^{3+} dopant ions that is pertinent to developing UC-AMS. For example, Pr^{3+}-doped materials for emission of red light use emission from the $^1D_2$ states following excitation to the ^3P_J states, which requires rapid $^3P_J \rightarrow {}^1D_2$ non-radiative relaxation. To achieve this rapid relaxation, host materials are used that have a charge transfer (CT) transition with an energy halfway between that of the $^3P_0$ and $^1D_2$ states of Pr^{3+} [174]. This allows back and forth transfer of energy between the Pr^{3+} dopant and host charge transfer state such that energy cascades from $^3P_0 \rightarrow CT \rightarrow {}^1D_2$, with the host acting as an intermediate [174]. On the contrary, such rapid depopulation of the $^3P_0$ state is very undesirable if one wants to achieve UC using Pr^{3+} and host crystals of this type should not be employed. Generally, such crystals contain an oxyanion component with a group IV, V, or VI transition metal, particularly titanates, vanadates, zirconates, and niobates [54].

Additional host-dopant interactions involving Pr^{3+} materials have been elucidated in the development of VUV quantum splitting phosphors. Therein, the goal is to make a phosphor that absorbs one photon of VUV radiation and emits two visible photons, achieving a quantum yield greater than 1, *i.e.* downconversion [162]. Excitation of Pr^{3+} ions into the 4f5d manifold followed by $^1S_0/4f5d \rightarrow {}^3P_J$ emission , then $^3P_0 \rightarrow {}^3H_J$ emission

is one strategy that has been studied by many groups [162, 176, 177]. Thusly, it has been shown that if the edge of the 5d band is of greater energy than the $^1S_0$ state (no overlap), then efficient cascade emission occurs, whereas UV emission is more likely to occur if the 5d band edge lies below $^1S_0$ [162]. This latter scenario is more beneficial to achieving visible-to-UV UC since electrons excited into the 4f5d band would be more likely to relax via UV-emitting transitions rather than sequential visible light emission. High energy Pr^{3+} 5d bands occur for hosts with highly ionic bonds such as fluorides[169] and in fact, in most cases where the $^1S_0$ is of lower energy than the 5d band edge, both levels are too energetic to allow visible-to-UV UC in the first place. This is because initial excitation to the ^3P_J intermediate levels could be achieved using visible wavelengths; however, ESA, which further promotes the electron to the $^1S_0$ or 5d level, would require a near UV photon.

2.6. Acknowledgements

Portions of the background section contain contribution from coauthors and were published in *Cates, Ezra L., Stephanie L. Chinnapongse, Jae-hyuk Kim, and Jae-hong Kim (2012) "Engineering Light: Advances in Wavelength Conversion Materials for Energy and Environmental Technologies."* *Environmental Science & Technology* ***46****(22): 12316-12328.*

CHAPTER 3

DEVELOPMENT OF PHOTOLUMINESCENCE SPECTROSCOPY SYSTEM FOR VISIBLE-TO-UVC UPCONVERSION

3.1. Introduction

Photoluminescence spectroscopy (PLS) is the term applied to instrumentation that includes an IR, visible, or UV excitation source, a sample holder, and a light detection system for obtaining photoluminescence emission spectra. Spectrofluorometers are the most common PLS system found in chemistry laboratories and are defined by their containment of all components into one unit. In more specialized systems, however, the components may not be contained and instead arranged on a breadboard along with the required optics. The study of UC phosphors, in general, requires more specialized PLS systems primarily due to the large amount of background noise. Since UC is by nature an inefficient nonlinear process, the upconverted emission from the sample is of very low intensity compared to the intensity of the excitation beam. Therefore, ensuring that back-scattered excitation photons are sufficiently filtered from the emission beam prior to detection is a priority. Furthermore, thermal noise associated with the high-sensitivity detectors commonly used to study UC is also significant, warranting the use of phase-sensitive detection, as described below. Figure 15 depicts a schematic and photographs

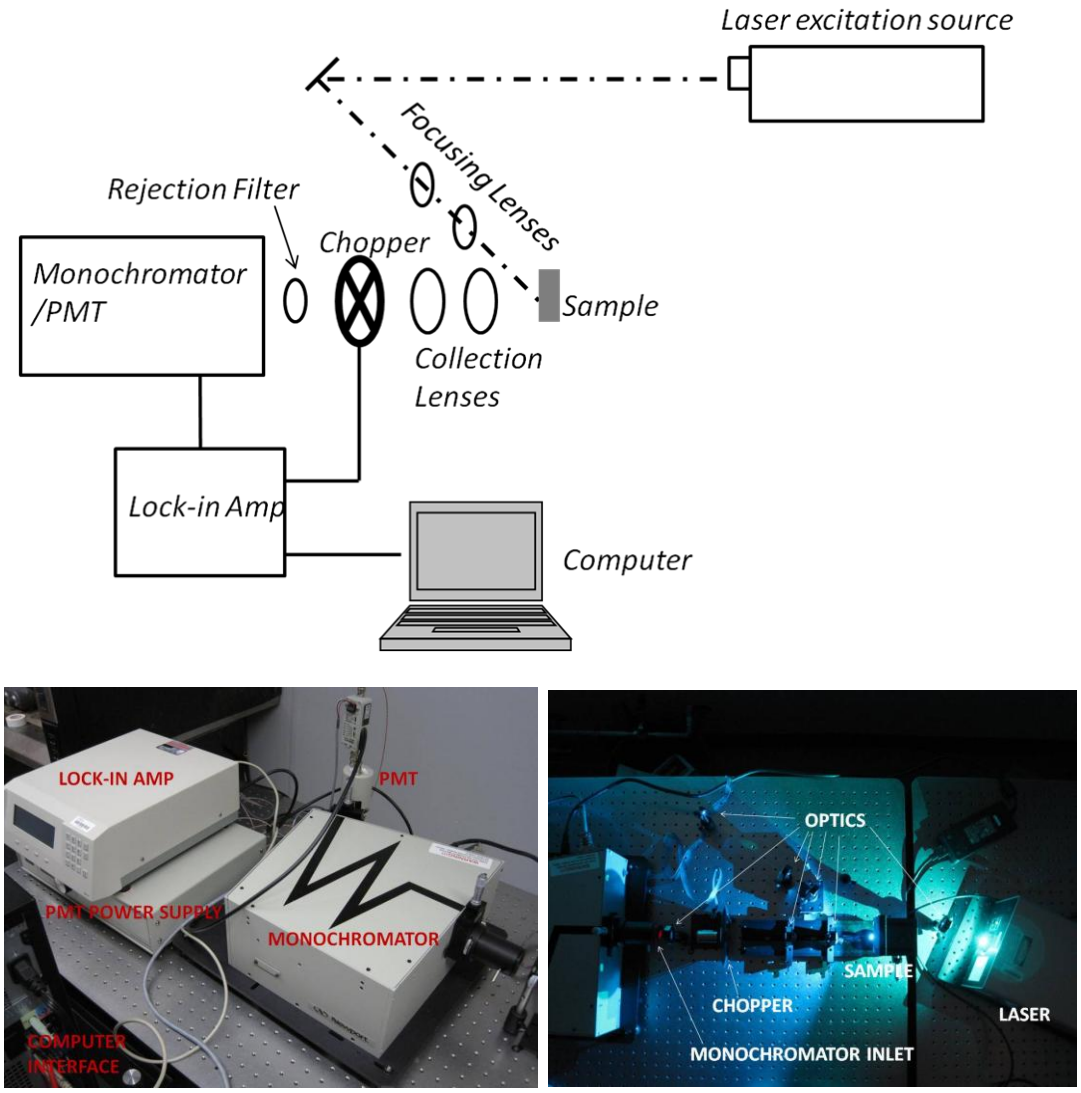

Figure 15. Schematic and photographs of the photoluminescence spectroscopy system for detection of UV luminescence under visible light excitation.

of the PLS system developed for this research and Appendix A lists all of the components and specifications.

3.2. Excitation Sources

As elucidated by Hu et al. [172], visible-to-UVC conversion by Pr^{3+} occurs via the ^3P_J intermediate levels, which have absorption bands at ~442-456 nm and ~468-490 nm (Figure 14). A PLS system for studying Pr^{3+}-activated UC-AMS phosphors should thus include an excitation source within these ranges. The popular xenon lamp sources found in spectrofluorometers provide tunable excitation throughout the IR, visible, and UV range; however, laser sources are preferred for UC research, as the higher power density results in a stronger UC signal [52, 53]. Tunable pulse laser systems allow the most flexibility in PLS capabilities, yet it was decided that a set of fixed wavelength continuous lasers would offer the most cost-effective excitation capability for this research. Hence, sample excitation was typically provided by one of two continuous lasers:

1. ***Argon Ion Laser*** (Stellar Pro-ML, Modulaser Inc.). This air-cooled gas laser had a total output of 1000 mW, with typical argon ion lasing lines. Individual lines were selected through external placement of line filters with the 488 nm and 514.5 nm lines employed in this research. The maximum powers of these components were roughly 200 mW each, making the argon laser the more powerful of the sources used in this PLS system. The beam stability and divergence were also superior to the DPSS laser described below.

2. ***Violet DPSS Laser*** (OEM Lasers Inc.). While an argon laser can excite the Pr^{3+} at 488 nm, this laser's emission fell at the shorter wavelength end of the Pr^{3+} ^3P_J absorption spectrum, at 447 nm. In addition to offering a second excitation wavelength option, this diode-pumped solid state (DPSS) laser was considerably more compact, quiet, and energy efficient than a gas laser. It emitted only one major line, thus requiring no line filters, and had a maximum power of 100 mW.

3.3. Optics and Sample Holder

The laser excitation light was directed to the samples using parabolic or dichroic mirrors and UV-grade fused silica plano-convex focusing lenses. Each mirror employed had a reflectance of only ~90% and thus resulted in some loss of excitation power. Two focusing lenses were placed in the beam path such that the focal point of the final lens was approximately at the sample surface and the beam approached the sample at 45º (detection occurs at 90º). Powder samples were prepared by compacting the powder into the head of a hex screw, which was screwed horizontally (parallel to the floor) into a properly positioned vertical bracket. Ceramic disk samples were positioned simply by placing them upright, facing the detection system on a raised surface. Since exact placement of the sample determines its position relative to the focal point of the final focusing lens, and thus the power density of the incident laser beam, samples were placed in a reproducible manner.

Upon striking a UC phosphor sample, the laser excitation results in omnidirectional emission of UV radiation. Two collection lenses were placed normal to the sample surface to focus a portion of the emitted radiation into the detection system. In this case, fused silica plano-convex lenses with a UV anti-reflective coating were employed, in order minimize signal loss. Prior to reaching the detection system, the condensed emission first passed through a chopper (see below) and one or more short-pass filters. These filters allowed most of the emitted UV radiation to pass through while most of the visible-range photons from backscattered laser light and sample Stokes emission were rejected, thus reducing background noise. Even though the signal was fed into a monochromator, the intensity of the scattered laser light was high enough to overwhelm the monochromator grating, making the use of rejection filters a necessity.

3.4. Detection System

After excitation and emission collection, the UC emission spectrum was analyzed by an optical detection system. Emitted radiation first passed into the monochromator opening, where there was a collimating lens that transformed the diverging emission beam into a collimated beam to allow more effective spectral separation by the monochromator. The emission spectrum was then spatially separated by the monochromator, which employed a MgF-coated grating for more effective throughput in the UV range. The separated emission was then scanned onto the detector slit and entered an Oriel Side-on photomultiplier tube (PMT), sensitive from 160-900 nm. The

current signal from the PMT was converted to a voltage signal by a preamplifier and then connected to an Oriel Merlin signal processor.

Together with the optical chopper (see Figure 15), the lock-in amplifier in the Merlin unit achieved phase-sensitive detection. Therein, the chopper rotates, "chopping" the emission beam so it was modulated with a particular waveform and generally with a frequency of 120 Hz. This modulation makes the emission signal distinct from the thermal noise generated in the PMT and the lock-in amp can extract the signal using a low-pass electronic filter. Signal-to-noise ratio was thus improved by several orders of magnitude, allowing analysis of even weak UC emission. The entire detection system was controlled via a personal computer and TracQ Basic data acquisition software.

CHAPTER 4

UPCONVERSION ANTIMICROBIAL SURFACES PROOF-OF-CONCEPT: SURFACE DEVELOPMENT AND MICROBIAL STUDIES

4.1. Introduction

In proposing a new technology, proof-of-concept demonstration is required in order to move the concept out of the theoretical domain and into the research and development stage. Since a UC-based AMS has never been reported, the first task in pursuing this new class of functional materials is to show that surface microorganisms can in fact be inactivated by visible light that has been upconverted into UVC radiation. Herein, the $Y_2SiO_5:Pr^{3+}$ system reported by Hu et al. [172] (2.5.1) was used as a starting point for material development, as it was seen as likely the most efficient existing phosphor capable of upconverting visible-range photons into germicidal energies. In their work, Hu et al. studied a single crystal, which is impractical for the present application and, instead, powder phosphors offer greater flexibility. However, Zhmurin et al. and Masalov et al. studied Stokes emission in $Y_2SiO_5:Pr^{3+}$ nanocrystals and found that $^1D_2$ emission was less efficient when compared to the bulk material [72, 178]. The difference was attributed to the spatial confinement of the nanocrystals causing clustering of Pr^{3+} ions and higher incidence of detrimental cross relaxation. At this time, the relative efficiency of visible-to-UVC UC in $Y_2SiO_5:Pr^{3+}$ nanocrystals is unknown.

In addition to Pr^{3+} doping, Gd^{3+} co-activation and Li^{+} codoping were explored in the present phosphor development experiments in order to test a variety of phosphor compositions. As mentioned previously, Gd^{3+} is known to emit intense UVB radiation at 311-313 nm via the $^{6}P_{J} \rightarrow {}^{8}S_{7/2}$ transition; moreover, several studies have observed that Pr^{3+} ions in the 4f5d states may sensitize such transitions [179, 180]. In addition, doping with Li^{+}, while not an optically active ion, in certain oxide phosphor systems is known to enhance UC efficiency by Ln^{3+} activators [181-183].

A successful proof-of-concept demonstration of UC-AMS may be formalized as meeting the following three criteria: (1) observation of any measureable surface microbial inactivation; (2) proof that the inactivation resulted from UVC radiation; and (3) the UVC was generated by UC of visible photons originating from an incoherent light source of relatively practical intensity. The final criterion is appropriate due to the nonlinear nature of UC, wherein conversion efficiency is dependent on excitation intensity. Thus, while generation of sufficient UVC photon emission to kill microorganisms may be achieved using laser excitation, such an accomplishment does not provide evidence that the same system would function under sunlight or ambient light scenarios. Excitation sources for the following surface inactivation experiments are thus restricted to commercial compact fluorescent bulbs.

4.2. Experimental Section

4.2.1. Materials

All chemicals were purchased from Sigma Aldrich. Yttrium nitrate was prepared from Y_2O_3 (99.999%) by boiling in 1:1 nitric acid (trace metal grade) and evaporating to dryness in an oven at 104 ºC. Any dopants were also added at the same time as HNO_3, with appropriate amounts of 0.2 M aqueous Ln^{3+} dopant solutions and 1 M $LiNO_3$ (99.999%) while a stoichiometric amount of Y_2O_3 was omitted. For Li^+ doping, Y^{3+} was omitted at 1/3 the molar amount of Li^+. Aqueous stock solutions of Pr^{3+} and Gd^{3+} (0.2 M) were prepared from $Pr(NO_3)_3 \cdot 6H_2O$(99.99%) and $Gd(NO_3)_3 \cdot 6H_2O$ (99.99%). Tetraethoxysilane (TEOS, 99.999%) was the silicon source and gelling agent. All water was purified on a Millipore ultra-purification system.

4.2.2. Powder Phosphor Synthesis

Optical properties of the UC phosphors were studied mainly by use of nano- or microcrystalline powder materials prepared via sol gel decomposition. Sol gels were made by converting 5.3 g of Y_2O_3 to the anhydrous nitrate form (with dopants) and then dissolving in 17.25 mL of ethanol (200 proof) and 5.4 mL of water. A stoichiometric amount of TEOS was then added, followed by an additional 10 min of stirring. The solutions in beakers were heated at ~70 ºC until a clear gel formed. The gels were placed in an oven at 104 ºC for 17 h to form a tacky xerogel, which was ground to a powder with mortar and pestle and placed in alumina crucibles. The samples were heated to 1000 ºC at a ramp of 8 ºC/min in a muffle furnace with air atmosphere and held at 1000 ºC for 3 h, then cooled naturally down to room temperature. Dopant concentrations were adjusted to optimize upconversion efficiency, which corresponded to 1.0 mol % Pr^{3+} and Gd^{3+} for

samples without lithium and 1.2 mol % Pr^{3+} and Gd^{3+} for samples with Li^{+}. Upconversion emission was optimized at a Li^{+} concentration of 7.2 mol %. The resulting powders appeared off-white for samples without Li^{+}, while the samples with Li^{+} were bright white with a light greenish tint attributed to the Pr^{3+}.

4.2.3. Coating Procedure

To coat substrates for antimicrobial testing, 12.7 mm × 12.7 mm (0.25 in^2) silica glass squares were first roughened with 150-grit sandpaper and washed clean. They were then dipped manually into a sol solution prepared in the same manner as the sol for the powder phosphors except that it was stirred gently overnight and then aged for an additional day. One side of each square was wiped clean and the film on the other side was allowed to dry for 1 h at room temperature and then 1 h in an oven at 104 ºC. They were then transferred to a furnace and heated in the same manner as the powder phosphor.

4.2.4. Characterization

Stokes emission spectra were obtained by preparing 0.3% (w/w) phosphor powder suspensions in ethanol via sonication and analyzed on a Shimadzu spectrofluorometer equipped with xenon arc lamp. Upconversion emission spectra were obtained with an argon laser (Stellar Pro-L-ML, Modulaser Inc.) and the PLS system described in Chapter 3. Unactivated Y_2SiO_5:Li^{+} powder was used to obtain a background spectrum, which

was subtracted from all sample spectra. X-ray diffraction analysis was performed on the as-made powder samples in a Scintag XGEN-4000 diffractometer using Cu Kα radiation. Scanning electron microscopy (SEM) of lithium-doped powders was performed with a JEOL JSM-6490LV SEM at 15-20 kV after sputter coating the samples with gold for 30 s. For imaging of non-lithium-doped powders and surface coatings, a JEOL JSM-6500F Field Emission SEM was used at an accelerating voltage of 5 kV.

4.2.5. Biofilm Growth and Imaging

Pseudomonas aeruginosa PAO1 was grown in tryptic soy broth (TSB) at 37 ºC. Cells were harvested by centrifugation at 1000 g for 10 min and washed twice with phosphate-buffered saline (PBS; pH 7.0). A PAO1 suspension was prepared by resuspending the cell pellet in 50 mL of PBS. Biofilms were grown in a Centers for Disease Control and Prevention (CDC) reactor (Biosurface Technologies Inc., Bozeman, MT). The CDC reactor contained four rods that each held three glass coupons. Phosphor-coated and control glass samples were affixed to two of these rods, on opposing sides. An overnight culture was prepared by incubating PAO1 in 1/10 diluted TSB for 20 h at 37 ºC. The sterile reactor was inoculated with 3.5 mL of an overnight culture that had been added to 350 mL of 1/100 diluted TSB. The initial PAO1 population in this batch medium was about 10^6 colony-forming units (cfu)/mL. Two "cool white" 13 W compact fluorescent bulbs were placed on opposite sides of the reactor, in line with the outward-facing samples, and UV filters were placed in between (cutoff <400 nm) to block any UV produced by the bulbs. The reactor was operated in batch mode for 24 h at 100 rpm and

room temperature. After the 24 h, the reactor was connected via a nutrient feed line to a carboy containing 1/300 diluted TSB and was operated in the continuous-flow mode at a flow rate of 11.67 mL/min for 24 h. In order to evaluate cell membrane integrity, the BacLight Live/Dead bacterial viability kit (L-7012; Molecular Probes) was used. The kit contains Syto 9 and propidium iodide to differentiate between cells with intact membranes (live) and membrane-damaged cells (dead), respectively. The stain was prepared by dilution of 3 μL of each component into 1 mL of distilled water. Biofilm samples were imaged with a Leica AOBS-SP2 confocal laser scanning microscope (CLSM; Leica Microsystems Inc.). A water immersion objective lens (63 by 0.9 numerical aperture) was used. The optimum photomultiplier setting was determined in a pre-experiment, and then the same photomultiplier setting was used for all untreated and treated samples. When these preparations were analyzed, at least 2000 cells were scored per sample. The image stacks collected by CSLM were analyzed with MetaMorph software (Molecular Devices Corp.) and Imaris software (Bitplane). Each type of differently doped phosphor surface was analyzed in triplicate to ensure reproducibility, though digital images were only saved for one of each sample type; however, each set of triplicates yielded similar biofilm results.

4.2.6. Surface Inactivation

Bacillus subtilis ATCC 6633 spores were prepared and enumerated as in previous works [184]. Coated glass coupons were sterilized by germicidal UVC lamps for several minutes, and then 50 μL of 3×10^7 cfu/mL spore suspension in 10 mM phosphate buffer

solution was pipetted onto each sample and allowed to dry for 2 h. Samples were placed in open Petri dishes and a glass UV filter (cutoff <400 nm) was used to cover the dish, which was placed 3 cm beneath two 30 W Life-glo2 fluorescent bulbs (Hagen Corp.). The bulbs and immediate area were kept cool with a small fan. For each data point, at least three coupons per sample type were removed at each time increment and assayed via the spread plate method. Spores were recovered from the coupons by placing the samples in a Falcon tube containing 10 mL of phosphate buffer and vortexing for 1 min. To estimate external optical efficiency of the coated samples, the blue light output of the fluorescent bulbs used in biological experiments was measured at the appropriate distance by use of a radiometer with "blue light safety detector", showing response from 400 to 520 nm and peaking at 460 nm (Solar Light Company, Inc.). This response provides good coverage of the Pr^{3+} two-photon excitation spectrum as reported by Hu et al. [172], which has bands from ~440-460 nm ($^3H_4 \rightarrow {}^3P_2$) and ~470-495 nm ($^3H_4 \rightarrow {}^3P_1, {}^1I_6, {}^3P_0$). The intensity of germicidal UV emitted in the direction of the deposited microorganisms was estimated from a dose response curve for *B. subtilis* spores. These data were obtained from a bench scale collimated beam apparatus with low-pressure UV lamps (4 × 4 W, Philips Co.), which introduces nearly monochromatic UV light into the experimental reactor. Bacterial spore suspensions of 10^6 cfu/mL were pipetted at 50 μL per sample onto sterile 1 × 1 cm glass slides, dried, and then placed under the collimated beam. The organisms were recovered and assayed in the same manner as the UC coated samples. The UV intensity was controlled to 0.3 mW/cm^2 and was measured with a radiometer with UV 254 detector (UVX radiometer, UVP Co.). Ultraviolet dose (millijoules per square centimeter) was calculated by multiplying the average light

intensity at 254 nm (milliwatts per square centimeter) and exposure time (seconds). A linear regression was fitted to the linear portion of the dose-response curve to estimate UV dose as a function of inactivation.

4.3. Results and Discussion

4.3.1. Phosphor Development

SEM analysis of the $Y_2SiO_5:Pr^{3+}$ powder doped at 1.0 mol % revealed aggregated small crystallites of ~25 nm, shown in Figure 16. The room-temperature UC emission spectrum under 488 nm excitation is shown in Figure 17 and is in agreement with past studies on commercial $Y_2SiO_5:Pr^{3+}$ laser crystals, wherein 255-360 nm radiation is emitted via the two-photon excitation process described above [172, 173].

To maximize the observable antimicrobial action, the UVC emission was improved by lithium codoping, which has been shown to enhance upconversion in oxide phosphors due to a number of structural effects [160, 161, 182, 185, 186]. In this case, a 7.5-fold increase in overall integrated UC emission peak area and a 14.0-fold increase in UVC emission were observed at an optimized 7.2 mol % doping concentration and were attributed to changes both at the local activator centers and in the surrounding phosphor lattice. First, X-ray diffraction analysis showed that Li^+-free samples exhibited the

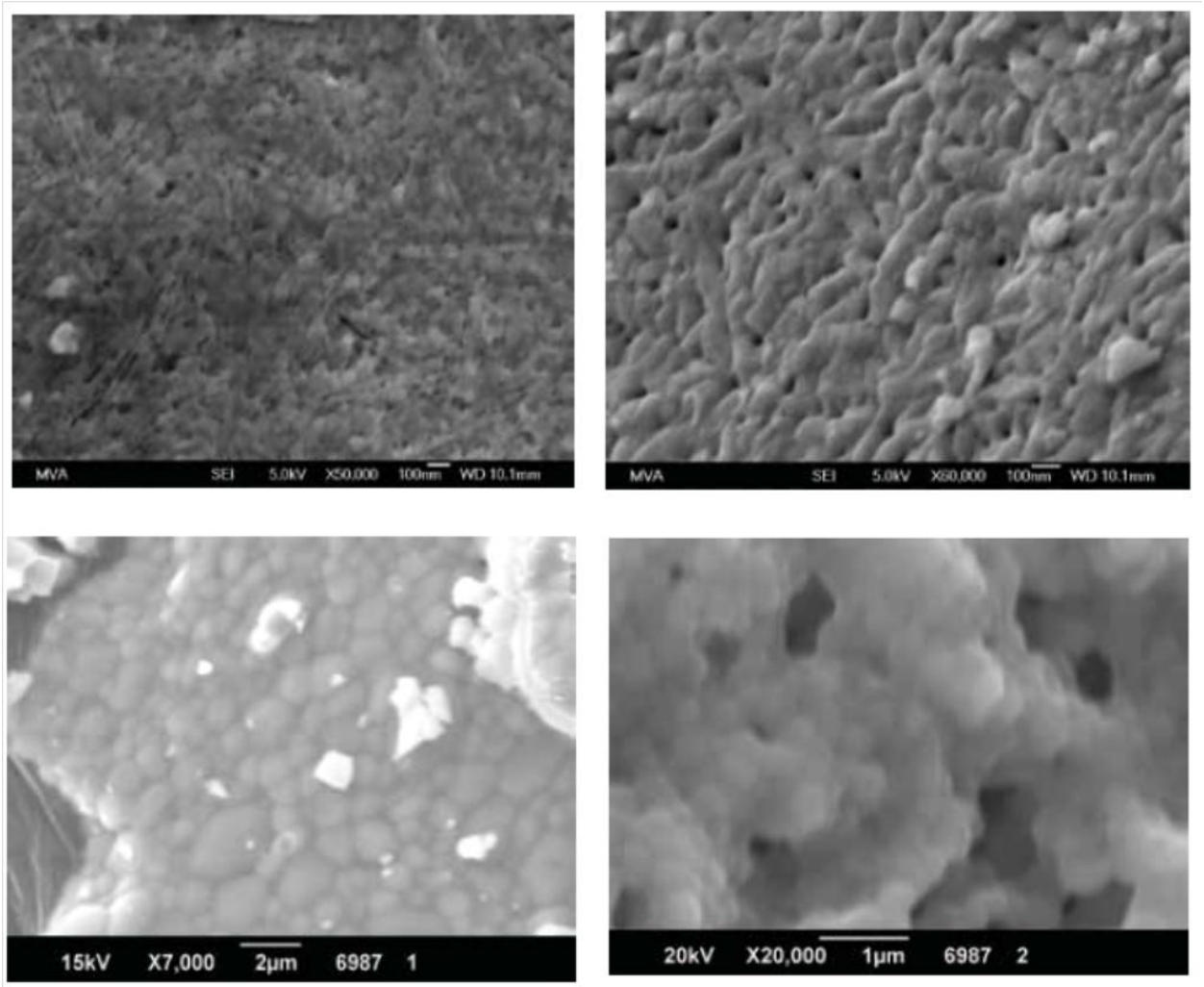

Figure 16. Scanning electron micrographs of Y_2SiO_5 powders with different doping schemes. Clockwise: Pr^{3+}; Pr^{3+}/Gd^{3+}; $Pr^{3+}/Gd^{3+}/Li^{+}$; Pr^{3+}/Li^{+}. Reprinted with permission from Cates et al. (2011). *Environ. Sci. Technol.* 45(8): 3680-3686. Copyright 2011, American Chemical Society.

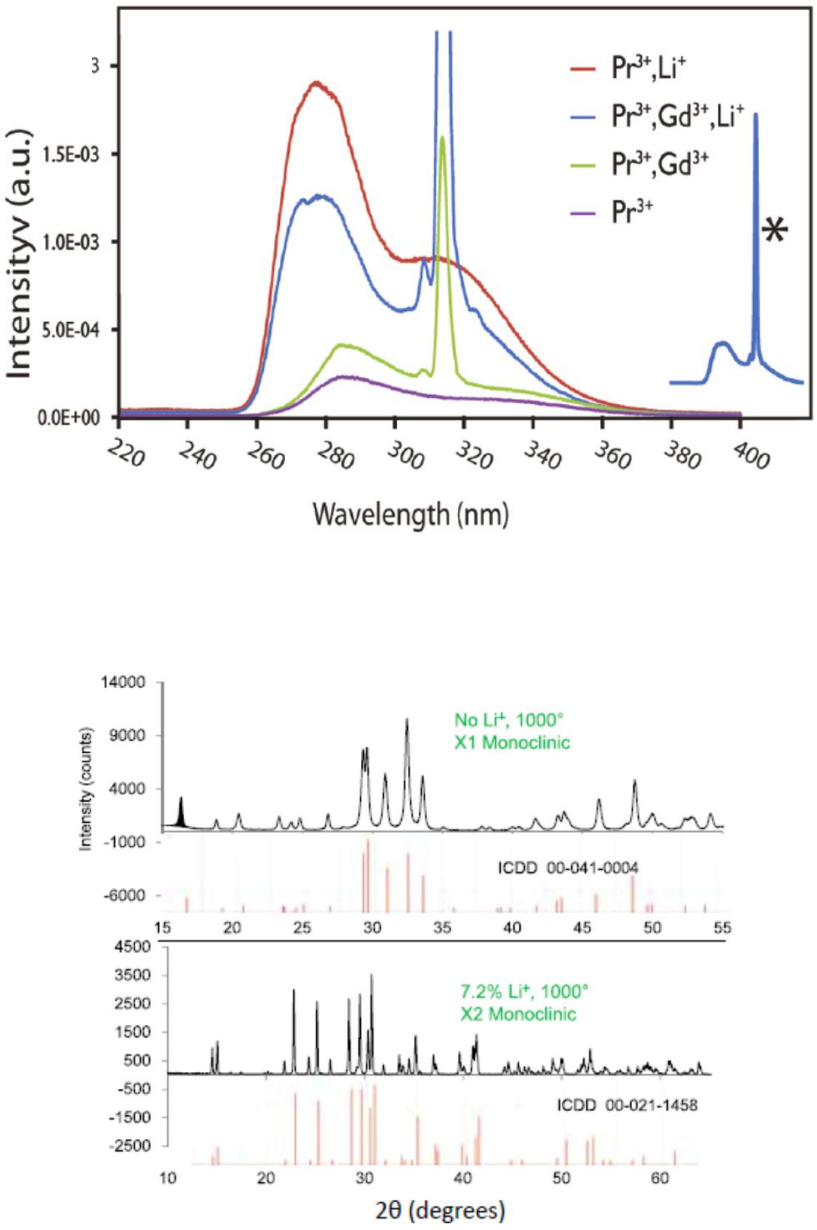

Figure 17. **Top**: Upconversion emission spectra of $Y_2SiO_5:Pr^{3+}$ phosphor powders with various codopants under 488 nm laser excitation. Inset (*) shows zoomed-out view of $Y_2SiO_5:Pr^{3+},Gd^{3+},Li^+$ emission to show height of UVB peak. **Bottom**: X-ray diffraction patterns of Y_2SiO_5 powders with and without Li^+ doping. Reprinted with permission from Cates et al. (2011). *Environ. Sci. Technol.* 45(8): 3680-3686. Copyright 2011, American Chemical Society.

expected X1-Y_2SiO_5 monoclinic phase structure [187], while the Li^+-doped version was of the X2 phase (Figure 17). With all samples annealed at 1000 ºC, well below the formation temperature of the X2 phase [187], this result was unexpected; however, it is speculated that the optically preferred nature of this structure arising from lower Y^{3+} site symmetry,[188] as well as similar asymmetry induced by the Li^+ intercalation itself, may allow greater $^3H_4 \rightarrow {}^3P_J, {}^1I_6$ transition probabilities. Second, Li^+ doping induced the formation of much larger crystallites of 1 μm or greater, as seen in Figure 16. Most literature supports a positive correlation between crystallite size and upconversion efficiency caused by a higher ratio of internal dopants to surface dopants, the latter of which can effectively relax nonradiatively through energy transfer to vibrational surface functionalities.[189, 190] Similarly, in other studies, reductions in phonon- correlation between crystallite size and upconversion efficiency caused by a higher ratio of internal dopants to assisted losses have been speculated to arise from decreases in OH defects upon Li^+ doping [182, 191]. The presence of both symmetry effects and reduction of vibrational loss is also evident herein from the emission spectra obtained under direct excitation by UV radiation (Figure 18), which show that Stokes emission is also improved with Li^+ presence but to a much lesser extent. The differences in degree of emission enhancement exist because directly excited 5d $\rightarrow$4f emission will be improved by reducing phonon-assisted relaxations through larger crystallites and OH reduction, while symmetry distortion will have much less influence than it will on the parity-forbidden intra-4f electric dipole transitions required for the UC mechanisms. Greater integrated peak area in these phosphors' emission was also accompanied by a blue shift in the UVC emission peak of 885 cm^{-1} (from ~285 to ~278 nm), implying a higher energy

5d manifold in the Li^+- doped powders. This is attributed to lower covalency of the Y/Ln-O bonds in X2-Y_2SiO_5, in contrast to the X1 polymorph, which is more greatly influenced by the nephelauxetic effect [192]. Such a shift is welcomed in our case as this places the emission peak further into the action spectrum of radiation-induced DNA dimerization.

Additional codoping experimentation revealed that gadolinium can have a beneficial effect on emission when doped in equimolar proportion to the Pr^{3+} activator and adds an additional peak at 314 nm, as seen in Figure 17. This sharp UVB emission clearly arises from transfer of energy from photoexcited Pr^{3+} to Gd^{3+} and subsequent $^6P_J \rightarrow {}^8S_{7/2}$ intra-4f transitions, as has been reported previously in fluoride crystals [179], and is depicted in Figure 19. Under direct excitation at 255 nm by xenon lamp, the Pr^{3+} Stokes emission is diminished upon Gd^{3+} inclusion since energy is diverted away from excited Pr^{3+} centers to populate Gd^{3+} excited-state levels (Figure 18). However, under 488 nm excitation, the material showed 67% increase in Pr^{3+} UC emission when codoped with Gd^{3+}, the exact reason for which is currently unknown. Conversely, in conjunction with Li^+, coactivation with Gd^{3+} served to detract from UVC upconversion emission, similar to the Stokes emission results. In summary, ascending order of upconverted UVC emission intensity from different doping schemes in the powder phosphors is: Pr^{3+} only (1% doping) < Pr^{3+} and Gd^{3+} (1%, 1%) < Pr^{3+}, Gd^{3+}, and Li^+ (1.2%, 1.2%, 7.2%) < Pr^{3+} and Li^+ (1.2%, 7.2%).

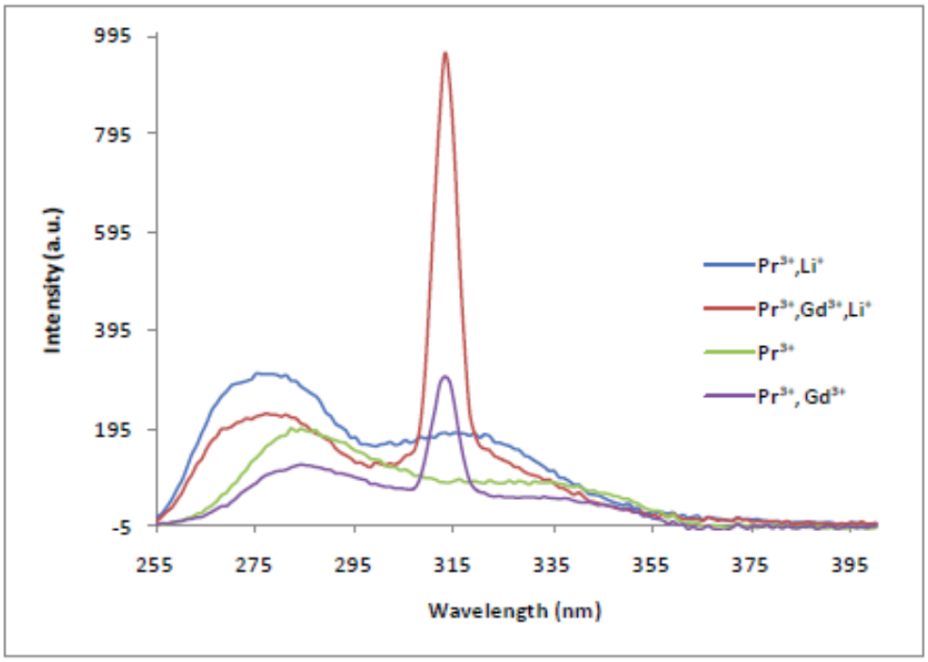

Figure 18. UV Stokes emission by Y_2SiO_5 phosphors under 250 nm excitation by xenon arc lamp. Reprinted with permission from Cates et al. (2011). *Environ. Sci. Technol.* 45(8): 3680-3686. Copyright 2011, American Chemical Society.

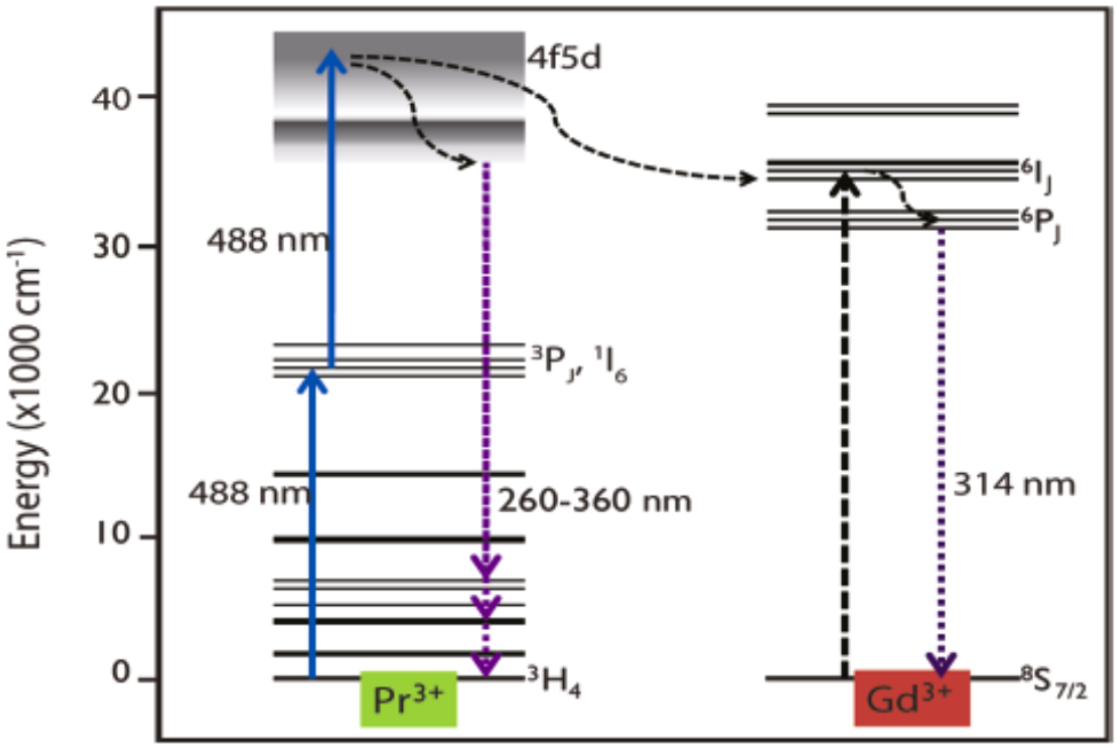

Figure 19. Sensitization of Gd^{3+} upper excited states by doubly excited Pr^{3+} ion. Reprinted with permission from Cates et al. (2011). *Environ. Sci. Technol.* 45(8): 3680-3686. Copyright 2011, American Chemical Society.

4.3.2. Biofilm Inhibition

Figure 20 presents the CSLM micrographs of *P. aeruginosa* biofilms grown on the coated surfaces, showing that the unactivated control surface (Y_2SiO_5:Li^+) and Ln^{3+}-activated dark control showed mature biofilms after 48 h in the reactor, thereby excluding any antimicrobial effects arising from unforeseen phenomena. The upconverting surfaces, in contrast, exhibited clear inhibition of biofilm development with no formation of mushroom-shaped multicellular structures and visibly higher numbers of dead cells, which fluoresce red due to propidium iodide penetration. It is important to consider that this viability test assesses membrane integrity and thus significantly underestimates the number of inactivated cells resulting from UVC exposure, which mainly affects internal biomolecules and only indirectly results in membrane degradation [193]. The Pr^{3+}/Li^+-doped coating resulted in noticeably less biofilm inhibition than the triply doped phosphor surface containing the Gd^{3+} coactivator. These results somewhat contradict our initial assumption that the relative order of UC efficiency among the dip-coated surfaces will mirror that of the powder phosphors, and it is possible that this results from the differences in morphology between the crystalline films and the powders. Scanning electron micrographs of the dip-coated surfaces shows that both doping schemes exhibit crystallites of 50-100 nm, while in the powder samples, crystallite sizes were in the micrometer range (Figure 16 and Figure 21). No significant difference was noticed between the UVC emission intensities of the Pr^{3+}/Li^+ coating and the triply doped coating under 488 nm excitation, though peak areas fluctuated depending on slight variations in

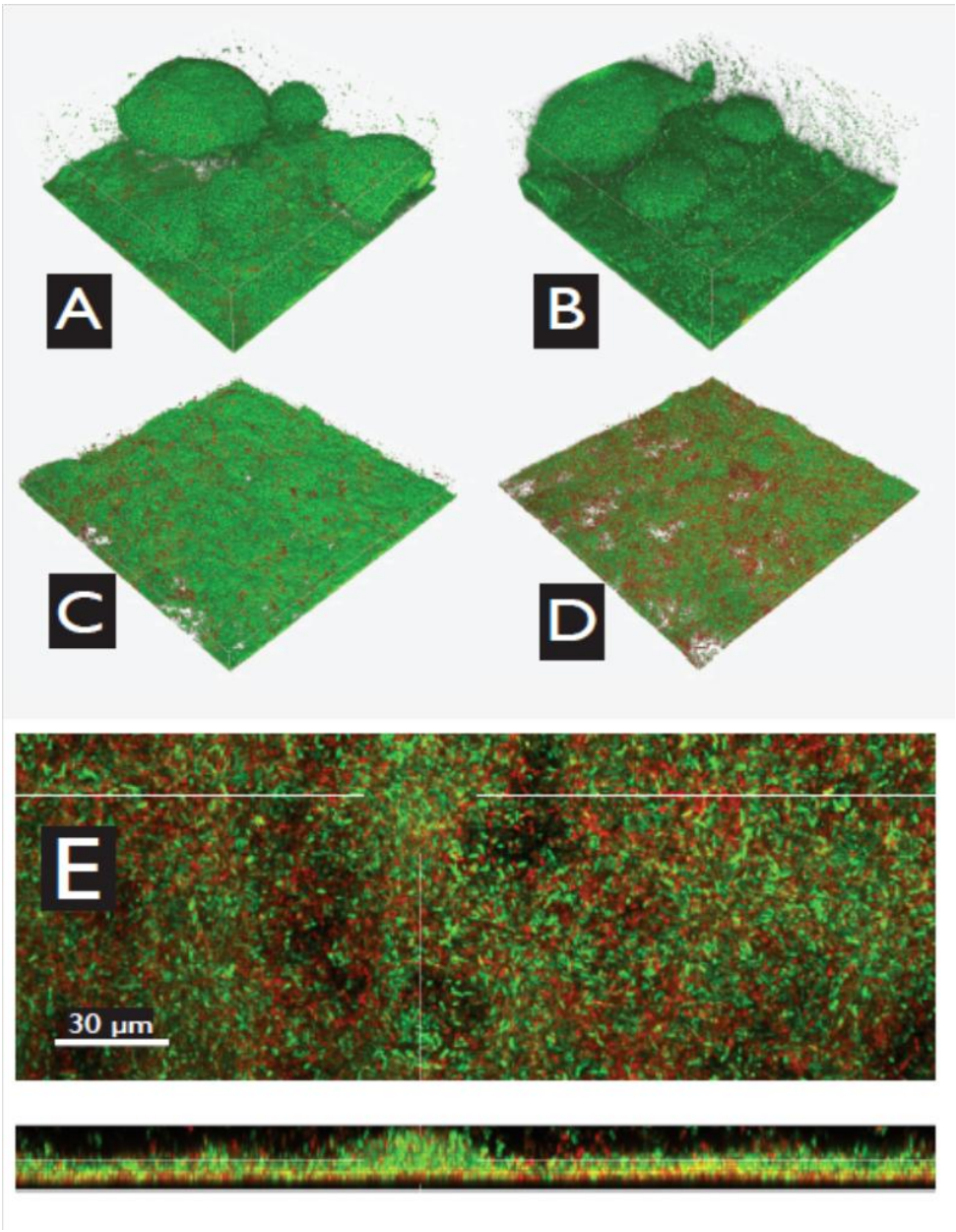

Figure 20. Confocal scanning laser micrographs showing inhibition of Pseudomonas aeruginosa biofilms grown on illuminated phosphor-coated surfaces. (A) Unactivated Y_2SiO_5:Li^+ control surface under visible light; (B) Pr^{3+},Gd^{3+},Li^+-doped surface under dark conditions; (C) Pr^{3+},Li^+-doped surface under visible light; and (D) Pr^{3+},Gd^{3+},Li^+ surface under visible light. (E) Pr^{3+},Gd^{3+},Li^+ surface under light conditions with top view (top) and cross-sectional view (bottom). Live and dead cells appear green and red, respectively, due to BacLight viability staining. Reprinted with permission from Cates et al. (2011). *Environ. Sci. Technol.* 45(8): 3680-3686. Copyright 2011, American Chemical Society.

film thickness (data not shown). Furthermore, antimicrobial effects of 314 nm emission from Gd^{3+} should not be ruled out as a contributor to the observed results, and additional quantitative biofilm analysis is required to assess a true statistically significant difference between the two surfaces' inhibition effects.

Analysis of the biofilm cross sections imaged through CSLM (Figure 20) suggests that the phosphor-coated surface causes inactivation not only in the layer of cells in direct contact with sample but also in the upper portions of the film, several cell layers from the material surface. Such through-space inactivation is indicative of the optical nature of the biocidal mode, in contrast to contact-type polymer antimicrobial surfaces, which have been shown to affect only a monolayer at most [32]. In our experiments, UVC photons emitted into the biofilm are expected to encounter either active genetic material or the remainder that is composed of primarily polysaccharides/lipopolysaccharides (LPS) and smaller amounts of free nucleic acids [194]. The UV absorbances of these substances were reported by Pier et al. [195],showing that LPS generated by *P. aeruginosa* has an absorbance peak at 206 nm and extracellular nucleic acids have a peak at approximately 255 nm with moderate widths. Both regions of absorption are located deeper in the UV than the emission band from the Pr^{3+}- activated surfaces, which peaks at 278 nm, still well within the mutagenic range. The minimal overlap between these spectra accounts for the lack of complete attenuation of incident visible light and emitted UV photons from the phosphor surface by biofilm slime and supports the occurrence of inactivation in upper portions of the films. This characteristic also distinguishes the UC strategy from photocatalysis in that availability of oxygen at the material interface is no longer a requirement and interference by foulants is a more continuous function of their

absorption behavior, rather than the possibility of complete quenching of radical species by water or organic matter. While the UV photon flux will nonetheless diminish gradually with increasing biofilm thickness, the above observations show a fundamental difference in the mode of biocidal action, which is capable of penetrating certain fouling layers without the need for direct contact or chemical biocide release, as with existing technologies.

4.3.3. Surface Inactivation

Quantitative analysis of antimicrobial effect was studied through inactivation kinetics of *Bacillus subtilis* ATCC 6633 endospores deposited and dried on the coated surfaces. The spores of this organism show similar UV susceptibility to *Bacillus anthracis* spores and will remain viable in dry conditions [196]. Figure 21 shows the inactivation curves resulting from exposure of the deposited spores on coated surfaces to a daylight fluorescent lamp at 1960 $\mu W/cm^2$ in the blue range equipped with a UV filter (cutoff <400 nm). Ten days of visible light exposure resulted in 1.01-log inactivation (90% reduction) of *B. subtilis* spores on the

$Y_2SiO_5:Pr^{3+},Gd^{3+},Li^+$-coated surface. Figure 22 (top) compares the inactivation on differently doped surfaces after 10 days of exposure, with ascending order of mean inactivation rate as follows: $Pr^{3+} < Pr^{3+}/Gd^{3+} < Pr^{3+}/Li^+ < Pr^{3+}/Gd^{3+}/Li^+$. This order follows that of increasing UC emission intensities from Figure 17 with the exception of the relative efficacies of the Li^+-doped samples, which are in agreement with the biofilm inhibition results. We also conducted a biodosimetric analysis based on the dose-response curve of *B. subtilis* spores inactivated with 254 nm UV radiation, shown in

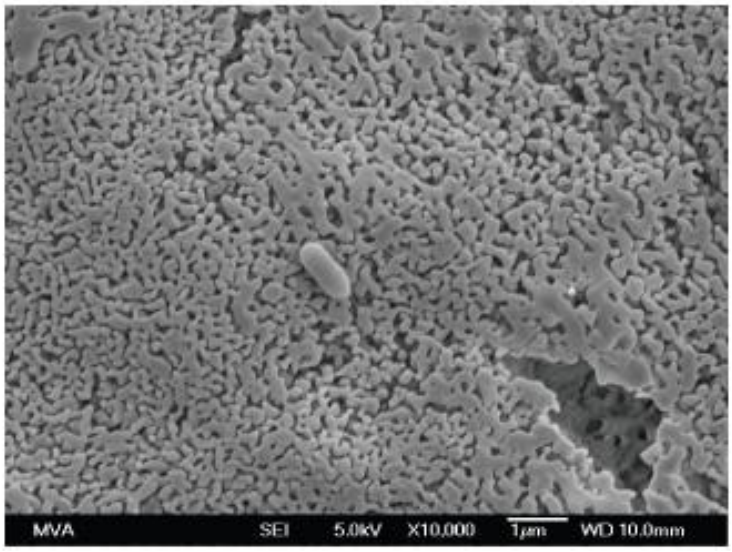

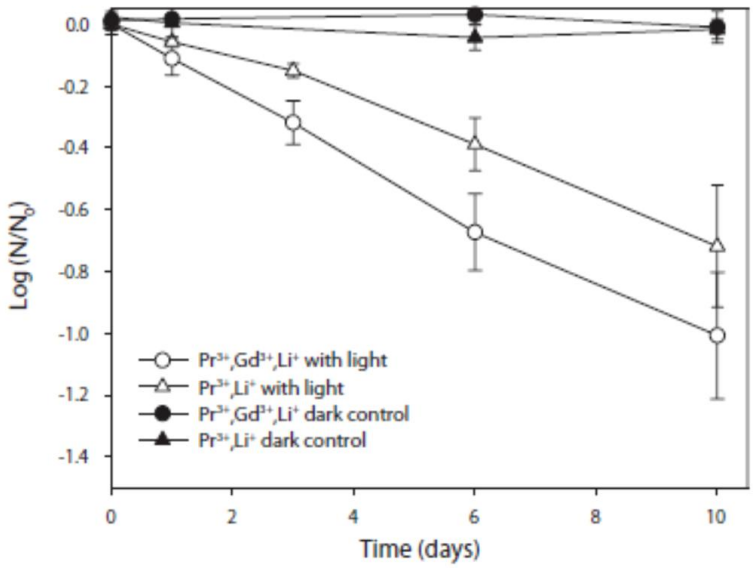

Figure 21. Inactivation of Bacillus subtilis spores on dry phosphor-coated surfaces. **Top:** Inactivation kinetics of Y_2SiO_5 phosphors with different doping schemes exposed to "daylight" fluorescent lighting and dark controls. Unactivated surfaces showed no inactivation under visible light after 10 days (data not shown). **Bottom:** Scanning electron micrograph of a *B. subtilis* spore on a Y_2SiO_5:Pr^{3+},Li^+ nanocrystalline surface prepared through dip-coating in precursor sol solution. White scale bar is 1 μm. All error bars show standard deviations. Reprinted with permission from Cates et al. (2011). *Environ. Sci. Technol.* 45(8): 3680-3686. Copyright 2011, American Chemical Society.

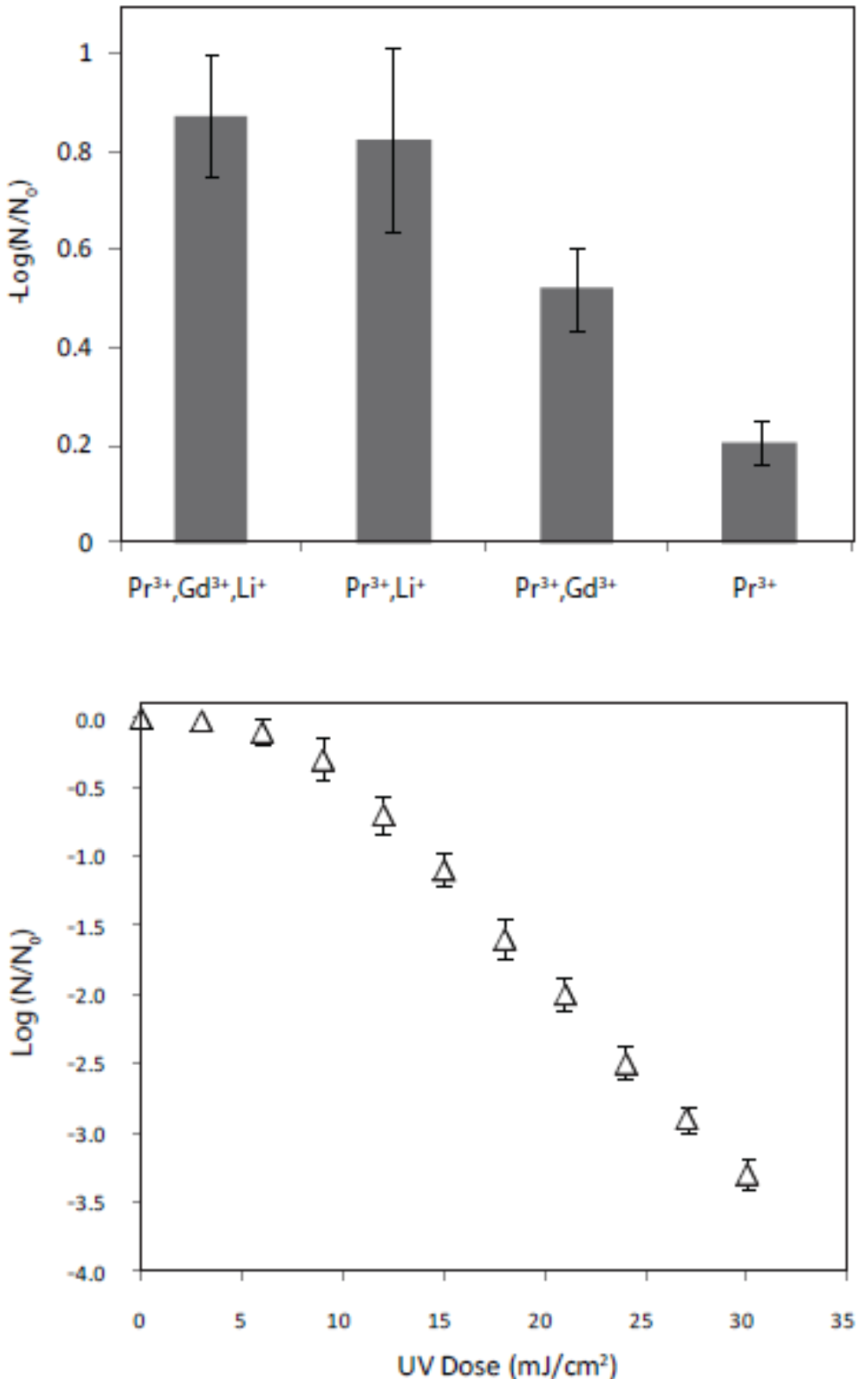

Figure 22. Top: 10-day log inactivation of spores on Y_2SiO_5-coated surfaces with different doping schemes under visible light. **Bottom:** Inactivation dose_response of B. subtilis spores on dry surface exposed to known doses of UVC from low-pressure Hg bulbs, $\lambda = 254$ nm. The linear portion of this curve was used for biodosimetric estimation of the upconversion efficiency of coated samples. Reprinted with permission from Cates et al. (2011). *Environ. Sci. Technol.* 45(8): 3680-3686. Copyright 2011, American Chemical Society.

Figure 22 (bottom), which projects that the 1.01-log reduction from the triply doped surface during the kinetic experiments resulted from an approximate 14 mJ/cm^2 UV dose (254 nm equivalent). This translates to an average UV intensity of 0.016 $\mu W/cm^2$ and places the external optical efficiency of the system on the order of 0.001%, defined as the percentage of incident blue light power density converted into UVC of 254 nm equivalence and emitted upward from the surface. The inactivation experiments herein represent the lowest excitation intensity used in an evaluation of upconversion materials reported thus far and show that such low conversion efficiencies are already adequate to invoke a measurable effect on microorganisms and even biofilms. While inactivation kinetics are much slower in comparison to conventional technologies, there exists ample room for improvement in material performance through pursuing further understanding of visible-to-ultraviolet UC phosphors and through use of improved surface coatings. Pending future increases in conversion efficiency, practical inactivation of pathogens under ambient light intensities may be possible, as well as more rapid disinfection under stronger light, such as tropical sunlight for use in solar water disinfection (SODIS) for developing countries.

4.4. Acknowledgements

This section contains contributions from coauthors and was published in: *Cates, Ezra L., Min Cho, Jae-hong Kim (2011). "Converting Visible Light into UVC: Microbial Inactivation by Pr^{3+}-Activated Upconversion Materials."* Environmental Science & Technology ***45****(8): 3680-3686.*

CHAPTER 5

DELINEATING MECHANISMS OF UPCONVERSION ENHANCEMENT BY Li^+ CODOPING IN $Y_2SiO_5:Pr^{3+}$

5.1. Introduction

In the previous chapter, Li^+ was added to the $Y_2SiO_5:Pr^{3+}$ phosphors in order to improve UC efficiency; the use of this codopant was borrowed from the literature, wherein Li^+ doping in photoluminescent, oxide-based crystalline materials is a widely reported strategy to significantly enhance optical efficiencies. Particular success has been reported for UC phosphors, wherein upconverted emission enhancements of roughly an order of magnitude have resulted from addition of Li^+ to host materials such as Y_2O_3 [160, 181, 191], Gd_2O_3 [197], $BaTiO_3$ [198], and Y_2SiO_5 [104], regardless of the type of activator ions employed. The mechanism by which Li^+ enhances luminescence is complex, and actually consists of several independent mechanisms with the relative contribution of each being seemingly dependent on the specific material.

The most obvious way by which Li^+ can improve luminescence is via a flux effect leading to larger crystallites. At annealing temperature, the presence of the codopant may result in a liquid phase at the grain boundaries that dramatically enhances the rate of crystallite formation. This has been reported to occur during sol gel, combustion, and conventional solid state syntheses [104, 186, 199, 200]. Larger crystallites with higher phase

purity are produced, as evidenced by both electron microscopy and peak width analysis of X-ray diffraction (XRD) patterns. Crystallite enlargement results in a greater fraction of activator ions inhabiting the interior of the crystals, rather than the near-surface where energy can be rapidly lost by transfer to surface defects with high vibrational energies [53]. The latter effect is responsible for the poor UC performance of nanoscale phosphors in general, which many researchers have successfully mitigated through the encapsulation of UC nanoparticles with a transparent shell to prevent energy transfer to surface defects [153, 155, 190].

Another frequently stated explanation for optical enhancement by lithium is the tailoring of the activator ions' site geometry [173, 181, 197, 198]. Lanthanide UC phosphors rely strictly on parity-forbidden intra-4f electronic transitions which will exhibit low spontaneous transition probabilities in the presence of inversion symmetry according to the Laporte rule. This low transition probability can be detrimental, as it results in a low absorption coefficient, yet beneficial in that it also contributes to the characteristic long excited-state lifetimes of Ln^{3+} ions that allow UC to take place. Incorporation of a low concentration of Li^{+} into a phosphor crystal and the resultant localized distortion of activator cation sites have been stated by many to be the main cause of observed luminescence enhancements, wherein the distortion allows stronger absorption of excitation photons. However, several of these studies also report an increase in the radiative lifetimes of the emitting ions [161, 193, 199, 201]. Since the intrinsic radiative lifetime, τ_R, is inversely related to the spontaneous transition probability, A_{ba} ;

$$\tau_R = (A_{ba})^{-1} \qquad \text{Eq. 1}$$

And the probability of stimulated absorption, either from the ground state or an intermediate state, is given by:

$$W_{ab} = \frac{g_b}{g_a} A_{ba} n_\omega \qquad \text{Eq. 2 (ref. [55])}$$

(where g_a and g_b are the statistical weights of the absorbing and emitting states, respectively, and n_ω is the number of photons of the appropriate energy within the control volume of the excitation beam[55]), then by substitution of Eq. 1 into Eq. 2, it follows that any luminescence improvement resulting from a change in site geometry accompanied by greater absorption will be accompanied by a *decrease* in radiative lifetime of both intermediate and final emitting states. It is thereby implied that lower activator site symmetry yields both higher absorption and emission probabilities. The data in the above references therefore suggest that other factors, aside from, or in addition to site distortion, are responsible for the observed UC enhancement that accompanies the slower luminescence decay rates.

While the flux effect and site geometry distortion warrant consideration in virtually any phosphor doped with Li^+, still other mechanisms may be important depending on the specific host crystal structure. For materials in which the trivalent activator substitutes a divalent host cation, such as Ca^{2+}, lithium substitution can provide charge compensation and reduce the number of cation vacancies [202]. Other studies have reported a phase change upon Li^+ addition, which may or may not be optically favorable [104, 203]. There also exists much ambiguity as to the possibility and role of oxygen vacancies formed when Li^+ replaces a trivalent host cation to form an aliovalent

substitution. Activator site distortion, lattice expansion, and sensitization by F-centers have all been suggested in the literature as possible beneficial effects of these vacancies [204, 205]; however, there is little evidence showing whether or not charge compensation occurs as a result of vacancies or interstitial Li^+. In this Chapter, the mechanisms of enhancement by Li^+ are delineated and quantified, in order to better understand its role in $Y_2SiO_5:Pr^{3+}$ UC and other phosphor materials. Other codopants were also examined for comparison in order to reveal which properties of Li^+ are of importance.

5.2. Experimental Section

5.2.1. Syntheses

Y_2SiO_5 phosphors were prepared by a sol gel decomposition method described in detail in Section 4.2.2, using an assumed stoichiometry of $Y_{2-x-y}Pr_xLi_{3y}SiO_5$. A Pr^{3+} concentration of 1.2 mol.% (x=0.024) was used for all samples, which was previously determined to be the optimum concentration for the Li^+-doped phosphors and all samples were annealed at 1000 ºC for 3 h unless otherwise stated. Sodium, scandium and lanthanum codoping were achieved by adding the 99.995% purity metal nitrate to the sol, and zinc codoping by adding 99.999% ZnO powder to the Y_2O_3 prior to dissolving in HNO_3, while appropriate portions of Y_2O_3 were omitted. Zirconium doping was conducted through the addition of zirconyl chloride. Samples of each composition were prepared in triplicate. Some samples were subjected to additional annealing at 1500 °C

in air for 1 h using a Lindberg Blue-M general purpose tube furnace and are denoted herein as X2-1500º.

5.2.2. Analyses

Upconversion emission spectra (488 nm argon laser excitation) were obtained as described Section 4.2.4. Stokes (visible) emission under 488 nm excitation was recorded using the same setup as with UC measurements, except that the 400 nm shortpass filter at the monochromator entrance was replaced with a 488 nm notch filter. Scanning electron micrographs were obtained as in 4.2.4. XRD patterns were measured using a Panalytical X'pert Pro diffractometer with X'celerator detector. Crystallographic parameters were obtained via Rietveld analysis of XRD data using GSAS and EXPGUI software [206, 207]. Patterns were modeled using the X2 monoclinic phase (space group I 2/a [208]) and/or the X1 phase (space group P $2_1/c$ [209]). The crystal structure was drawn using DRAWxtl [210]. The lithium contents of select samples were determined by a certified commercial lab via inductively coupled plasma optical emission spectroscopy (ICP-OES) after sodium hydroxide flux digestion.

5.3. Results and Discussion

5.3.1. Upconversion Emission

Under blue light excitation, $Y_2SiO_5:Pr^{3+}$ can emit UV radiation of 255-365 nm as a result of excited state absorption and, to a greater extent, energy transfer upconversion (ETU) followed by radiative relaxation from the lowest 4f5d level, as previously shown [104, 172]. Figure 23A compares the emission spectra of the unmodified $Y_2SiO_5:Pr^{3+}$ material (*i.e.* no codopants, annealed at 1000 ºC for 3 h) and the most efficient composition ("10%" Li^+ addition, *i.e.* prepared assuming a composition of $Y_{1.909}Pr_{0.024}Li_{0.2}SiO_5$[‡]) under 488 nm excitation by an argon laser at 140 mW, and Figure 23B shows the integrated emission intensities versus Li^+ concentration. The concentrations reported as percentage reflect the amount of Li^+ added during synthesis, while the ICP-OES measurements showed that approximately 5-10% of the added Li^+ evaporated during annealing at 1000 ºC for 3 h. It was observed that the unmodified material showed an emission maximum at 285 nm, while samples with 3% Li^+ or higher showed maxima at 276 nm. This is associated with a change from the X1 to the X2 polymorph, as described below, and the associated shift in energy of the 4f5d manifold [24, 192]. Emission increased markedly with increasing Li^+ doping and then the trend reversed between 10 and 12.5% doping. A separate set of samples, denoted X2-1500º, was prepared using no Li^+ and annealed at 1500 ºC for 1 h, which also showed more intense UC emission than the original material. Visible light Stokes emission from the ^3P_J states of Pr^{3+} was relatively constant for samples with the same host polymorph and showed no correlation to Li^+ dopant concentration (data not shown).

[‡] While 7.2% Li^+ was found to be optimum during the experiments reported in the previous chapter, refined synthesis technique revealed that UC reaches a maximum at approximately 10% Li^+.

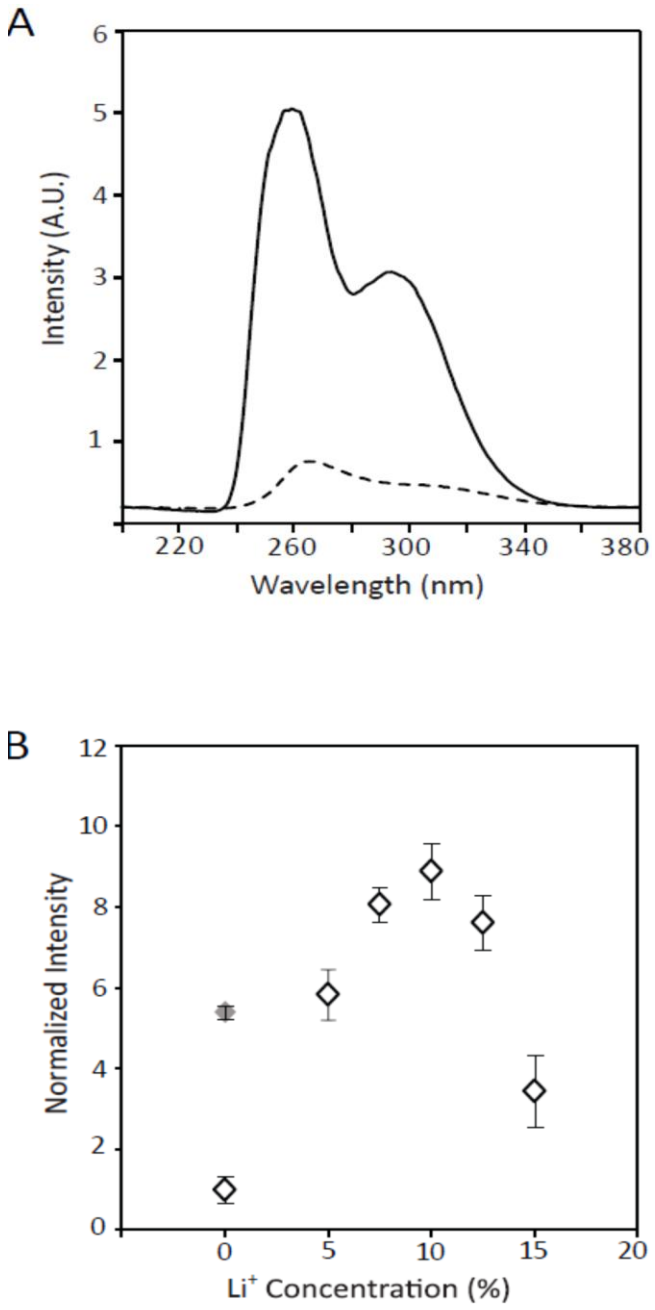

Figure 23. (A) UV upconversion emission spectra of unmodified $Y_2SiO_5:Pr^{3+}$ (dashed) and the same material doped with 10% Li^+ (solid), λ_{exc} = 488 nm. (B) Integrated UV emission intensities of samples prepared at 1000 ºC (hollow) and X2-1500º (solid gray) versus codoping concentration. Intensities have been normalized to that of the unmodified phosphor. Error bars show standard deviations. Reprinted with permission from Cates et al. (2012). *J. Phys. Chem. C* 116(23): 12772-12778. Copyright 2012, American Chemical Society.

5.3.2. Crystal Structure and Morphology

Evidence of a flux effect by Li^+ is clearly seen in Figure 24, wherein the codoped powders showed spherical crystallites of up to ~1.5 μm, compared to <50 nm for the unmodified phosphor (see Section 4.3.1). The X2-1500º samples also exhibited micron-sized crystallites showing that the high temperature treatment resulted in similar growth kinetics to the presence of a Li^+ flux. X-ray diffraction analysis revealed further differences in crystal structure and purity among the various samples. The host crystal, Y_2SiO_5, is known to form two polymorphs [211]. The first, X1-Y_2SiO_5, is formed below 1250 °C and is isostructural to other rare-earth silicates of the form RE_2SiO_5, where RE = La^{3+} through Gd^{3+} (the larger rare-earths). This phase has a monoclinic unit cell with space group P 2_1/c and the Y^{3+} ions occupy two sites that are 9-coordinated and 7-coordinated, respectively. The second phase, X2-Y_2SiO_5, formed by annealing above 1250 °C, is isostructural to the smaller rare-earth silicates (RE = Tb^{3+} through Lu^{3+}) and has a monoclinic unit cell with space group I 2/a. There are also two crystallographically distinct Y^{3+} sites in this structure, but their coordination is lower at 6 and 7, respectively. The X2 structure is shown in Figure 25. As expected, unmodified Y_2SiO_5:Pr^{3+} exhibited the X1 structure; however, as described in the previous chapter, Li^+ doping induced a complete transformation to the X2 structure at concentrations as low as 3%, even though these samples were still annealed at only 1000 °C. The X2-1500º samples also adopted the X2 structure, due to their higher annealing temperature. As discussed later, the phase transition to X2-Y_2SiO_5 is responsible for a significant fraction of the UC enhancement seen in the Li^+-doped and X2-1500º phosphors.

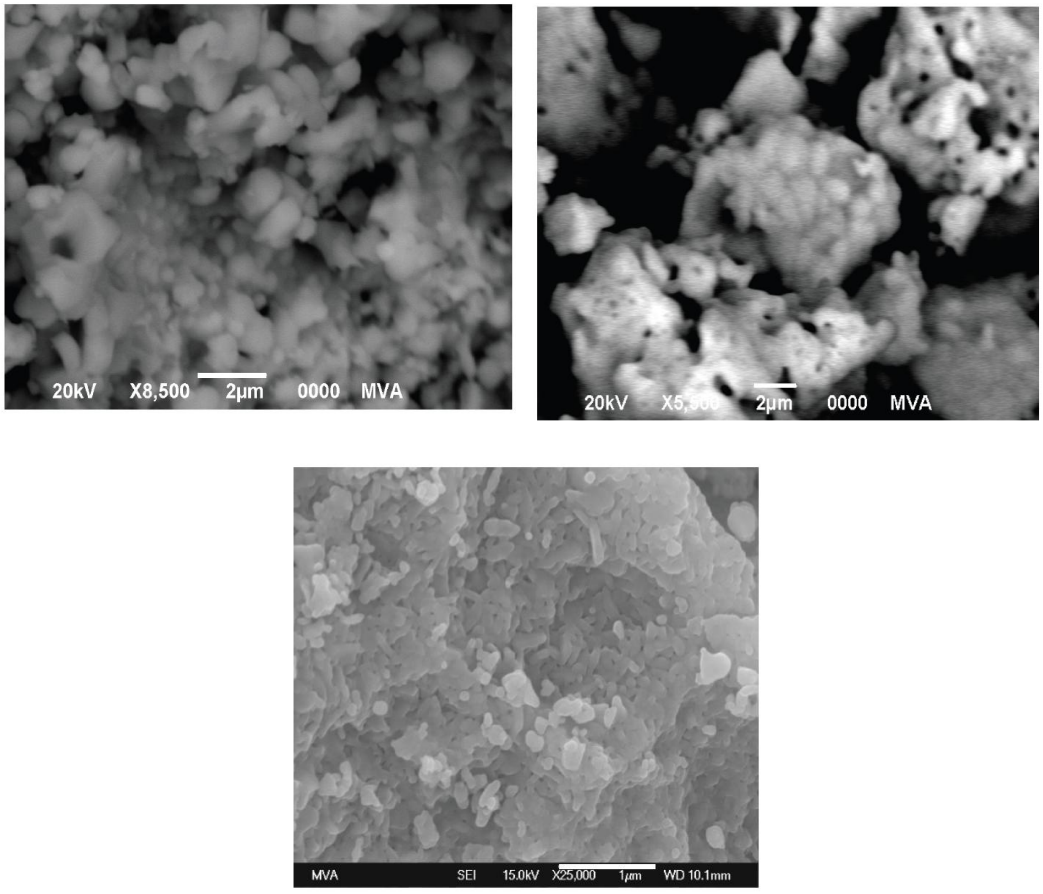

Figure 24. Scanning electron micrographs of $Y_2SiO_5:Pr^{3+}$ doped with 10% Li^+ (top left, scale bar = 2 µm), X2-1500° (top right, scale bar = 2 µm), and $Y_2SiO_5:Pr^{3+}$ doped with 5% La^{3+}, annealed at 1000 °C for 36 h (bottom, scale bar = 1 µm). Reprinted with permission from Cates et al. (2012). *J. Phys. Chem. C* 116(23): 12772-12778. Copyright 2012, American Chemical Society.

According to the Rietveld analyses, one of which is depicted in Figure 25 (structural parameters are listed in Appendix B), the main impurity found in the unmodified Y_2SiO_5:Pr^{3+} phosphor was a 6% content of the X2 polymorph, while Li^+-doped and X2-1500º samples contained only small fractions of Y_2O_3. Figure 26 shows unit cell volume as a function of Li^+ doping concentration, wherein the undoped X2-phase Y_2SiO_5 has the smallest unit cell and the Pr^{3+} singly-doped phosphor ("X2-1500º") shows a significantly expanded lattice. Addition of Li^+ causes an initial drop in cell volume which then increases with higher Li^+ content until ~12.5%; thus, the presence of Li^+ appears to partially negate the lattice expansion due to Pr^{3+}, but causes a less pronounced expansion on its own when doped at increasing concentrations. When Li^+ replaces Y^{3+} in the material, it is unknown whether charge compensation occurs through the formation of oxygen vacancies ($V_O^{\cdot\cdot}$, *i.e.* $Y_{2-y}Li_ySiO_{5-y}$) or by interstitial codopant ions ($Li_i^{\cdot}$, *i.e.* $Y_{2-y}Li_{3y}SiO_5$), both of which could potentially result in the observed expansion. Yet, the results mentioned above, and other data that follow, suggest that formation of $V_O^{\cdot\cdot}$'s is the more likely mechanism. One out of every five oxygen atoms in X2-Y_2SiO_5 is not associated with SiO_4^{2-} tetrahedra and are thus more weakly bound in the material [208, 211]; these O^{2-} ions also show the shortest Y-O bond distances in the Y^{3+} oxygen coordination spheres. It is therefore hypothesized that if one of these sites were vacated due to charge compensation, the adjacent RE site would have more space to allow occupation by large Pr^{3+} ions. In this fashion, localized combinations of $Li_Y''/V_O^{\cdot\cdot}/Pr_Y^x$ would allow Pr^{3+} to enter the structure while causing less overall expansion of the lattice and result in the relative unit cell volumes seen in Figure 26. Also according to this

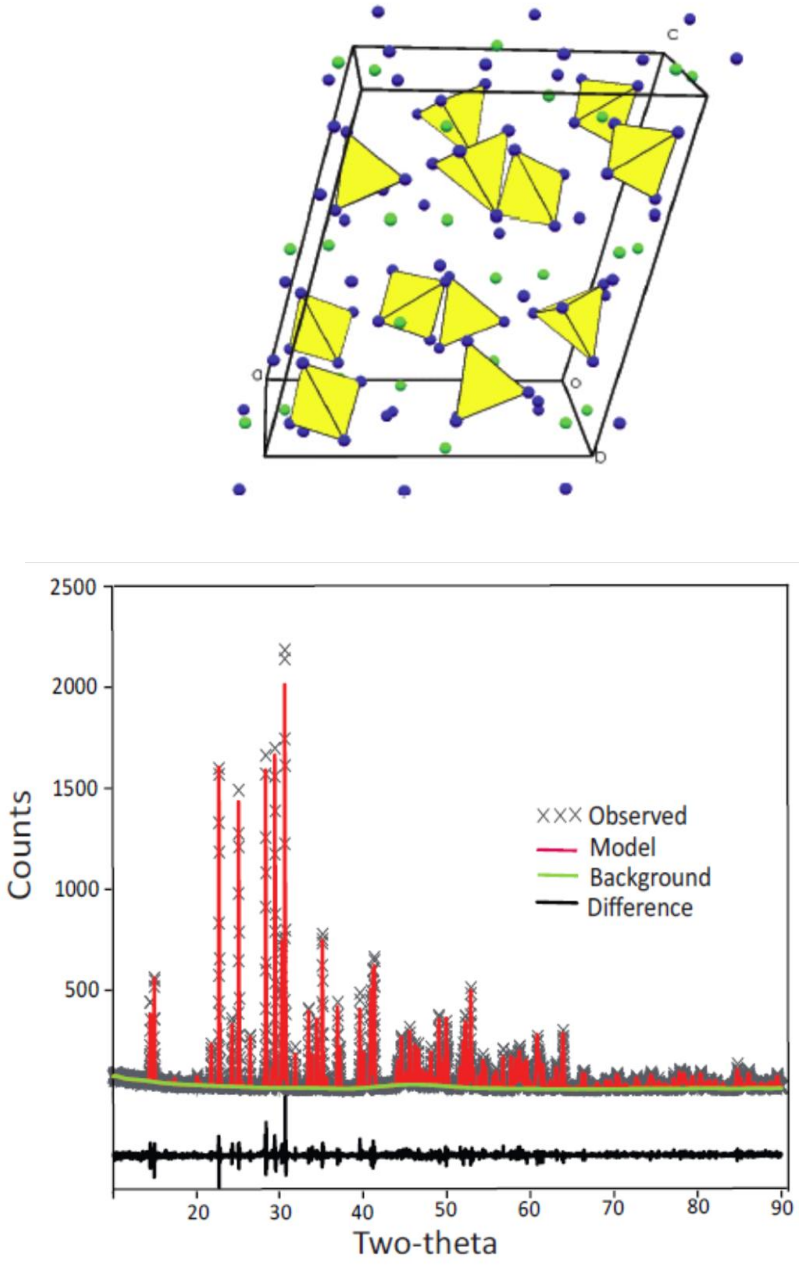

Figure 25. Top: Structure of X2−Y_2SiO_5; blue = O^{2-}; green = Y^{3+}, yellow = Si^{4+}-containing tetrahedra. Bottom: Sample Rietveld fit to X-ray diffraction data of doped X2−Y_2SiO_5 . Reprinted with permission from Cates et al. (2012). *J. Phys. Chem. C* 116(23): 12772-12778. Copyright 2012, American Chemical Society.

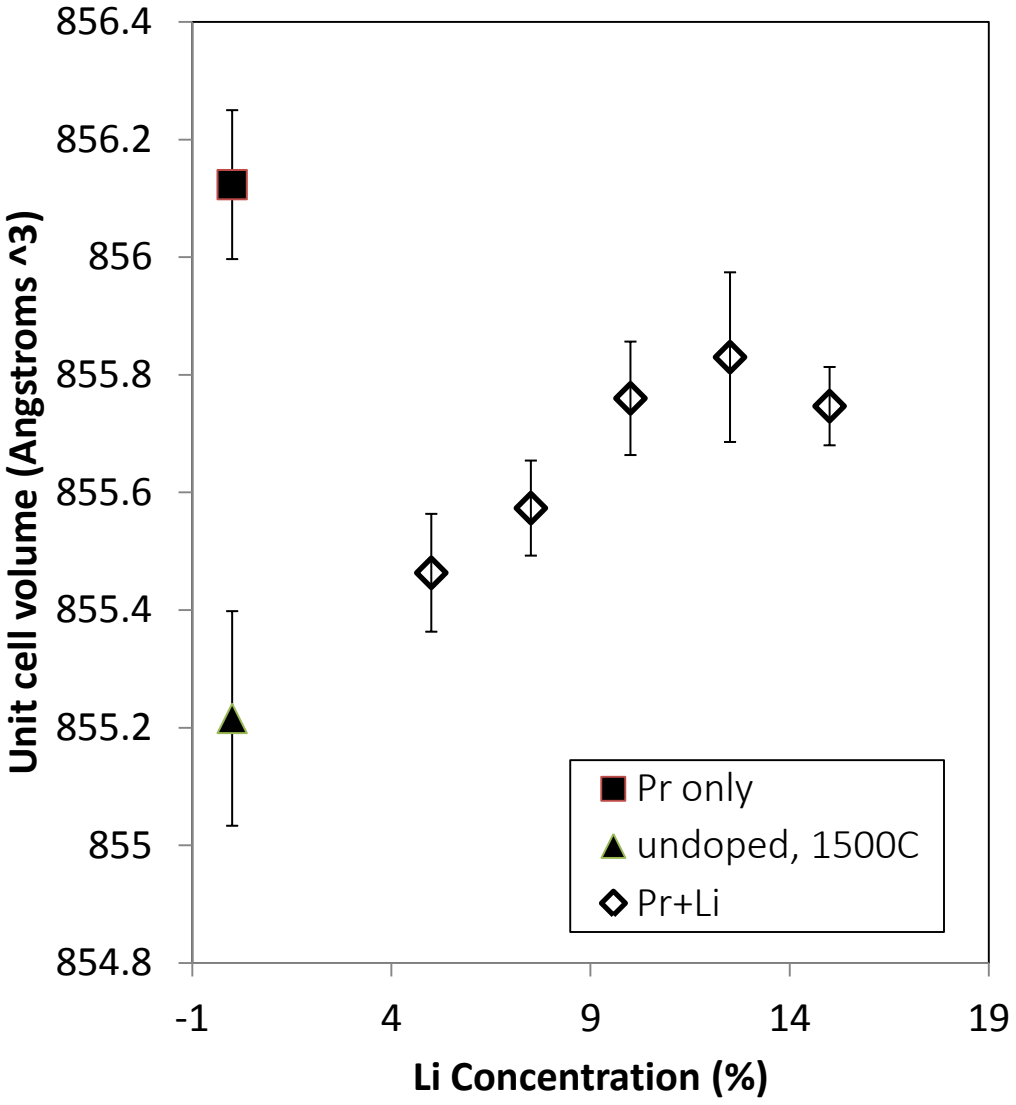

Figure 26. Unit cell volume versus Li^+ concentration for X2−Y_2SiO_5 samples. Reprinted with permission from Cates et al. (2012). *J. Phys. Chem. C* 116(23): 12772-12778. Copyright 2012, American Chemical Society.

Table 4. Effects of various codopants on the crystal structure (polymorph) of $Y_2SiO_5:Pr^{3+}$ annealed at 1000 ºC. All species were added at 10%, with the exception of Zr^{4+}. *Doping with 3% Li^+ and 6% Zr^{4+} resulted in the X1 phase, while 10% Li^+ and 6% Zr^{4+} resulted in the X2 phase.

	Ionic Radius	***ΔZ*** ***(Y^{3+} substitution)***	***X2 phase 1000º C?***
Li^+	$<Y^{3+}$	-2	Yes
Na^+	$>Y^{3+}$	-2	No
Zn^{2+}	$\approx Li^+$	-1	Yes
Sc^{3+}	$\approx Li^+$	0	No
Zr^{4+}	$\approx Li^+$	+1	No*

theory, the gradual increase in volume seen with increasing Li^+ content is due to the increased concentration of $V_O^{\cdot\cdot}$.

To reveal why the addition of Li^+ to Y_2SiO_5 causes a transformation to the high temperature phase, other optically inactive codopants – including Na^+, Zn^{2+}, and Sc^{3+} – were doped at 10% (assuming $Y_{1.909}Pr_{0.024}M_{0.2}SiO_5$) and tested for any similar effects. Results, shown in Table 4, suggest this phase transition is only observed at lower temperature for codopant ions that are both *(1)* smaller than Y^{3+} and *(2)* of lower oxidation state, *i.e.* Li^+ and Zn^{2+}. Since the X2 polymorph has lower Y^{3+} site coordination numbers, it is reasonable that doping with smaller ions would thermodynamically encourage this phase. However, it also seems apparent that aliovalent substitution and the resultant charge compensation mechanism (whether it is $V_O^{\cdot\cdot}$ or interstitial ions) are required, or else Sc^{3+} doping would have resulted in the X2 polymorph. We further confirmed this model by doping Zr^{4+} into the Li^+-containing samples to show the effect of reintroducing some of the positive charge that would be lost when Y^{3+} is replaced by Li^+. This was done using the smallest Li^+ concentration found to result in the phase transformation, 3%, and Zr^{4+} was added at 6% in an attempt to prevent the need for any charge compensation. As determined by XRD, adding Zr^{4+} to the Li^+-doped material in this fashion resulted in X1-Y_2SiO_5 and negated the effect of Li^+ on the crystal structure (while also showing additional impurities arising from incomplete dissolution of Zr^{4+}). Finally, a sample was prepared using 6% Zr^{4+} and 10% Li^+, which once again formed the X2 polymorph, confirming that the structure resulting from 1000 ºC synthesis is intimately dependent on charge balance. Also of note, other results described below

suggest that X1-Y_2SiO_5 may only be kinetically favored at 1000 ºC, rather than thermodynamically stable; yet, the above observations suggest that it is the small size and lower oxidation state of Li^+ that promote the X2 phase, and not solely enhanced kinetics. Such kinetic enhancement is likely to be caused by Li^+ codoping regardless of whether or not Zr^{4+} is added. None of the codopants, aside from Li^+, resulted in any enhancement of UC emission at the concentrations tested.

5.3.3. Delineation of Enhancement Mechanisms

Quantification of the contributions from the flux effect and phase transition to the total UC enhancement arising from Li^+-doping was accomplished by isolating these variables from one another. First, synthesis of X1-Y_2SiO_5:Pr^{3+} samples with micron-sized crystallites was attempted via long-duration annealing at 1000 ºC in order to observe the optical improvement resulting solely from the consequences of the flux effect. Difficulties were encountered, however, because at annealing times over 24 h, significant fractions of the X2 polymorph appeared in the XRD patterns. This result suggests that at 1000 ºC, X1-Y_2SiO_5 is only kinetically stable and not thermodynamically favored, as mentioned previously. To overcome this problem, the materials were codoped with 5% La^{3+}, which is a larger RE and stabilizes the X1 phase. After the normal 3 h annealing, this material showed UC emission identical to the original unmodified material and, after extended annealing, showed only the X1 polymorph and slightly enhanced UC emission. The SEM image in Figure 24 shows that after 36 h annealing, crystallites of several hundred nanometers result; while these are not as large

as those of the 10% Li^+ samples, additional annealing resulted in no further emission enhancement, which reached a maximum at ~40% improvement over the original emission intensity. This enhancement translates to ~5% of the total enhancement by Li^+, thus larger crystallites resulting from the flux effect can be considered responsible for this portion, as illustrated in Figure 27.

To quantify the UC enhancement resulting only from the phase change induced by Li^+, we compared the emission of X2-1500º to that of the aforementioned $Y_2SiO_5:Pr^{3+},La^{3+}$ phosphor showing large crystallites, as the only optically relevant difference between these two materials is the crystal structure – X2 versus X1. An additional 3.9-fold increase in emission intensity was determined from integrated peak areas, which accounts for ~50% of the total enhancement by Li^+, shown in Figure 27. There is firm consensus in the literature that the X2 phase exhibits superior optical properties to X1, though the precise reasons are not well established [187, 192, 212]. An explanation was put forth by Lin et al., who stated that the X2 polymorph shows reduced covalency and greater rigidity, which the authors claimed reduces vibronic coupling and nonradiative losses [192]. However, interpretation of the visible emission spectra as part of this work revealed that the ^3P_J intermediate states of Pr^{3+} in the X2-Y_2SiO_5 host are of notably lower energy (~125 cm^{-1}, data not shown) than in the X1 polymorph, corresponding to stronger absorption of 488 nm light. The UC emission of these two materials was retested using a 447 nm diode-pumped solid state laser and found that the emission of X1-$Y_2SiO_5:Pr^{3+},La^{3+}$ was nearly equivalent intensity to X2-1500º. Hence, the UC enhancement that occurs upon forming the X2 polymorph is mostly a result of the

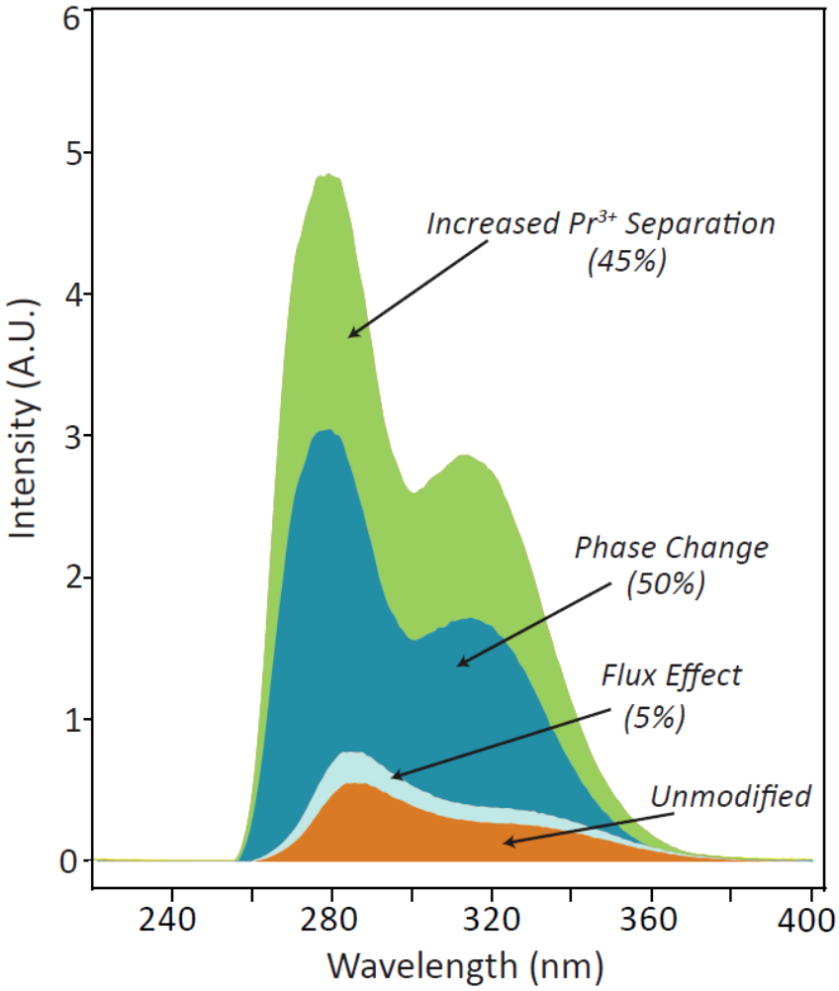

Figure 27. Quantitative contributions of the multiple structural effects of Li^+ codoping on the upconversion efficiency of $Y_2SiO_5:Pr^{3+}$, codoped with 10% Li^+. Numbers in parentheses reflect the approximate percentage contribution to the total area comprising the top three regions. Reprinted with permission from Cates et al. (2012). *J. Phys. Chem. C* 116(23): 12772-12778. Copyright 2012, American Chemical Society.

Pr^{3+} intermediate levels more suitably matching the excitation wavelength of these experiments.

It is clear from these data that the X2 phase is preferred with respect to Pr^{3+} UC of 488 nm light, however, the 10% Li^{+}-doped material still shows markedly greater emission intensity than the X2-1500º material, despite both having the preferred phase structure, high phase purity, and large crystallite size. As mentioned previously, activator site distortion is frequently used as an explanation for improved Ln^{3+} emission upon Li^{+} doping; however in this case, no correlation between visible-range ^3P_J stokes emission and Li^{+} concentration was observed, which should have been evident if symmetry effects were causing significantly higher transition probabilities. Furthermore, all the activator sites in both polymorphs are already of low point symmetry (C1) [213].

Insight into the mechanism of the remaining 45% of the enhancement by Li^{+} was found in Malyukin et al. wherein Pr^{3+} ions were found to form clusters when doped in Y_2SiO_5, even in single crystals prepared from a melt [214]. Such clusters then increase the probability of detrimental cross relaxation (CR), which occurs when a Pr^{3+} ion excited to the $^3P_0$ state transfers energy to a neighboring ion through a phonon-assisted $^3P_0 \rightarrow {}^1D_2$ / $^3H_4 \rightarrow {}^3H_6$ mechanism allowing efficient non-radiative decay (Figure 28) [215]. If Li^{+} were to disperse these clusters, as has been asserted by Yang et al. for Er^{3+} in $Y_3Al_5O_{12}$ [216], then CR would be reduced and UC efficiency would improve. Too much separation, however, would discourage the energy transfers required for ETU (Figure 13). Indeed, it is feasible that there exists a certain range of inter-ion separation wherein CR is minimized while $^3P_J \rightarrow {}^3H_4$ / $^3P_J \rightarrow$ 4f5d ETU is still relatively efficient. Energy transfer among Ln^{3+} ions in

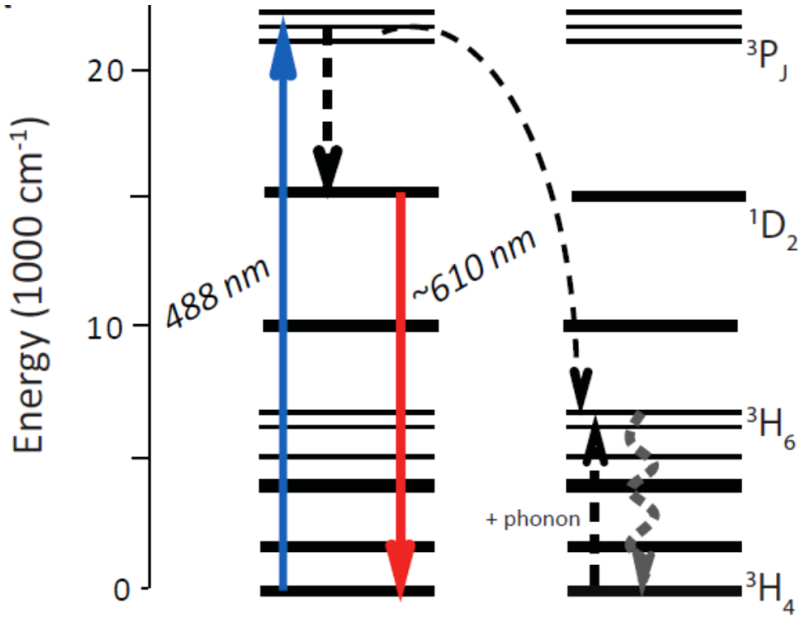

Figure 28. Cross relaxation among two Pr^{3+} ions. Reprinted with permission from Cates et al. (2012). *J. Phys. Chem. C* 116(23): 12772-12778. Copyright 2012, American Chemical Society.

crystals are induced dipole interactions which can be described by Förster theory [217]; therein, the critical transfer radius increases with greater spectral overlap between the two transitions that are to occur. In the UC transfer, there is great overlap between the $^3P_J \rightarrow {}^3H_4$ and $^3P_J \rightarrow$ 4f5d transitions, owing largely to the high density of 4f5d states. The cross-relaxation mechanism, on the other hand, relies on levels with lower densities of states and even requires phonon assistance due to an energy mismatch, implying significantly less overlap and therefore smaller critical transfer radius. Thus, it is not paradoxical to imply that adjustment of inter-ion separation can decrease concentration quenching while having a negligible impact on Pr^{3+} ETU probabilities.

Cross-relaxation behaviors were probed by examining the visible luminescence under 488 nm excitation. Some of these spectra are shown in Figure 29 and all distinguishable peaks were assigned to transitions from the $^3P_0$ and $^3P_1$ states, with the exception of the peaks at ~590-615 nm. These emission peaks are a result of transitions from the $^1D_2$ Stark states, which, at the Pr^{3+} concentrations used, are populated almost exclusively by the CR mechanism described above [217]. It is seen in the figure that the emission peaks of the sample doped with 10% Li^+ are slightly more intense than the X2-1500º sample in all cases except in the $^1D_2$ emission region, which is consistent with the notion that reduced CR resulting from Li^+ doping will result in less $^1D_2$ emission and both greater UC (UV) emission and direct visible emission. To further explore this relationship, we compared the ratio of $^1D_2$ emission to $^3P_0$ emission of samples with various Li^+ doping concentrations. For both sets of emission peaks, a 10 nm wavelength range was used, employing 603-613 nm for the $^1D_2$ emission and 547-557 nm for the $^3P_0$ emission. The latter group of peaks was chosen to represent the $^3P_0$ emission since it

does not overlap any of the $^1D_2$ peaks and is of comparable intensity, though other ranges could have been used. The resultant ratio provides a metric for cross relaxation, wherein a higher $^1D_2/^3P_0$ emission ratio implies higher incidence of CR. These results are shown in Figure 30 using a reverse order y-axis to highlight the similarity to the trend of UC efficiency versus Li^+ concentration seen in Figure 23A. Therein, the X2-1500º and 5% Li^+ materials show both equivalent CR and UC intensity. Cross-relaxation then decreases and reaches a minimum at 10% Li^+, corresponding to the most intense UC. At 15% Li^+, however, the similarity breaks down as UC intensity drops suddenly, while CR remains steady. This indicates that the sharp decrease in UC intensity at this codoping concentration is not due to a reversal in the lithium's effect on clustering, but rather likely arises because the solubility limit of Li^+ in the material is being surpassed, causing a higher degree of impurities and an overall deterioration of optical performance.

The aforementioned hypothesis predicting the presence of localized groups of $Li_Y''/V_O^{\cdot\cdot}/Pr_Y^x$ provides a reasonable mechanism by which Li^+ works to disperse clusters of activator ions; Pr^{3+} ions are allowed more space at their particular site, due to the vacancy and replacement of the neighboring Y^{3+} with a smaller Li^+ ion, and the surrounding structure is less distorted by the presence of Pr^{3+}. The Pr^{3+} ions could thus enter the material without causing the cumulative strain that leads to the formation of clusters.

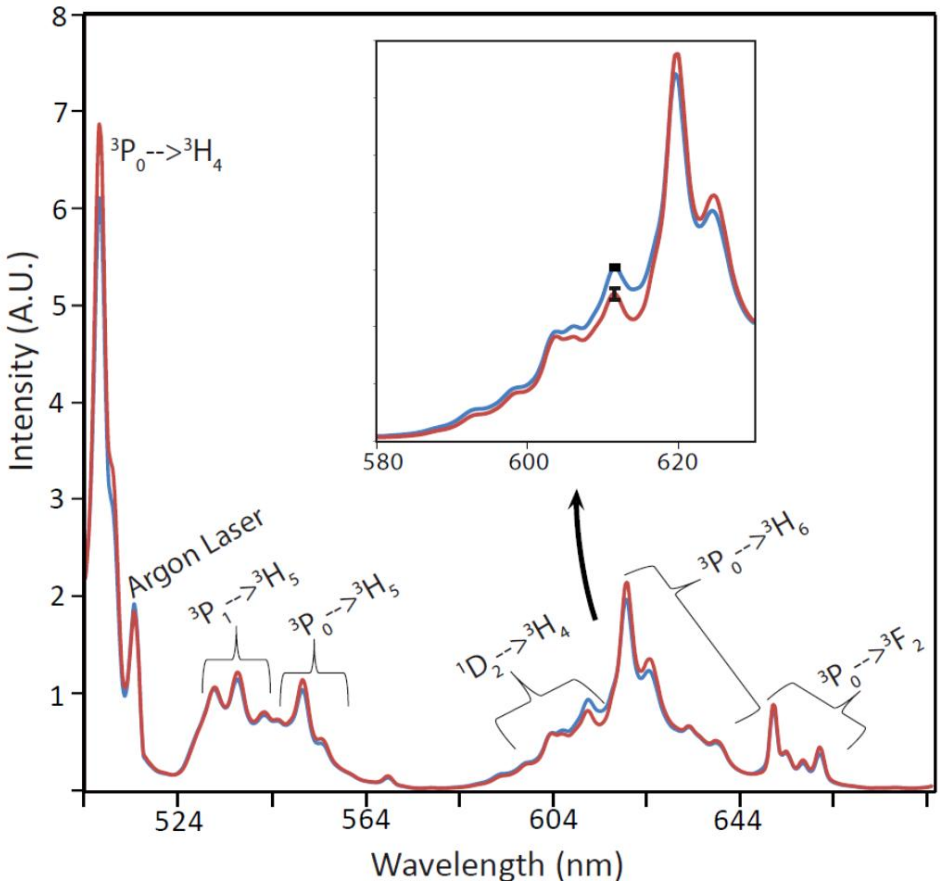

Figure 29. Stokes emission of X2-1500º phosphor (blue) and 10% Li^+-doped phosphor (red) excited to the $^3P_0$ state by argon laser at 488 nm (the peak at 514 nm arises from incomplete filtration of the laser beam). Inset shows zoomed-in view including the $^1D_2$ emission region with error bars. Reprinted with permission from Cates et al. (2012). *J. Phys. Chem. C* 116(23): 12772-12778. Copyright 2012, American Chemical Society.

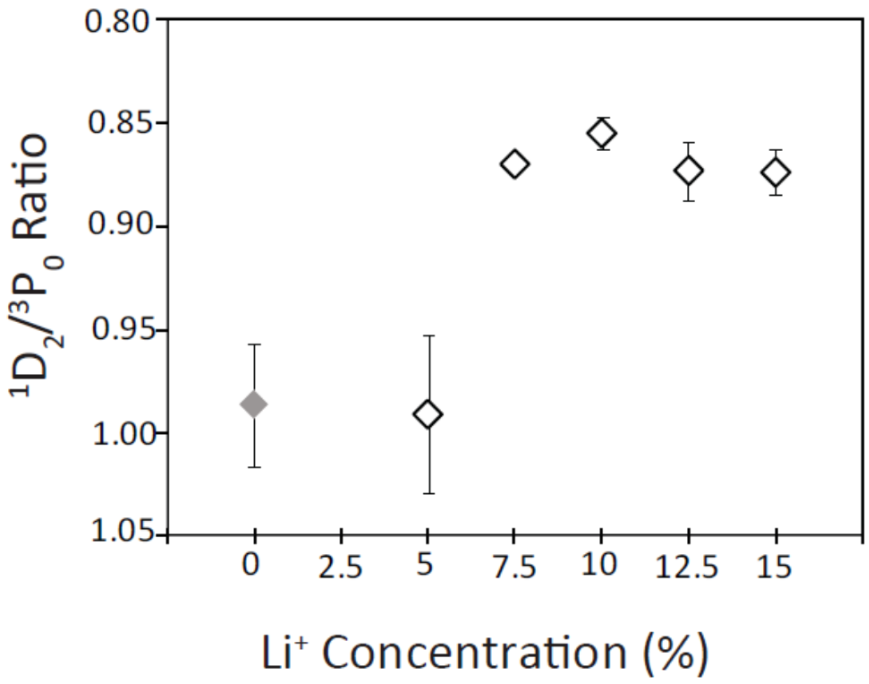

Figure 30. Observed cross-relaxation expressed as the ratio of emission intensities from the $^1D_2$ Stark states at 603−613 nm to that of the $^3P_0$ emission peaks at 547−557 nm, with reverse-order y-axis. The point at 0% (gray) shows the X2-1500° material. Reprinted with permission from Cates et al. (2012). *J. Phys. Chem. C* 116(23): 12772-12778. Copyright 2012, American Chemical Society.

5.4. Conclusion

The enhancement of visible-to-ultraviolet UC in $Y_2SiO_5:Pr^{3+}$ by Li^+ doping was attributed to a flux effect, a phase change from the X1 to the X2-Y_2SiO_5 polymorph, and a reduction in activator cross-relaxation, with the final two mechanisms having the greatest impact. Lithium is able to readily induce the change in structure because it is a small ion that occupies Y^{3+} sites, while oxygen vacancies likely exist as a charge-balancing defect and have important structural implications. While some of the enhancement in UC can be achieved without Li^+ via extended or high-temperature annealing, the ability to disperse Pr^{3+} clusters makes codoping with Li^+ a uniquely effective way of increasing UC efficiency in this phosphor system.

5.5. Acknowledgements

This section contains contributions from coauthors and was published in: *Cates, Ezra L., Angus P. Wilkinson, Jae-hong Kim (2012). "Delineating Mechanisms of Upconversion Enhancement by Li^+ Codoping in $Y_2SiO_5:Pr^{3+}$."* *The Journal of Physical Chemistry C* ***116****(23): 12772-12778.*

CHAPTER 6

UPCONVERSION UNDER POLYCHROMATIC EXCITATION

6.1. Introduction

Many of the applications of UC materials described in this work involve non-laser excitation, including utilization of sub-bandgap radiation in solar cells [109, 133, 218], photocatalyst enhancement [141, 144], and the central topic of UC-AMS. In all such applications, the intended excitation source is sunlight or ambient light, which in comparison to the more common laser excitation, offers a much broader wavelength spectrum of incident photons with lower intensity. The UC emission resulting from low power irradiation is not intense enough to be detected by typical photodetection equipment. Therefore, the emission under low-power excitation is typically inferred from monochromatic laser-excited emission measurements, or quantified using indirect methods related to the application. Numerous authors have reported infrared-to-visible UC in Er^{3+}-doped materials by exciting with ~1500 nm laser radiation and subsequently measuring an increase in photocurrent when the material is applied as a backing layer to photovoltaic cells exposed to solar simulators [106, 219]. Similarly, the work by Qin et al. showed that YF_3:Yb^{3+},Tm^{3+} emits UVA radiation when excited by a 980 nm diode laser and further demonstrated that, when coated with a photocatalytic TiO_2 shell, the

composite particles were capable of degrading organic dye solutions under filtered sunlight [144].

The efficiency of UC materials under broad-spectrum irradiation is likely to be significantly different, compared to monochromatic excitation, when viewed from an incident photon utilization perspective. For example, due to their electronic structures, multiple different stepwise ESA schemes can be imagined for ions like Er^{3+} and Tm^{3+}, wherein the initial excitation is initiated by a photon of one wavelength, while the second excitation involves a photon of a significantly different energy with each step having a separate absorption coefficient depending on the precise energy of the incident photon. Tian and Reddy reported that UV emission by Tm^{3+} was enhanced five-fold when excited by both 458 and 585 nm beams [220]. Also, Kramer et al. showed that infrared-to-visible UC emission in $LaCl_3:Er^{3+}$ showed different peak ratios depending on whether it was excited at 980 nm, 810 nm, or both [221].

In this chapter, several mechanisms of ESA in $Y_2SiO_5:Pr^{3+}$ that result in UVC emission only under polychromatic visible light excitation are hypothesized. The mechanisms shown in Figure 31(A and B) have been investigated, wherein the material was irradiated with wavelengths in the blue/violet range to achieve UC emission and then other colors are added to evaluate the increase (or decrease) in UC. The goal was to study how multiple simultaneous wavelengths might be utilized to better understand the performance of UC materials under broadband excitation.

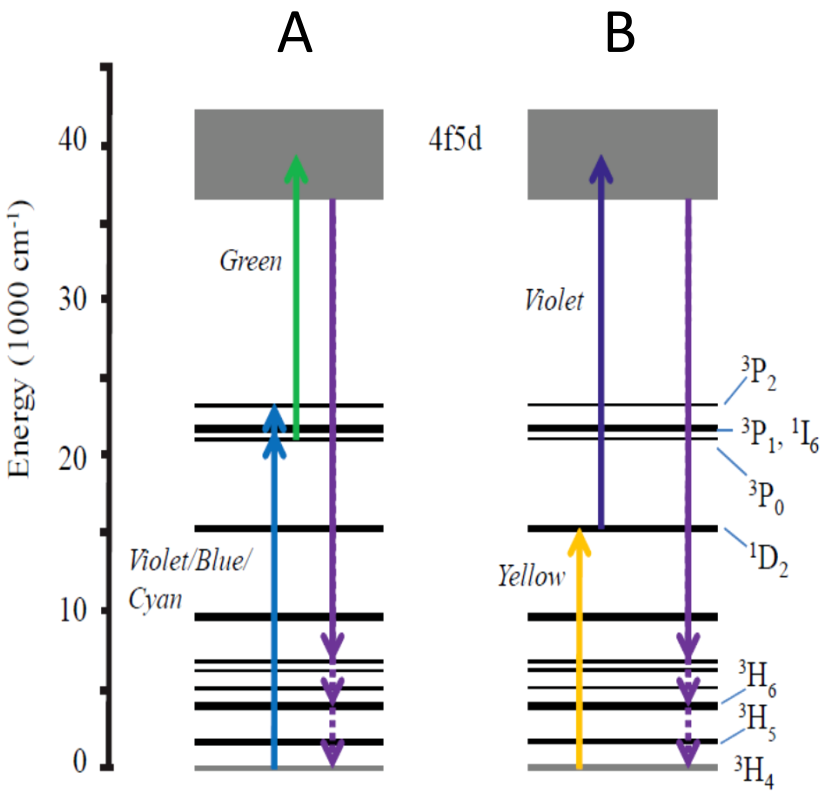

Figure 31. Hypothesized visible-to-ultraviolet UC mechanisms in $Y_2SiO_5:Pr^{3+}$ via excited state absorption under two-color excitation scenarios.

6.2. Experimental Section

The specific phosphor material employed in this work was X2-Y_2SiO_5:Pr^{3+}(1.2%), Li^+(10%) which was synthesized as described in Section 5.2.1, and is referred to in this section as YSO:Pr^{3+}. The codopant, Li^+, is added to maximize UC efficiency as detailed previously [159]. The host crystal, X2-Y_2SiO_5, is a monoclinic system with space group I 2/a, and Pr^{3+} ions can occupy two distinct Y^{3+} sites, both of C1 point symmetry [159].

Spectroscopic studies were conducted using packed powder samples at room temperature, with excitation sources including: an argon ion laser for 488 nm ("cyan") or 515 nm ("green") beams of ~130 mW maximum power each; a 447 nm ("violet"), 100 mW DPSS laser; and a 589 nm ("yellow"), 100 mW DPSS laser. Beams were combined using dichroic mirrors, as shown in Figure 32. Luminescence decay measurements were taken by exciting the phosphors with a 7 ns, 3 mJ pulse from an optical parametric oscillator set at 447 nm and pumped by an Nd:YAG laser. The yellow DPSS laser mentioned above was also used in the decay studies. The 4f5d UV PLE spectrum was recorded using a Shimadzu RF-5301PC spectrofluorophotometer and phosphor powder suspended in ethanol.

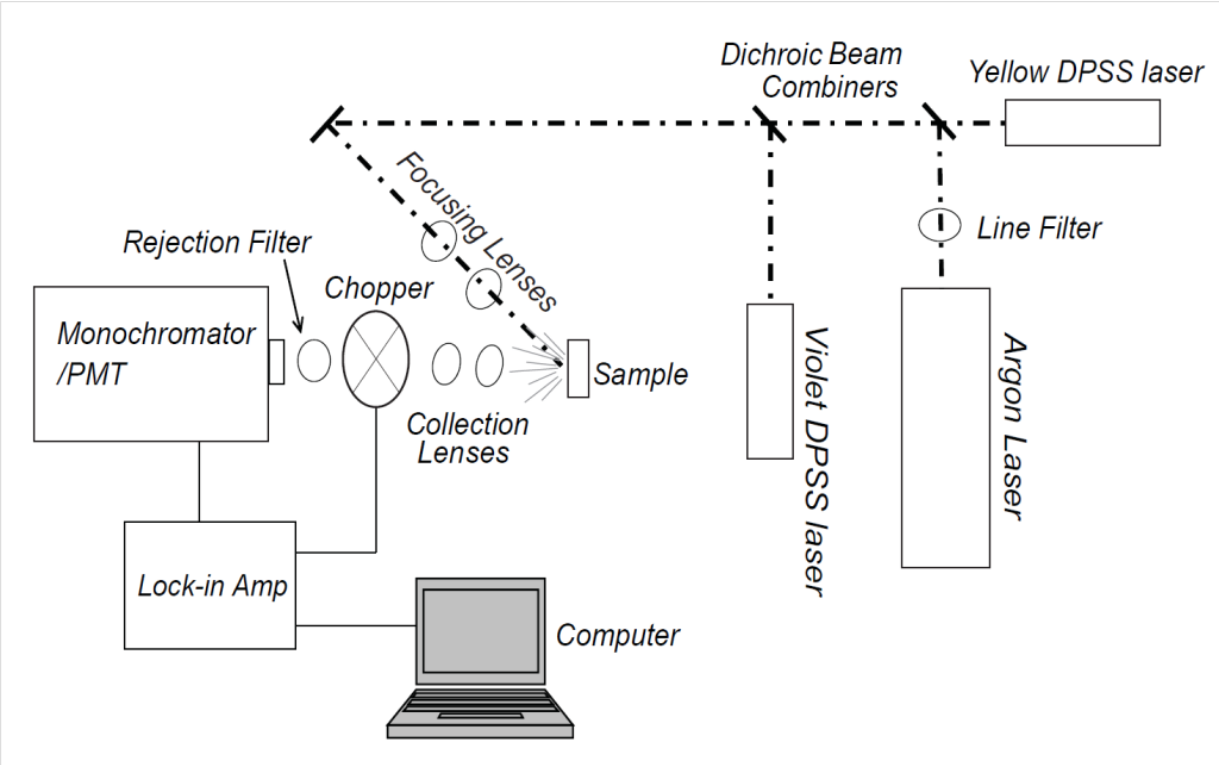

Figure 32. Photoluminescence spectroscopy system with multicolor excitation beam.

6.3. Results and Discussion

Before considering UC under polychromatic excitation, the mechanisms occurring during monochromatic excitation must first be clarified based on the experiment results. Figure 33B shows the UC emission spectrum of YSO:Pr^{3+} under violet laser excitation. In this case, the intensity of UC emission under violet excitation could not be quantitatively compared to that under cyan excitation, due to the different beam diameters of the two lasers; however, the two-photon PLE spectrum measured by Hu et al. indicates that these wavelengths result in approximately the same quantity of UC emission (Figure 14) [172]. Nonetheless, multiple UC mechanisms must be considered for violet excitation and will differ from those associated with cyan irradiation, which is more commonly reported for Y_2SiO_5:Pr^{3+} [104, 172, 173]. Under cyan excitation (488 nm), Pr^{3+} electrons will be excited to the $^3P_1$,$^3P_0$ states, and UC can proceed through either ETU or ESA [173]. Under violet excitation, however, it is likely that $^3P_J \rightarrow$ 4f5d ESA is negligible. The Stokes emission spectrum in Figure 33C shows that the lowest ^3P_J level, $^3P_0$, is of approximately 20,325 cm^{-1}, indicated by the emission peak at 492 nm. Violet excitation results in $^3H_4 \rightarrow {}^3P_2$ transitions, followed by rapid relaxation to the $^3P_0$ state. Absorption of a second violet photon of 447 nm would then result in a total energy of 42,700 cm^{-1}. The absorption coefficient of this second step depends on the density of accepting 4f5d states around this energy. Such information can be obtained using direct excitation with photons of 42,700 cm^{-1}, *i.e.* 234 nm. Figure 33A shows the 4f5d PLE

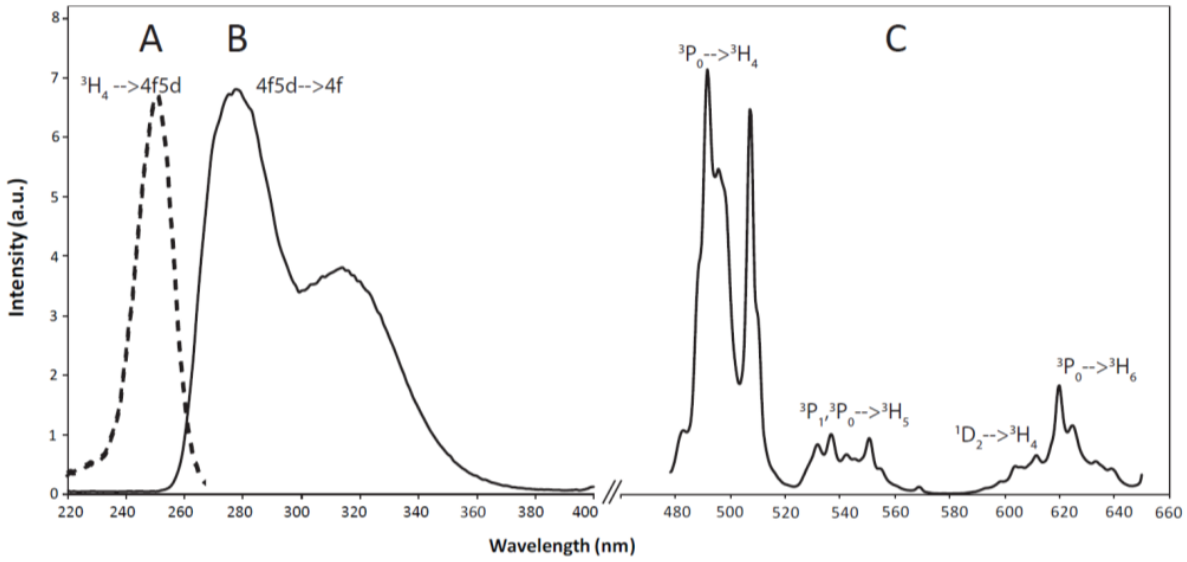

Figure 33. (A) 4f5d photoluminescence excitation spectrum of YSO:Pr^{3+}, λ_{em} = 277 nm; (B) 4f5d→4f upconversion emission under 447 nm excitation (emission spectrum under direct 251 nm excitation is qualitatively identical); (C) Visible light emission under 447 nm excitation. Intensities of each spectrum have been normalized.

spectrum which indicates that photons of this wavelength do not result in significant UV emission; thus there is a low density of states at this energy and $^3P_J \rightarrow$4f5d ESA involving violet photons is relatively improbable. Still, ETU may occur under violet excitation as in Figure 13 [159], and is likely of equivalent efficiency to ETU under cyan excitation.

An additional UC mechanism should be considered, wherein Pr^{3+} ions are first excited by violet photons and then relax to the $^1D_2$ level through either multiphonon emission or cross relaxation, as has been reported [72, 159, 215]. This state has a longer lifetime than the ^3P_J levels [217], since the relaxation transition is spin-forbidden, and $^1D_2 \rightarrow$4f5d ESA may occur upon absorption of a second violet photon. The $^1D_2$ term is split into four Stark states with the state of lowest energy residing at approximately 16,500 cm^{-1}, depending on the crystallographic site [214]. Absorption of a violet photon from this state will result in a total energy of 38,873 cm^{-1}, corresponding to a single photon of 257 nm. The 4f5d PLE spectrum indicates a significant probability of excitation to the 4f5d band occurring at this photon energy. However, predicting the $^1D_2 \rightarrow$4f5d transition probability in this fashion does not take into consideration changes in spin multiplicity. The PLE spectrum (Figure 33A) reflects the photon energies that are likely to result in $^3H_4 \rightarrow$4f5d transitions; since the $^3H_4$ ground state has triplet spin multiplicity, spin-allowed transitions involving triplet $5d^1$ states will contribute most to the UV PLE, which will be minimally influenced by singlet $5d^1$ states. It is these singlet $5d^1$ states, however, which are most likely to accept an electron during a spin-allowed $^1D_2 \rightarrow$4f5d ESA transition. Laroche et al. in fact showed that the PLE spectrum of $^3P_J \rightarrow$4f5d excitation exhibited a slightly different energy distribution than for $^1D_2 \rightarrow$4f5d transitions in Pr^{3+}-doped fluoride crystals due to the spin nature of the different states [169].

It is thus difficult to predict whether ETU between two ions at the ^3P_J level or $^1D_2 \rightarrow$ 4f5d ESA is more responsible for the UC emission under violet light excitation based on these PLE data, though ETU is generally considered 100 times more efficient than ESA [52]. Also worth considering is the possibility of a separate ETU mechanism occurring between an ion at the $^3P_2$ level and one at the $^1D_2$ level, wherein one participant transfers energy and the other becomes excited to the 4f5d band. However, considering that this mechanism requires virtually no vibronic relaxation among ^3P_J levels after initial excitation in order to maintain sufficient total energy, it is assumed to be largely negligible, though further investigation beyond the scope of this work is required to confirm this assumption.

Possible polychromatic UC mechanisms were first explored by using a combined green and violet excitation beam. There are no 4f states of Pr^{3+} which allow ground state absorption of green light at 515 nm, and therefore no UV emission was detected when green light alone was used in a control test. However, the mechanism hypothesized in Figure 32A predicts that green photons can contribute to UC by initiating $^3P_0 \rightarrow$ 4f5d transitions following excitation within the range of 445-490 nm. This was investigated by exciting YSO:Pr^{3+} with the combined violet + green laser beam and comparing the resultant UV emission to that produced by monochromatic violet excitation. Figure 34 shows that UC increases significantly upon addition of green light and confirms that green photons can assist in populating the 4f5d states. Our experimental setup did not allow a quantitative assessment of the efficiency of green photon ESA relative to violet excitation intensity because variations in beam size and divergence will result in different

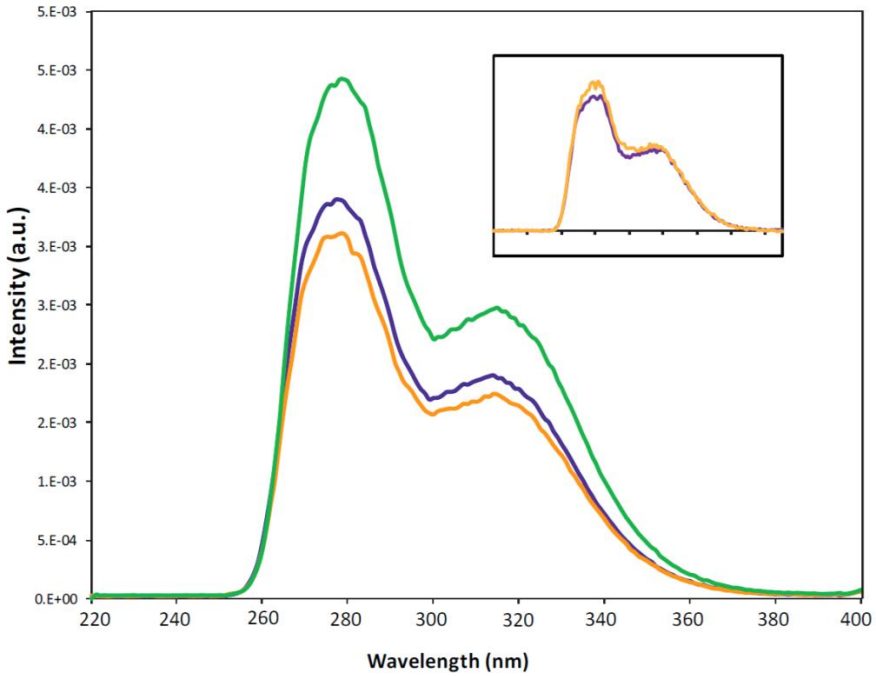

Figure 34. Upconversion emission spectra of YSO:Pr^{3+} under 100 mW violet (purple), violet+green (green), and violet+yellow (yellow) excitation. Inset shows violet (purple) and violet+yellow (yellow) with violet laser at low power of 20 mW.

intensities experienced by the sample, even if both lasers are set to emit at the same power. However, it can be inferred that a finite range of green wavelengths can result in this enhancement, as long as the energy sum, $E_{^3P_0} + h\nu_{green}$, falls within range of the 4f5d PLE spectrum. Thus 512.4 nm is predicted to be the most effective wavelength, wherein $E_{^3P_0} + h\nu_{512.4\ nm}$ = 39,840 cm^{-1} (251 nm) and an electron is excited to the energy where the PLE spectrum peaks. Additionally, the initial $^3H_4 \rightarrow {}^3P_J$ excitation required for the mechanism is not restricted to violet light, but may also occur through blue or cyan excitation.

Further mechanisms were probed under combined yellow and violet irradiation. Above, it is asserted that UC emission can result from $^1D_2 \rightarrow$ 4f5d ESA under violet excitation; it thus follows that the mechanism in Figure 31B is also possible, wherein a Pr^{3+} ion is directly excited to the $^1D_2$ state by a yellow photon (589 nm) and then ESA of a violet photon occurs. The presence of yellow light in a polychromatic excitation beam may therefore serve to enhance UC emission, although yellow alone did not result in any UC emission in a control test. This hypothesis was investigated by exciting YSO:Pr^{3+} with a combined 447 nm/589 nm beam and it was found that sometimes the UC signal was enhanced (Figure 34 inset) and sometimes it was lower than with violet excitation alone (Figure 34). Whether or not yellow photons were beneficial or detrimental to UC emission was found to depend on the violet laser power intensity. In Figure 35A, the percentage enhancement of UC emission upon adding yellow excitation at a constant 100 mW is plotted versus violet laser power. At lower violet intensities, UC emission increases when the yellow laser is switched on. As the violet excitation intensity is

increased, no effect is observed at ~70 mW and addition of yellow then results in lower UC emission at powers above 70 mW. This result was unexpected, since it was predicted that yellow photons would increase UC intensity, or at least have no effect, rather than cause any decrease. One hypothesis that was considered was the existence of some type of cross-relaxation occurring betweens Pr^{3+} ions in the ^3P_J state and ions in the $^1D_2$ states, such that initiating *Ground*$\rightarrow{}^1D_2$ excitations with yellow light serves to lower the lifetime of the intermediate ^3P_J manifolds and thus decrease UC efficiency. To investigate, the radiative decay of $^3P_J \rightarrow {}^3H_4$ luminescence under violet and violet + yellow excitation, monitored at 507 nm, was measured and is shown in Figure 35B. It is clear that there is no decrease in lifetime upon introducing yellow excitation, disproving the above hypothesis. For completeness, regression curves were fit to the decay data which showed biexponential decay, indicating that two separate transitions contribute to emission at 507 nm, with τ = 695 ns and 2.25 μs without yellow excitation and 725 ns / 2.25 μs with yellow excitation. It is speculated that the short-lived luminescence arises from $^3P_2 \rightarrow {}^3H_5$ emission, while the longer portions of the decay curves are due to $^3P_0 \rightarrow {}^3H_4$ transitions.

To further elucidate the role of yellow photons in YSO:Pr^{3+} UC, the excitation power dependence of UV emission was studied. Figure 36A shows integrated UC emission intensity versus violet excitation power plotted in a double logarithmic scale. The slope of the regression line was found to be n=1.7, suggesting a two-photon process, as expected [165]. However, when the same experiment was conducted in the presence of continuous yellow excitation fixed at 100 mW, the violet power dependency shows a multi-phase character (Figure 36B). The data can be divided into three regions of different slopes: within 4-25 mW violet power, n = 1.3 and UC emission shows a near-

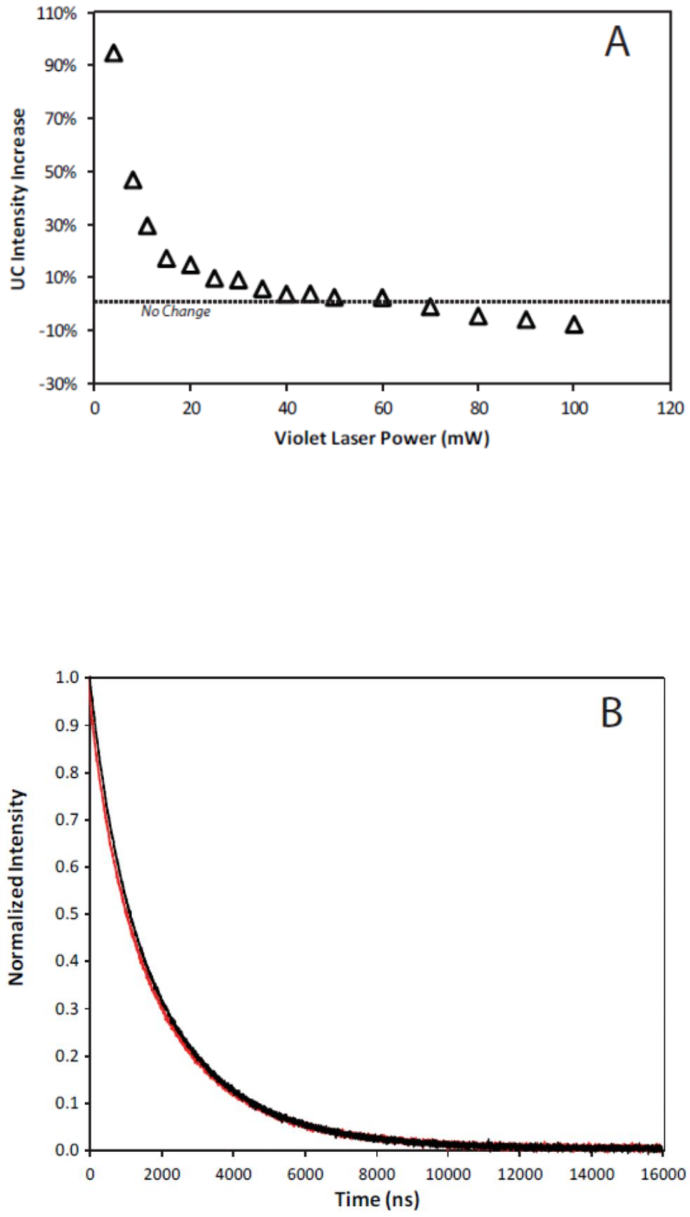

Figure 35. (A) Percentage increase in upconversion emission intensity by YSO:Pr^{3+} upon adding yellow excitation to an existing violet excitation beam; (B) Luminescence decay of ^3P_J emission monitored at 507 nm under pulsed violet excitation (red) and pulsed violet excitation plus continuous yellow excitation (black).

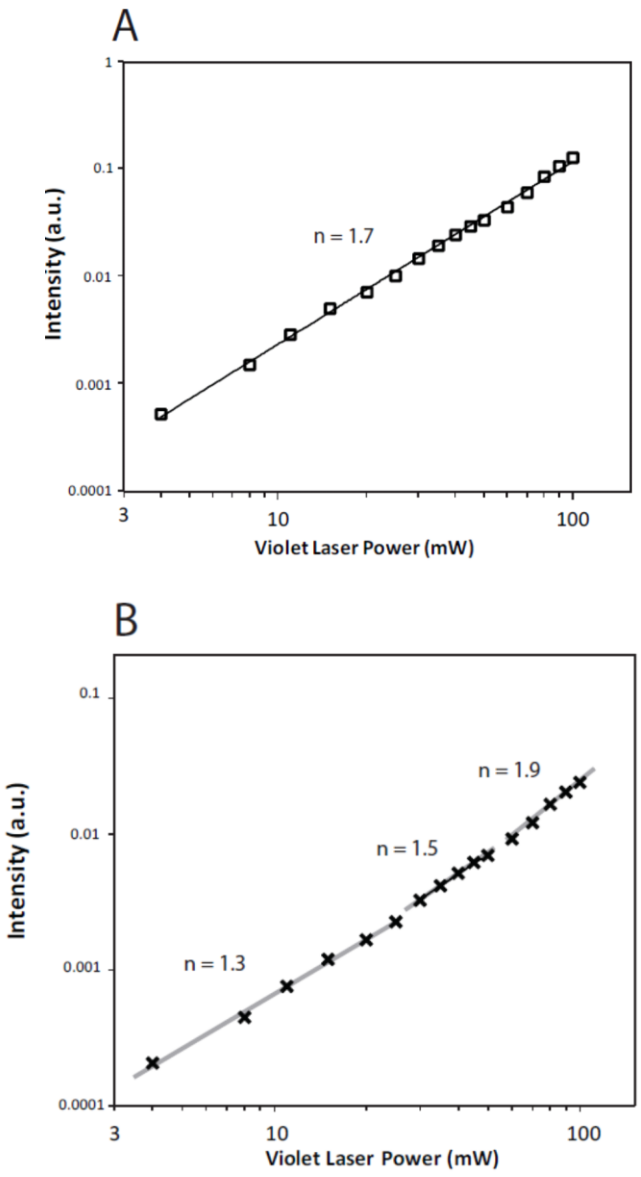

Figure 36. (A) Upconversion emission intensity violet laser power dependence; (B) Violet laser power dependence in the presence of 100 mW yellow excitation. Slopes of the regression lines are indicated.

linear power dependence; within 30-60 mW, n = 1.5; and within 70-100 mW, n = 1.9, achieving quadratic dependence. The transition power between the first two phases is somewhat subjective, yet the transition to n = 1.9 is more distinct. This laser power, 70 mW, is also the violet laser power at which addition of yellow light transitions from UC-enhancing to UC-detracting, as described above.

A linear relationship between UC emission and excitation power is known to indicate saturation of the intermediate states [222] and allows explanation of our results. Under low-power violet excitation, UC is relatively inefficient, regardless of the possible mechanism. Upon adding 100 mW yellow excitation, the $^1D_2$ states become nearly saturated and incoming violet photons have a high probability of being absorbed to result in $^1D_2 \rightarrow$ 4f5d ESA; this results in the enhanced UC emission and linear violet power dependence. As the violet excitation power is increased, the more efficient ETU mechanism accounts for a greater portion of the UC emission. The occurrence of both ESA showing linear power dependence and ETU with quadratic dependence, results in a slope of 1.5 for the middle portion. Ultimately, the ETU mechanism, which does not involve the $^1D_2$ states, becomes dominant at 70 mW and the violet power dependence is fully quadratic. At these higher powers where ETU is dominant, it appears that addition of yellow light does not significantly contribute to UC but serves primarily only to deplete the population of ground-state Pr^{3+} ions, and thus the number available for $^3H_4 \rightarrow {}^3P_J$ excitation and subsequent ETU; therefore UC intensity decreases. The data in **Figure 36**B were reproducible, though only for a particular range of power densities, *i.e.* the size of the focal spots of the combined beam on the sample. Other results showed less discernible multi-phase character with overall slopes of ~1.5.

The above experiments were also conducted using cyan + yellow excitation, leading to different results than the violet light experiments. Therein, addition of the 100 mW yellow beam served to decrease UC emission at high cyan laser power and had no observable effect at low powers (data not shown). Since cyan photons are not of great enough energy to result in $^1D_2 \rightarrow$ 4f5d ESA, yellow light irradiation results only in increasing the $^1D_2$ Stokes emission and depleting ground state Pr^{3+} ions under high power cyan excitation.

6.4. Conclusion

It was hypothesized that many UC mechanisms that have not been explored in the past literature may occur under polychromatic excitation due to ESA involving two different excitation wavelengths. These results confirm that green and yellow light can contribute to visible-to-UV conversion in YSO:Pr^{3+} , though under high violet laser power, addition of yellow light detracted from UC emission, which was attributed to saturation effects. Under low-power, broad-band irradiation, such as sunlight, the excitation power would not be great enough to achieve saturation of intermediate states. Thus, extrapolating from the results, a significant range of yellow, green, blue, and violet photons will all contribute to UVC emission by Pr^{3+} to some extent. While UC materials are typically studied using monochromatic excitation, similar upconversion of polychromatic light is likely possible for many lanthanide-doped phosphors and should be considered when studying UC for applications such as solar cells and other ambient light-activated materials. Furthermore, while not likely in the YSO:Pr^{3+} system due to

the activator's electronic structure, ETU mechanisms involving two-color excitations may also be feasible, with greater efficiency than ESA under low power irradiation.

6.5. Acknowledgements

This section contains contributions from Jaehong Kim and has been submitted for publication.

CHAPTER 7

LUTETIUM OXYFLUORIDE HOST CRYSTALS FOR EFFICIENT Pr^{3+} UPCONVERSION

7.1. Introduction

7.1.1. Background

With successful demonstration of the UC-AMS concept having been achieved, discovery of more efficient visible-to-UVC conversion systems is now essential. In Chapter 4, it was shown that the X2-Y_2SiO_5:Pr^{3+},Li^{+}(,Gd^{3+}) coatings were capable of inactivating *B. subtilis* spores at a rate of approximately 1-log reduction per 10 d direct exposure to visible fluorescent lamps. To achieve practical applicability in hospital or other commercial settings, however, it is likely that an inactivation rate that is one order of magnitude faster must be attained. Still, one must consider the variation in UVC susceptibility among various microorganisms. The bacterial spores used in the assessment have an uncharacteristically high UVC resistance when compared to typical pathogens; the required dose for 1-log inactivation of *B. subtilis* spores in water is over 5 times greater than that for *E. coli* [50], and their resistance is even higher on dry surfaces [223].

Nevertheless, an effective UC-AMS should function under ambient light conditions of considerably lower intensity than used in the previous experiments and it is presumed that the X2-Y_2SiO_5:Pr^{3+},Li^+ system cannot offer adequate conversion efficiency in this scenario. While the investigation of enhancement mechanisms by Li^+ in Chapter 5 revealed that efficiency of Pr^{3+} UC can vary widely within a given host composition, it is believed that the upper limit of phosphor performance was achieved and different host crystals must be tested in pursuing higher conversion rates. Though Y_2SiO_5 is an attractive material due to its chemical stability, its relatively high phonon cutoff energy of 970 cm^{-1} [224] allows high rates of multiphonon and cross relaxation, thus failing the general criteria of an optimal UC host.

It is hypothesized that doping of Pr^{3+} into a host crystal with significantly lower phonon cutoff frequency will result in more efficient visible-to-UVC UC, given that other important parameters are satisfied. Two key nonradiative energy loss mechanisms that could be alleviated by a low-phonon host are the multiphonon $^3P_0 \rightarrow {}^1D_2$ relaxations and phonon-assisted cross relaxation [159, 217], both of which decrease the lifetime of the $^3P_0$ intermediate state via relaxation to $^1D_2$. In development of infrared-to-visible UC phosphors, fluoride crystals have emerged as the standard for low-phonon energy, high efficiency hosts [52-54, 225]; however, this strategy may not necessarily be applied to the Pr^{3+} UC relevant to this research. The host-dependent edge energy of the 4f5d manifold must lie at low enough energy to be within range of excitation by two visible light photons (excitation spectrum must peak at <42,100 cm^{-1}), yet at high enough energy such that radiative transitions from the band edge result in UVC emission (band edge >36,000 cm^{-1}), as illustrated in Figure 37.

Two theories are typically applied in predicting the energy of the d orbital excited states in a given host. According to crystal field theory, increasing field strength of the surrounding ligands will induce greater crystal field splitting, lowering the 4f5d band edge energy [171]. However, the position of the 5d band in Pr^{3+} is more consistently explained by the nephelauxetic effect, wherein bond covalency determines the baricenter of the 5d band [192]. Thus, less electronegative ligand atoms result in greater bond covalency and the valence electrons are delocalized, lowering the energy of the 5d excited state transitions. For more electronegative atoms and oxyanion ligand groups, the 5d excited state energies are raised due to electron localization.

The objective herein is thus to find a host material that has both low phonon energy and appropriate 4f5d band energy for UC by Pr^{3+}. Table 5 lists some common host materials and properties of interest, including host phonon cutoff energy, Pr^{3+} intermediate state lifetime in each host, and Pr^{3+} 4f5d absorption peak energy in each host. However, none of the hosts fit both criteria with the exception of Cs_2NaYCl_6, which is chemically unstable due to moisture reactivity [168]. Yet it is interesting to note that both Y_2O_3 and YF_3 have low maximum phonon energies, with the former having excessively low 4f5d edge energy and the latter excessively high edge energy. In effect, "averaging" of these two crystals may result in an ideal host, pointing toward investigation of an unconventional class of materials – Rare earth oxyfluorides (REOFs) – for use in Pr^{3+} UC. Passuello et al. recently reported on the optical properties of lutetium oxyfluoride doped with Pr^{3+} [226]. While UC luminescence was not studied, the

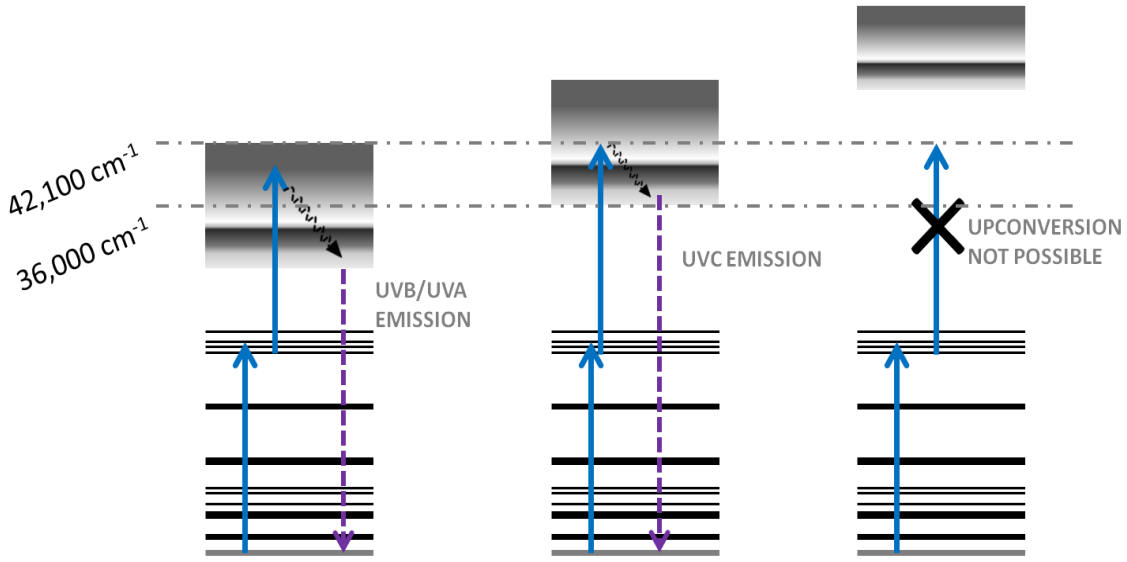

Figure 37. Energy levels of Pr^{3+} ions in different host crystals, wherein the 4f5d band is too low in energy (left), of desirable energy (middle), and too high in energy (right).

Table 5. Properties of crystals and Pr^{3+} as dopants in each respective host. Data from Donegá et al. [227], unless otherwise referenced.

Host Crystal	*Phonon Cutoff Energy (cm^{-1})*	*$^3P_0$ Lifetime (μs)*	*4f5d Absorption Peak (cm^{-1})*
$LiYF_4$	570	48	50,000
YF_3	550 [228]	---	~52,600 [179]
YOCl	560	7.1	40,000
La_2O_3	500	3.6	35,000
La_2O_2S	500	3.0	33,000
Y_2O_2S	500	2.7	33,000
Lu_2O_3	600	---	36,200
Y_2O_3	600	---	35,800
$YNbO_4$	830	0.3	Host CT overlap
Cs_2NaYCl_6	300 [168]	118 [168]	~41,000 [168]
X2-Y_2SiO_5	970 [224]	2.3*	39,840*

* Data from present work.

authors claimed that this class of materials possesses low phonon energies (though no reference was provided) and gave an emission spectrum of what was believed to be $Lu_{10}O_9F_{12}:Pr^{3+}$, which peaked at ~260 nm. This finding further confirms that REOFs may offer uniquely pertinent host crystals, and in this chapter, lutetium oxyfluorides and their feasibility as efficient Pr^{3+} UC hosts are investigated.

7.1.2. Structural Properties of Rare Earth Oxyfluorides

Reports in the literature of phosphors utilizing oxyfluoride hosts have seen a recent surge, possibly due to the realization that substitution of F^- into oxide crystals, accompanied by alteration of the cation component, can result in a plethora of compounds having superior luminescence and being isostructural to many known phosphor cyrstals [226, 229-234]. Phosphors have thus been prepared using REOFs including LaOF [235, 236], $Y_xO_{x-1}F_{x+2}$ [230, 233, 234], and $Lu_xO_{x-1}F_{x+2}$ [226], as well as calcium-aluminum and strontium-aluminum oxyfluorides [231, 232]. The REOF's present particular challenges with regard to phase purity and control. When prepared with an oxide to fluoride ratio of 1:1, the typical result is a rhombohedral phase, which is most stable for LaOF [237]. For Lu^{3+} and Y^{3+} oxyfluorides, however, this phase decomposes to RE_2O_3 upon heating in air, and even during solid state synthesis in inert atmosphere is difficult to achieve in pure form due to an abundance of possible Vernier phases [237-239]. Therein, a unique fluorite-related structure may be obtained for any local oxide-to-fluoride ratio, having the general form $RE_xO_{x-1}F_{x+2}$ and an orthorhombic unit cell [226, 237-240]. Müller et al. published a tentative

phase diagram of lutetium oxyfluoride, which depicts the limits of the Vernier region, shown in Figure 38.

While the diagram does not indicate any temperature dependence of the phases within the region, Müller wrote that achieving single-phase materials for XRD analysis required "considerable experimental effort" [239]. Similarly, Wen et al. recently synthesized $Y_xO_{x-1}F_{x+2}:Ln^{3+}$ phosphors and were unable to assign the structure of their materials to any one Vernier phase, though efficient luminescence was observed [241]. Finally, Schmid et al. contributed that while the Vernier phase concept is a convenient model, the Y^{3+} and Lu^{3+} oxyfluorides in fact show incommensurate phase structures that lack short-range periodicity in one lattice direction [242]. It is therefore evident that the ability to synthesize the above materials while achieving a precise and well-defined structure is elusive, though it is not definitive that such an achievement is required in order to produce effective REOF phosphors.

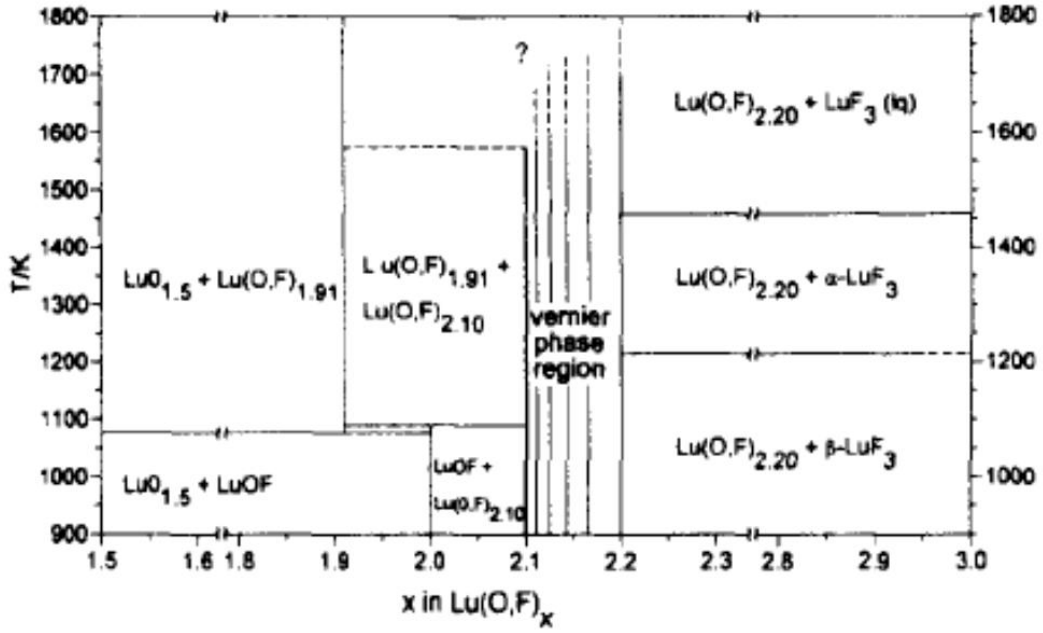

Figure 38. Tentative phase diagram of the Lu_2O_3-LuF_3 system. Reprinted from Müller, J. H., T. Petzel, et al. (1997). "Phase study of the binary system Lu_2O_3-LuF_3 in the temperature range 1000–1750 K." Thermochimica Acta **298**(1–2): 109-114 with permission from Elsevier. Copyright 1997.

7.2. Experimental Section

7.2.1. Syntheses

Stock chemicals employed in this work were purchased from Sigma Aldrich, unless indicated otherwise, and include: Lu_2O_3 (99.99%, Stanford Materials), $Pr(NO_3)_3 \cdot 6H_2O$ (99.99%), NH_4F (99.99%), NH_4OH, and HNO_3 (trace metal grade). The solid state method was employed through three basic steps: (1) Preparation of $Lu(NO_3)_3$ solutions; (2) Coprecipitation of $Lu(NO_3)_3/Pr(NO_3)_3$ solutions with NH_4F to produce $LuF_3:Pr^{3+}$; and (3) mixing of trifluoride powder with some portion of Lu_2O_3, pressing into a pellet, and heating in argon atmosphere. Specifically, 0.177 mol of Lu_2O_3 was added to 66 mL of boiling HNO_3 diluted with an equal volume of water. Once completely dissolved, the solution was brought to 100 mL with water for a final concentration of 1.77 M. Next, 12 mL of $Lu(NO_3)_3$ solution was added to a flask along with an appropriate amount of 0.2 M $Pr(NO_3)_3$ aqueous solution, such that the desired concentration of Pr^{3+} in $Lu_xO_{x-1}F_{x+2}$ would ultimately be achieved (typically ~1%). This solution was brought to 100 mL with water, then under vigorous stirring, the following were added: 0.300 mL 1/10 diluted NH_4OH (28% NH_3, aqueous) and 20 mL of 0.345 M NH_4F (aqueous) to precipitate white, solid $LuF_3:Pr^{3+}$ hydrate. The precipitate was then cleaned and separated by three cycles of rinsing/centrifugation, then dried in an oven at 104 ºC. The powder was then transferred to an alumina boat and placed in a tube furnace with flowing argon (ultra-high purity) and heated at 800 ºC for 2 h to remove any internal moisture.

To prepare the oxyfluorides, stoichiometric amounts of $LuF_3:Pr^{3+}$ and Lu_2O_3 were added to a mortar with a small amount of ethanol and wet-milled by hand for 10 min. The powder mixture was then dried in an oven, pressed into pellets at ~1000 MPa using a hydraulic press and steel die of 10 mm diameter. The pellets were placed in alumina boats, then, under flowing argon atmosphere, were heated to 400 ºC for 1 h, then to 700-1100 ºC at a rate of 12 º/min and held for various durations, then cooled naturally. It should be noted that the thermocouple of the employed furnace was positioned outside of the process tube and the actual temperature inside the tube was believed to be considerably cooler than what was programmed.

A range of Lu_2O_3: LuF_3 (O:F) ratios were used during syntheses, ranging from 0.33 to 0.75. However, these values reflect only the stoichiometry used during synthesis, while in reality, the coprecipitation method used to produce the $LuF_3:Pr^{3+}$ reactant results in substantial incorporation of OH^- defect anion groups into the fluoride crystals [243, 244]. During annealing, the hydroxide component will react to hydrolyze fluoride ions, resulting in a HF molecule exiting the structure and leaving behind O^{2-} ; thus, the end result is a greater fraction of oxide and higher final value of *x* compared to using pure fluoride reactants. Another consequence is that the *x* value of the samples are unknown until analyzed, and achieving a desired final O:F required some trial and error.

7.2.2. Characterization

Optical properties of the sintered $Lu_xO_{x-1}Fx_{n+2}:Pr^{3+}$ pellets were measured using the PLS system described in Chapter 3. Upconversion emission was measured under

excitation at 447 nm, employing a 400 nm short-pass filter at the monochromator entrance. Stokes emission under the same excitation wavelength was measured using 450 nm and 475 nm long-pass filters to completely omit laser background signal. Emission from the $^1D_2$ states under direct excitation was obtained using a 589 nm laser and 600 nm long-pass filter. X-ray diffraction was conducted as in Chapter 5. Since the phosphor pellets were generally curved, and may have had different predominant phase structures on the concave and convex sides, XRD was performed on thin, flat flakes that were broken from the pellets. Diffraction patterns were analayzed by the Rietveld method using GSAS and EXPGUI software [206, 207].

7.3. Results and Discussion

7.3.1. Solid State Reaction Behavior

The temperature and duration of annealing was observed to have a pronounced effect on pellet appearance, UC luminescence, and crystal structure, as will be discussed throughout this section. However, it was apparent that the product of temperature × heating time (T×t) was a more important determining factor in predicting synthesis outcome, rather than the individual variables. Thus, annealing at 800 ºC for 36 h could produce a very similar material to annealing at 1100 ºC for 1 h. Reproducibility of experimental conditions and resultant materials were poor during early stages, yet synthesis procedures were eventually refined such that samples with nearly identical properties could be obtained. This type of behavior is similar to previous reports of RE

oxyfluorides and supports the suspected semi-disordered nature of these materials [239, 241, 242].

Upon longer or hotter annealing of the compressed LuF_3/Lu_2O_3 mixtures, the resulting ceramic pellets showed a tendency to become curved to various extents, with the concavity most often occurring on the face-down side of the pellet, closest to the wall of the process tube. This effect became more prominent for decreasing *x*, while at the highest *x* value ($x = 10$), the pellets remained flat. In all cases of curved samples, the convex side showed only weak visible-to-UV UC, as determined by PLS, and also demonstrated weaker Stokes emission in the visible range (data not shown). Poor Stokes emission is a possible indicator of poor crystallinity, *i.e.* presence of numerous crystalline and amorphous phases with a high density of grain boundaries and associated defects. Such a state was confirmed by XRD analysis of a flake from this portion of a pellet; as seen in Figure 39 (top), the pattern shows a relatively high number of reflections compared to the other samples, and weak diffracted intensity. In contrast, the diffraction pattern of the concave side shows strong diffracted intensity and presence of fewer crystal phases (Figure 39, middle).

Multiple possible causes explaining the final two-sided macro-structure of the $Lu_xO_{x-1}F_{x+2}:Pr^{3+}$ ceramics were investigated. Since the furnace tube was continuously purged with argon, the presence of a cooling effect by the gas flow and resultant radial temperature differential was considered. This effect was ruled-out, however, since minimizing the gas flow and propping the alumina boat at different heights within the tube did not produce different results. Reaction of the exposed side of the pellet with residual atmospheric moisture was also excluded since previous experiments showed that

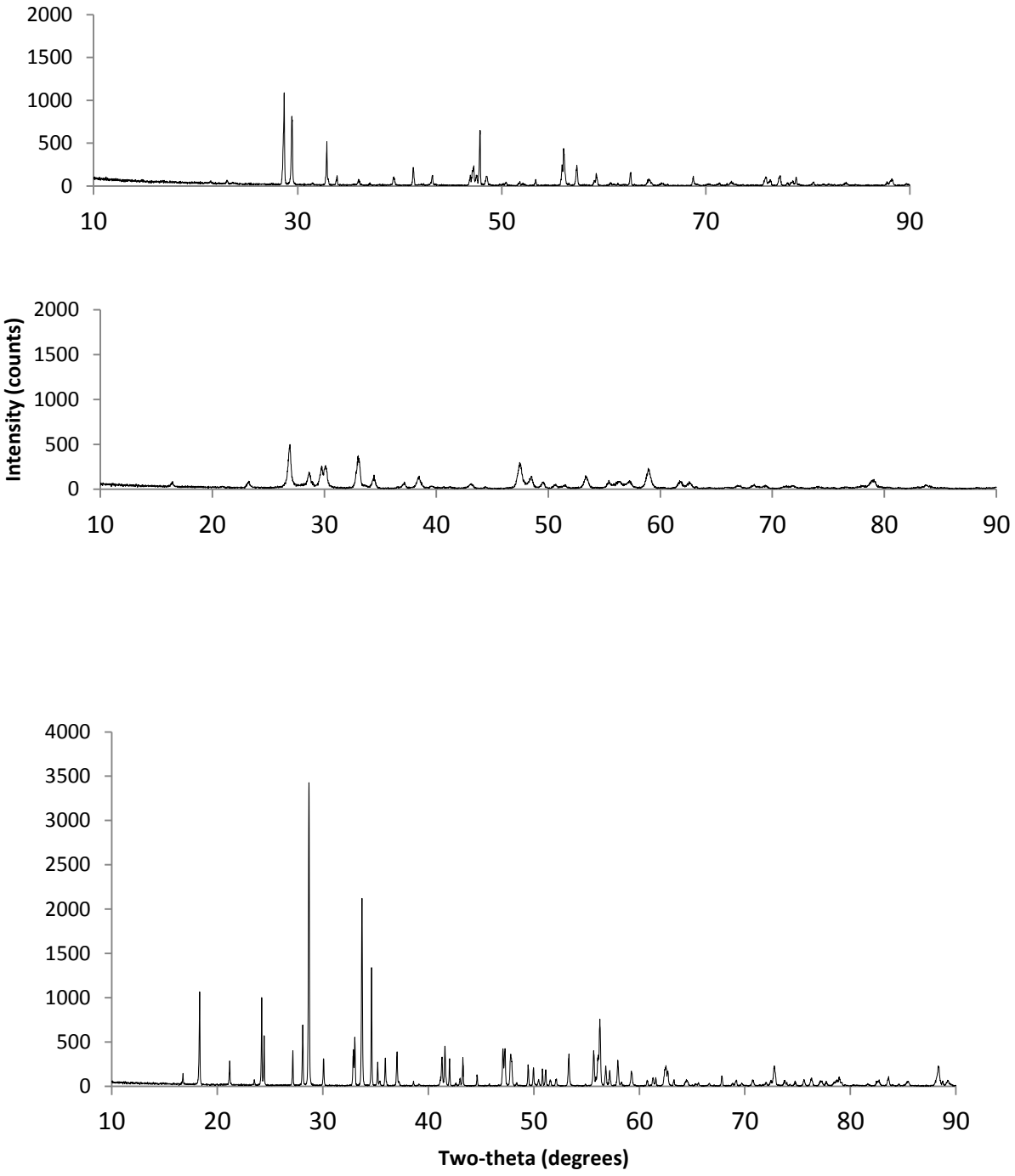

Figure 39. X-ray diffraction patterns of $Lu_xO_{x-1}F_{x+2}:Pr^{3+}$ ceramic pellets. **Top**: Pellet showing most intense Pr^{3+} UC emission, peaking at 259 nm (fragment from concave side). **Middle**: previous, fragment from convex side. **Bottom**: Pellet showing Pr^{3+} UC emission peaking at 310 nm (fragment from concave side).

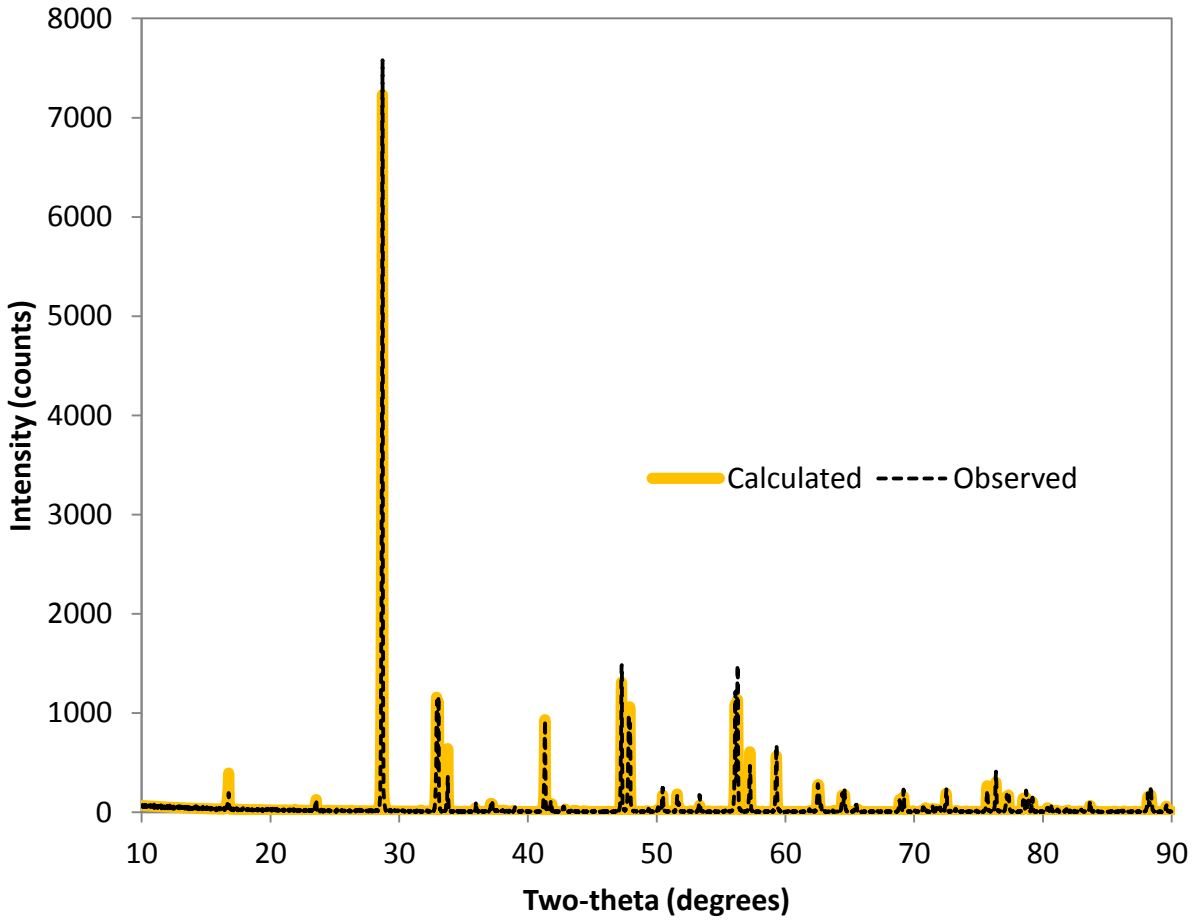

Figure 40. X-ray diffraction pattern and Rietveld fit of $Lu_xO_{x-1}F_{x+2}:Pr^{3+}$ showing single phase $Lu_7O_6F_9$ structure.

annealing in the presence of air at high temperature discolors the sample. Besides, hydrolysis reaction with moisture would serve to increase the O:F ratio, producing a denser material layer [238], which is inconsistent with a convex curvature. A feasible explanation was revealed after annealing a sample for 36 h at 1000 ºC. After this long heat treatment, the convex side of the pellet had a distinct green tint, indicating a high concentration of Pr^{3+} ions, while the concave side appeared white. Diffusion of Pr^{3+} through the ceramic material to one side of the pellet would be expected to cause lattice expansion due to the large ionic radius of Pr^{3+} compared to Lu^{3+} [146], which could be responsible for formation of a convex curvature. Furthermore, the limited solubility of Pr^{3+} – also due to its radius relative to Lu^{3+} – is expected to result in poor phase purity at higher concentrations. Finally, excessive activator concentration results in energy quenching mechanisms [54, 178], which could explain the observed poor luminescence on the convex side of the pellets. Incorporating the lack of curvature in the $x = 10$ sample into this theory, however, is difficult at present time.

7.3.2. Luminescence

The intensity of the UC emission upon 447 nm excitation was used as a deciding factor in refining the solid-state synthesis and selecting the "desired" $Lu_xO_{x-1}F_{x+2}$ materials from among many Vernier phases produced during early stages. The most efficient visible-to-UVC UC was found to occur when the $Lu_xO_{x-1}F_{x+2}$ crystal structure resulted in a Pr^{3+} 4f5d band edge-energy conducive to UV emission centered at 259 nm. This UC spectrum, shown in Figure 41, was observed for numerous pellets subjected to

different heat treatments, occasionally only on localized regions. The most intense spectrum is depicted in the figure, with the emission of X2-Y_2SiO_5:Pr^{3+} pellets for comparison. The oxyfluoride material shows 2.5-times greater overall UC emission and 4.5-times greater emission in the UVC range. In general, it was found that this emission type was dominant for pellets with low *x*-values and was the first phase to form on the concave side after short-duration annealing. This characteristic emission was observed even after reaction at only 700 ºC, although the intensity was weak. For more oxide-rich reactant stoichiometries and longer annealing time, structures that resulted in relatively red-shifted 4f5d→4f UC emission were encountered. Phases that showed emission peaks centered at ~263 nm, ~265 nm, and ~310 nm were most frequently observed in these cases; Table 6 summarizes the results of these preliminary syntheses.

After some experimental trial, an O:F of 0.538 was selected as the ideal ratio for achieving the desired 259 nm UC emission, and a furnace temperature of 1000 ºC was believed to be most effective in this respect, as well. Figure 42 shows the UC emission of $Lu_xO_{x-1}F_{x+2}$:Pr^{3+} (O:F = 0.538, Pr^{3+} concentration = 1 at.%) synthesized at 1000 ºC for various durations. Annealing times between 1 and 30 min resulted in the most intense UC emission, while further annealing caused gradual decrease in UC intensity in addition to slight red-shifting of the 4f5d→$^3H_4$ peak center. Figure 42 (inset) shows a decreasing trend of the 4f5d band edge-energy as annealing time increases via plotting of the emission center of gravity. This behavior indicates a dynamic crystal environment surrounding the activator ions during reaction at 1000 ºC, which could be the result of either transition from a kinetically stable Vernier phase to a more thermodynamically stable structure, or of relocation of Pr^{3+} ions to preferred sites. Since the O:F of the entire

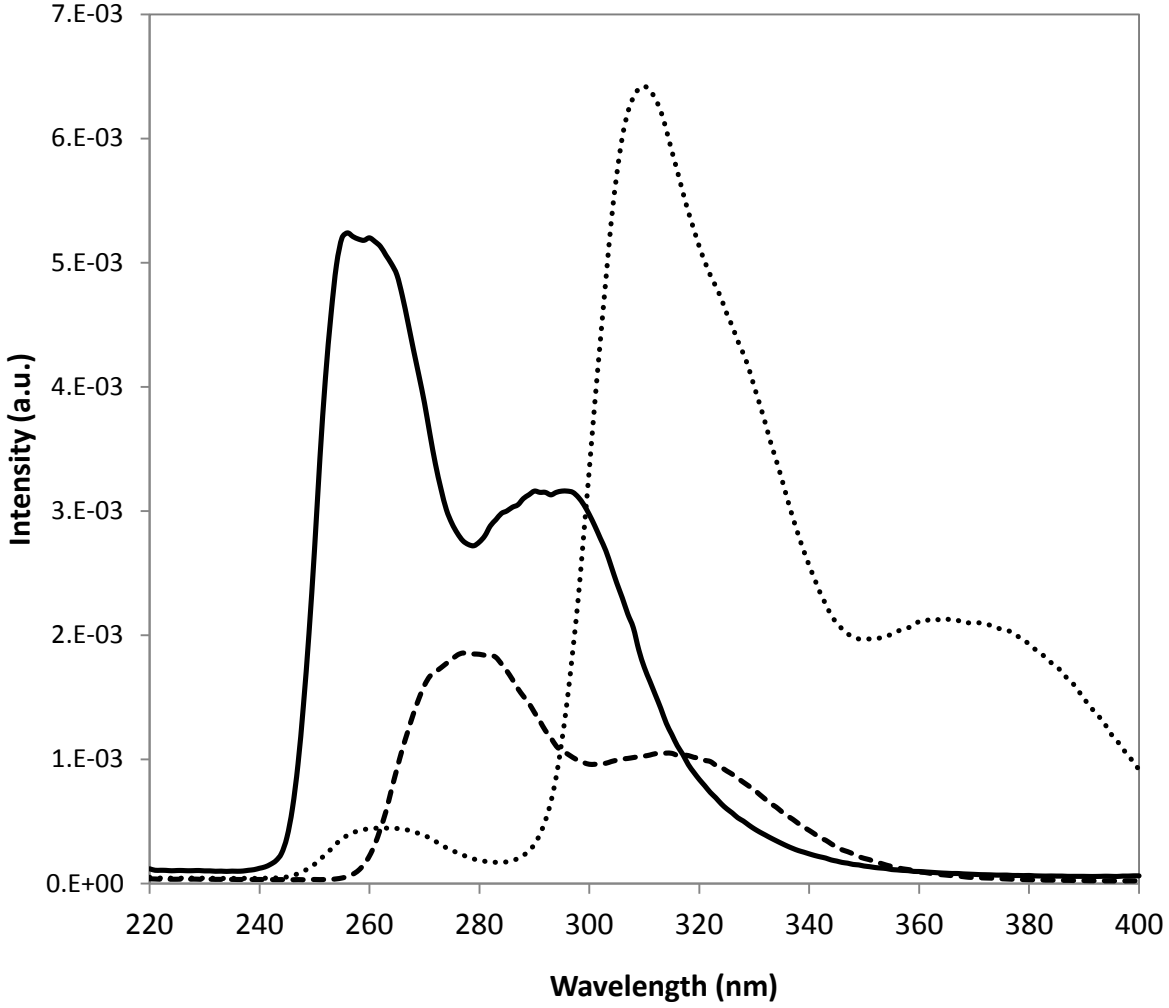

Figure 41. Upconversion emission spectra of Pr^{3+}-doped ceramic pellets under 447 nm excitation. **Solid:** sample with most intense UVC emission (O:F = 0.538, 1000 ºC for 1 min). **Dotted:** O:F = 0.75, 900 ºC for 34 h. **Dashed:** X2-Y_2SiO_5:Pr^{3+} reference material.

Table 6. Results of preliminary $Lu_xO_{x-1}F_{x+2}:Pr^{3+}$ ceramic syntheses. Peak center indicates the center of the strongest UC emission peak. Emission intensity label designates semi-quantitative intensity relative to X2-$Y_2SiO_5:Pr^{3+}$ reference phosphor, with "weak" indicating less than half of reference intensity; "medium" is roughly equivalent to reference; and "strong" is more intense than reference.

Lu_2O_3:LuF_3 Ratio Added	Annealing Temperature (ºC)	Annealing Duration (h)	Peak Center (nm)	Emission Intensity
0.538	1000	0.5	259	Strong
0.571	900	36	Multiple	Weak
0.571	800	10	262	Medium
0.625	800	10	260	Medium
0.667	800	10	263	Medium
0.625	900	36	259	Strong
0.625	900/1100	10/3	312	Strong
0.750	900	34	312	Strong

pellet will not change during annealing in inert atmosphere, any change in *x* at the concave surface layer of the pellet must result in an opposite change elsewhere, as O^{2-} and F^- ions relocate; this notion is consistent with the observation of curved pellets and differing optical properties on each side. Furthermore, the tendency of Pr^{3+} to diffuse preferentially to one side may affect the phase preference. Regardless of the nature of this structural evolution occurring over time, it ultimately leads to an arrangement of atoms that is less favorable to UC.

Intensity of $^3P_J \rightarrow 4f$ Stokes emission under 447 nm excitation, shown in Figure 43, demonstrated a dependence on annealing time that differed from the UC results. Therein, intensity increased as the pellets were subjected to longer annealing at 1000 ºC, until the trend reverses between 1.5 and 2 h. While the efficiencies of UC mechanisms are sensitive to many structural phenomena, Stokes luminescence is more indicative of overall material quality, *i.e.* phase purity and crystallite size, and affected less by many of the factors influencing UC. It is expected that crystallite size in a ceramic material will continually grow as annealing time is increased; however the state of phase purity is likely a more complicated situation in materials such as oxyfluorides, wherein a continuous range of incommensurate phases may exist. As the crystallites grow, the reduction in boundary defects may be partially offset by formation of new phases and epitaxial regions. Occurrence of changing phase structure was evidenced by shifting of the 4f5d band edge, as described above, and occurs only slightly until 2 h, then shifts more rapidly. Thus, it is speculated that the decrease in Stokes intensity at 2 h is related to an accelerating atomic rearrangement, which introduces significant defects beginning around this time.

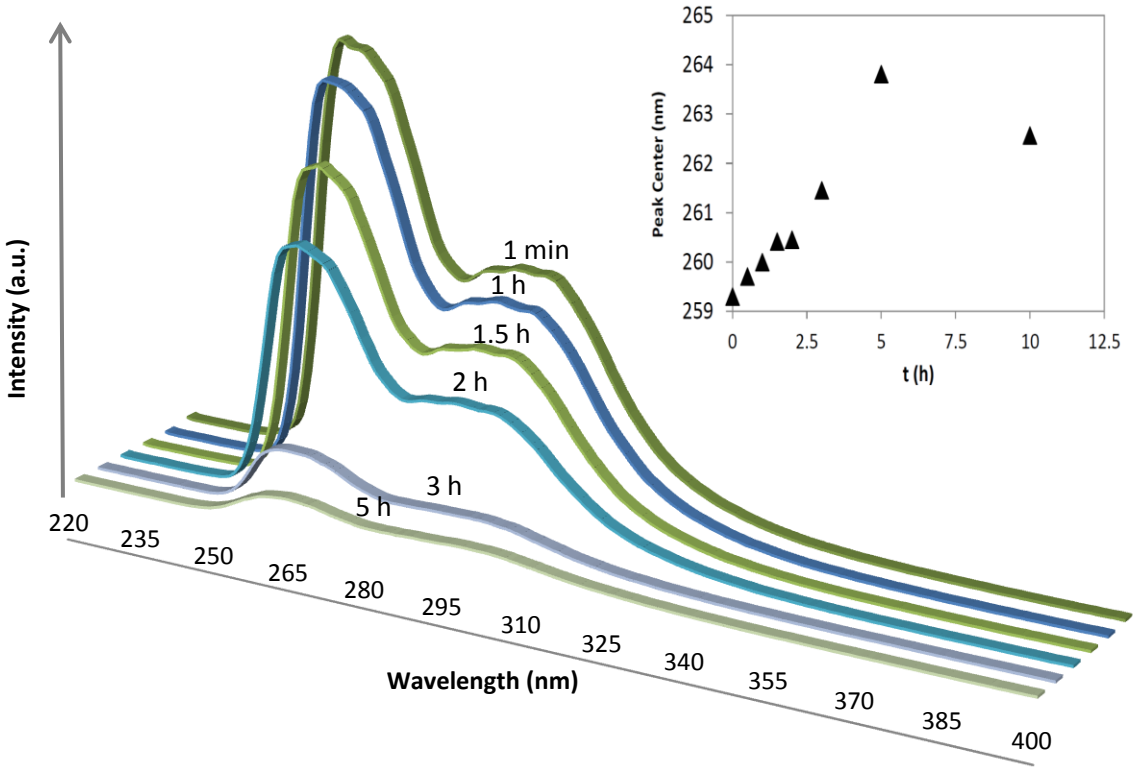

Figure 42. Upconversion emission spectra of $Lu_xO_{x-1}F_{x+2}:Pr^{3+}$ samples prepared using O:F = 0.538 at 1000 ºC for various durations. **Inset:** UVC peak center of gravity versus annealing time.

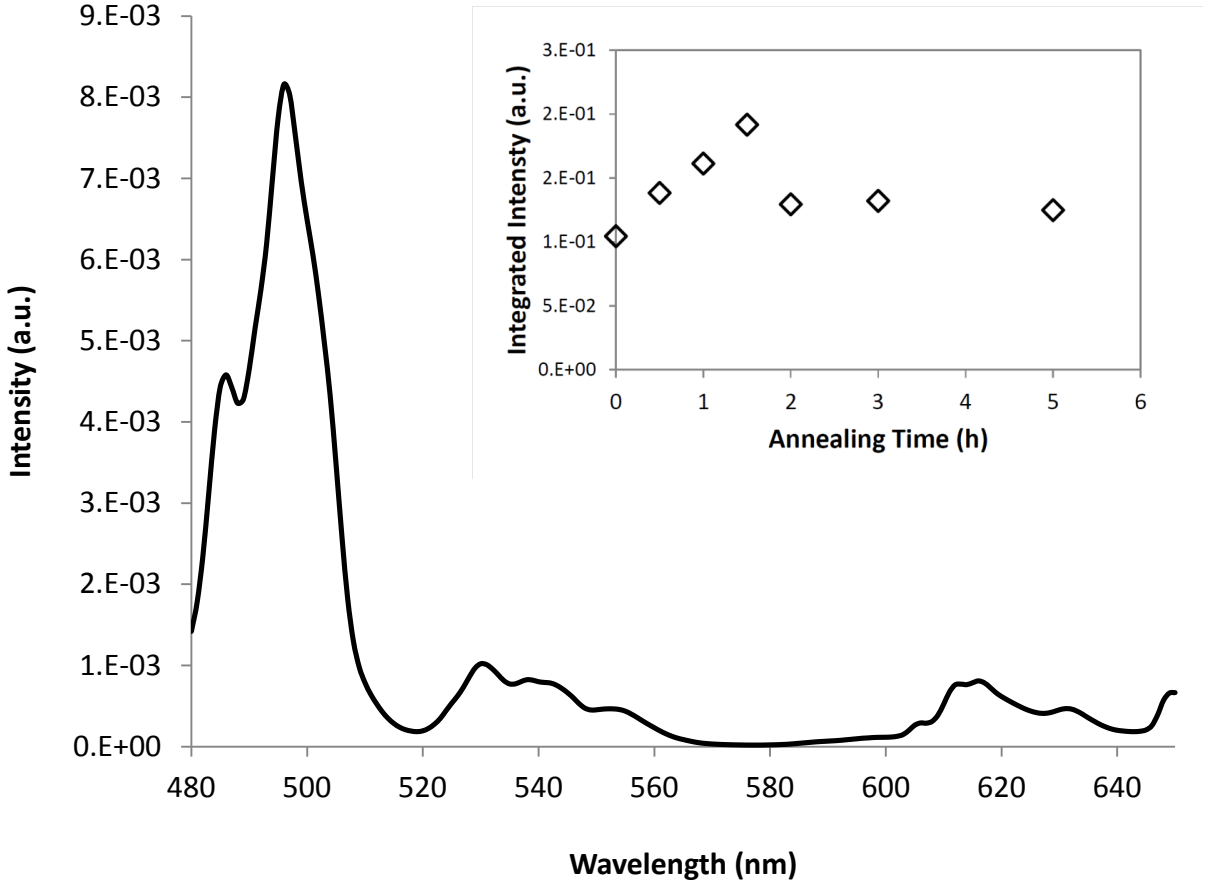

Figure 43. Visible range Stokes emission of $Lu_xO_{x-1}F_{x+2}:Pr^{3+}$ prepared using O:F = 0.538 at 1000 ºC for 1.5 h, excited at 447 nm. **Inset:** Integrated intensities of samples with various annealing times. Emission spectra of samples were (nearly) qualitatively identical.

The steady decrease in UC intensity from 0-5 h at 1000 ºC is not explained by the above phenomena, since the factors causing an increase in Stokes emission would be expected to have a positive influence on UC as well. However, the experiments in Chapter 5 revealed that Pr^{3+} UC efficiency is particularly sensitive to activator clustering and the associated cross-relaxation [159]. It was also found, therein, that a quantitative measure of CR is obtained by comparing the intensity of $^1D_2$ emission relative to $^3P_0$ emission. A similar analysis was conducted for these materials, first by probing the wavelength range of $^1D_2$ emission under 589 nm excitation; it was located at 600-640 nm and peaked at 606 nm (data not shown). To minimize overlap with ^3P_J transitions, the range of 602-611 nm was chosen for the indicator of $^1D_2$ emission intensity, while the range of 643-658 nm was chosen to represent $^3P_0$ emission. The latter range was chosen since it was the closest $^3P_0$ peak that did not overlap with $^1D_2$ emission, though other peaks could have been used.

Figure 43 (inset) shows Stokes emission of different samples in the 595-660 nm range under 447 nm excitation. From 0 to 1 h, a distinct increase in the relative intensity of the peak at 606 nm was observed, revealing greater incidence of cross relaxation. However, after 1.5 h annealing, the peak diminishes again, even though a corresponding increase in UC was not observed for the 1.5 h treatment. These data do not provide a complete explanation of the UC behavior as it relates to detailed changes in crystal structure, however, the stark initial rise in the $^1D_2/^3P_0$ ratio suggests that Pr^{3+} clustering and cross relaxation likely play an important role, in addition to other effects.

7.3.3. Crystal Structure

Thorough crystallographic study of the synthesized oxyfluoride materials has yet to be completed; however, XRD analysis revealed which Vernier phase leads to the most intense Pr^{3+} UC emission. Figure 39 shows two diffraction patterns obtained from pellet fragments showing strong UC emission with (nearly) qualitatively identical spectral distribution. The patterns were compared to many reference patterns including $Y_5O_4F_7$, $Y_6O_5F_8$, $Y_7O_6F_9$, $Y_{17}O_{15}F_{21}$,YOF, and Lu_2O_3 [§]. The only one of these phase structures that appeared to be present in the samples was $Y_7O_6F_9$. Rietveld analysis showed that the fragment of the sample prepared using an O:F ratio of 0.571 and annealing at 1100 ºC for 19 h[**] was pure-phase $Lu_7O_5F_9$. The other sample fragment (O:F = 0.538, 1000 ºC for 1 min) showed peaks that were also assigned to $Y_7O_6F_9$, yet an additional unidentified phase was present. These results suggest that the appearance and maturation of this structure results in the most efficient UC, until Pr^{3+} ions diffuse to thermodynamically favored sites and begin to cluster, causing cross relaxation and poorer UC efficiency. Upon additional annealing, Pr^{3+} UC diminishes further and is believed to be a result of rearrangement of the anion substructures to form new Vernier phases. Analysis of samples annealed for longer periods yielded diffraction patterns that could not be analyzed with the available reference patterns. Since the O:F of the whole pellets cannot change, localized segregation of disparate Vernier phases may be occurring during annealing times longer than ~5 h, with diffusion and concentration of Pr^{3+} acting as a possible driving force. Lastly, the stoichiometry of this Vernier phase translates to an

[§] More reference patterns exist in the literature for the yttrium analogs, which are isostructural to lutetium oxyfluoride Vernier structures.
[**] This material could not be reproduced using these synthesis conditions.

O:F of 0.667, which is higher than what was used during synthesis and further confirms the existence of significant unintended oxygen content in the "LuF_3:Pr^{3+}" reactant.

7.4. Conclusion

A new class of visible-to-UVC upconverting materials has been successfully synthesized through solid state reaction, utilizing Pr^{3+} ions in a low-phonon energy oxyfluoride host. The material demonstrated kinetically instable crystal structures, with different embodiments showing Pr^{3+} emission of differing intensity and spectral distribution. One phase was isolated as the most effective for UC, achieved most reproducibly with a Lu_2O_3:LuF_3 ratio of 0.538 and heating at 1000 ºC for 1-30 min. Analysis by XRD revealed a phase match to the $Y_7O_6F_9$ structure, and UC emission in the UVC range was 4.5 times greater than the reference phosphor. Further work is needed to achieve better understanding of the crystal phase behavior so that pure, homogenous UC materials can be fabricated and so that Pr^{3+} concentration and distribution may be fine-tuned for optimized UC. Strategies to achieve these goals are discussed in Chapter 9.

CHAPTER 8

PREDICTING THE EFFECT OF MATERIAL AND ENVIRONMENTAL PARAMETERS ON ESTIMATED ANTIMICROBIAL EFFICACY

8.1. Introduction

The work in this dissertation is focused on proof-of-concept and material development of UC-AMS's and thus does not include detailed numerical simulation of photophysical processes or microbiological responses; however, the experimental results within, and existing data in the literature, provide sufficient foundation for generating approximate quantitative estimates of how effectively a UC-AMS will perform under certain conditions. In this chapter, such estimates are generated under "best case" and "worst case" scenarios to elucidate the validity of the UC-AMS concept and expose whether or not it is reasonable to assume that it can become an effective technology in the future, given sufficient research effort. The proposed alternative application of utilizing visible-to-UVC conversion for solar drinking water disinfection purposes is also discussed, and, for all applications, the analysis is restricted to UC by Pr^{3+}-doped materials. A wide array of factors may determine the efficacy of any given UC-AMS system, and can be grouped into three categories: (1) environmental factors; (2) phosphor performance properties; and (3) microbial response factors. Many considerations are

listed in Table 7, though it is not an exhaustive list. The two most important parameters are undoubtedly excitation light intensity/spectral distribution and UC quantum efficiency. Two extremes may be considered for the former: moderate ambient room light (*e.g.* office or public restroom) and direct tropical sunlight. Ambient room light is more pertinent to the application of visible-to-UV UC materials for preventing disease transfer on surfaces and may range from office/hallway light in the low intensity regime, up to hospital room/food processing workspace conditions in brighter scenarios. Additionally, the fluorescent lamps currently used for indoor lighting produce a variety of emission spectra, depending on the phosphors employed. In analyzing excitation "quality", the excitation light spectral distribution should be weighted against the Pr^{3+} intermediate state absorption spectrum. In this respect, indoor lighting that emits more predominantly in the blue region will yield greater antimicrobial capability by the overall system.

In the proposed application of UC for enhancing SODIS, the intended excitation source is direct sunlight, which offers a significantly more intense source than indoor lights. Intensity may vary drastically depending on the time of day, latitude, and weather conditions. Sunlight comprises considerable power density in the blue range, as seen in Figure 44.

The quantum yield achieved by the phosphor layer is also of utmost importance when estimating the capabilities of a UC-AMS. The parameter is defined as the ratio of emitted upconverted photons (from $4f5d \rightarrow {}^3H_J, {}^3F_J$ transitions, in this case) to absorbed excitation photons – thus, reflectance and absorption losses are not expressed in this efficiency parameter. However, non-radiative vibronic energy losses, Stokes emission

Table 7. Parameters affecting the performance of upconversion antimicrobial surfaces.

Environmental Factors	Phosphor Performance Properties	Microbial Response Factors
Ambient light intensity	Surface texture/reflectivity	UVC dose requirements
Lighting cycle duration	Absorbance magnitude	UV action spectrum
Spectral distribution	Absorbance spectral distribution	Photo-repair mechanisms
Light angle/diffusivity	UC quantum yield	
Presence of foulants	Emission spectral distribution	
Rate of microbial deposition	Active layer thickness	

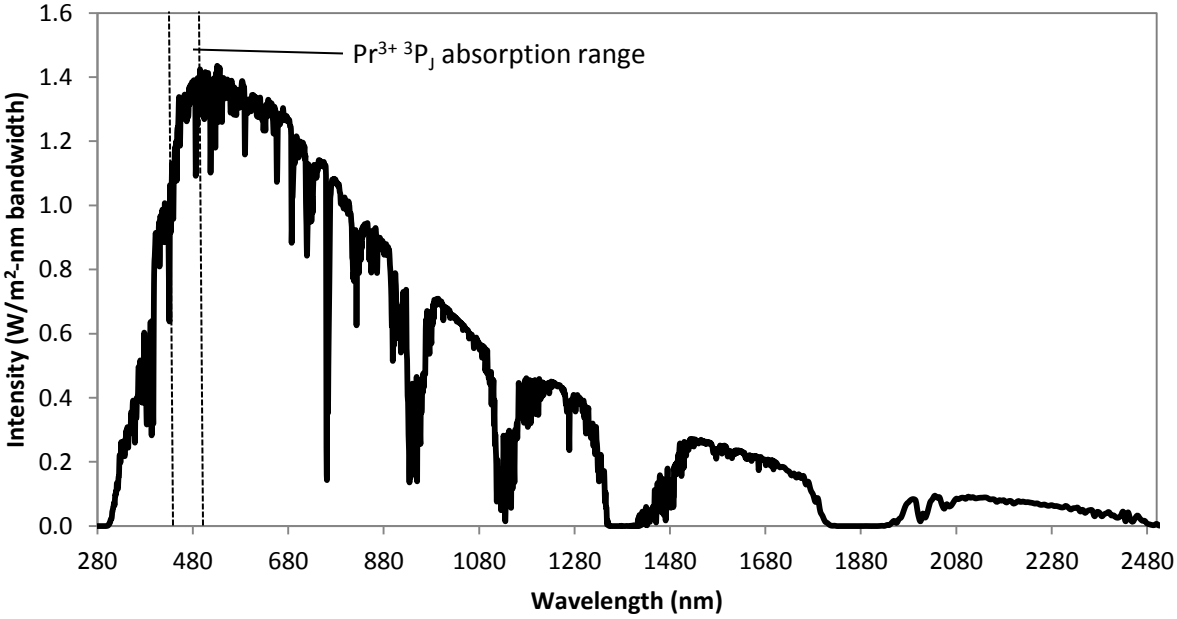

Figure 44. Solar radiation intensity at the Earth's surface (AM-1.5). www.ngdc.noaa.gov

from the intermediate state, and cascade emission from upper excited states will contribute to low values. Since emitted intensity shows quadratic dependence on excitation intensity in UC materials, the quantum yield is also excitation dependent, though the dependency is difficult to extrapolate to the low power regime [106].

8.2. Methods

8.2.1. Model Development

Equation 3 shows the simple mechanistic model developed for the present analysis. To predict the time required for 1-log (90%) inactivation of a target microorganism on a Pr^{3+}-activated phosphor surface, the model was designed to be calibrated using the biodosimetry results in Chapter 4 and to function without having known values of quantum yield, absolute material absorbance, or reflectance; instead, these parameters were grouped into a single variable termed "Pr^{3+} efficiency" (η), defined as the fraction of "useable" excitation power density that is absorbed by the activator ions and converted to UV radiation, accounting for reflection and scattering losses. Useable excitation power density is defined as the intensity of excitation light at wavelength λ ($I_{E,\lambda}$), corrected for the relative absorbance of the Pr^{3+} ^3P_J intermediate states at λ ($A_{Pr,\lambda}$), then integrated throughout the entire intermediate absorption range of λ = 430-495 nm.

$$t_{90} = \frac{2D}{60^2 X_{254} \eta \int_{\lambda=430}^{\lambda=495} I_{RE,\lambda} M [1-\left(10^{-A_{Pr,\lambda}}\right)] d\lambda} \qquad \text{Eq. 3}$$

t_{90} *= 90% inactivation time (h)*
2 *=(Discount the half of emitted light that is in the wrong direction)*
1/60^2 *= (Conversion of seconds to hours)*
X_{254} *= 254-Equivalence factor (dimensionless)*
η *= Pr^{3+} efficiency (dimensionless)*
$I_{RE,\lambda}$ *= Relative excitation intensity at wavelength=λ (arbitrary units, a.u.)*
M *= Intensity conversion factor (W·m^{-2}·[nm bandwidth]$^{-1}$·a.u.$^{-1}$)*
$A_{Pr,\lambda}$ *= Normalized Pr^{3+} absorbance at wavelength λ (-log·cm^{-1})*
λ *= Wavelength (nm)*
D *= Required UV-254 dose for 90% inactivation (W·s·m^{-2})*

For ambient light conditions, the relative emission spectrum ($I_{RE,\lambda}$) of "cool white" fluorescent bulbs measured in Chapter 4 was employed. This data, shown in Figure 45, may be considered an example of indoor lighting spectral distribution though, as mentioned previously, different bulbs will have differing spectra, and also sunlight from windows may be an important factor. Since the y-axis units are arbitrary, the model utilizes a conversion factor (M) to convert the arbitrary units into absolute intensity units of W·m^{-2}[nm-bandwidth]$^{-1}$. This factor can be adjusted to yield a desired integrated total intensity or total blue light intensity to simulate certain conditions. To account for the variation in Pr^{3+} absorbance over the blue/violet excitation range, the absorption spectrum of a $Pr(NO_3)_3$ solution was measured with a UV/VIS spectrometer and is shown in Figure 46. Because of the shielding effect of the 5s/5p electrons on the 4f suborbital, this spectrum will be qualitatively similar to the Pr^{3+} intra-4f absorption spectrum in any host medium – for example, the Y_2SiO_5;Pr^{3+} absorption spectrum recorded by Hu et al.[172] in Figure 14. This absorption spectrum was normalized such that the maximum absorbance at 445 nm was set to 100% absorption. Thus, the variable $A_{Pr,\lambda}$ in Eq. 3 reduces the excitation intensity in proportion to the Pr^{3+} absorption spectrum to generate "useable" excitation intensity. Then, the fraction of this light that is actually absorbed is accounted

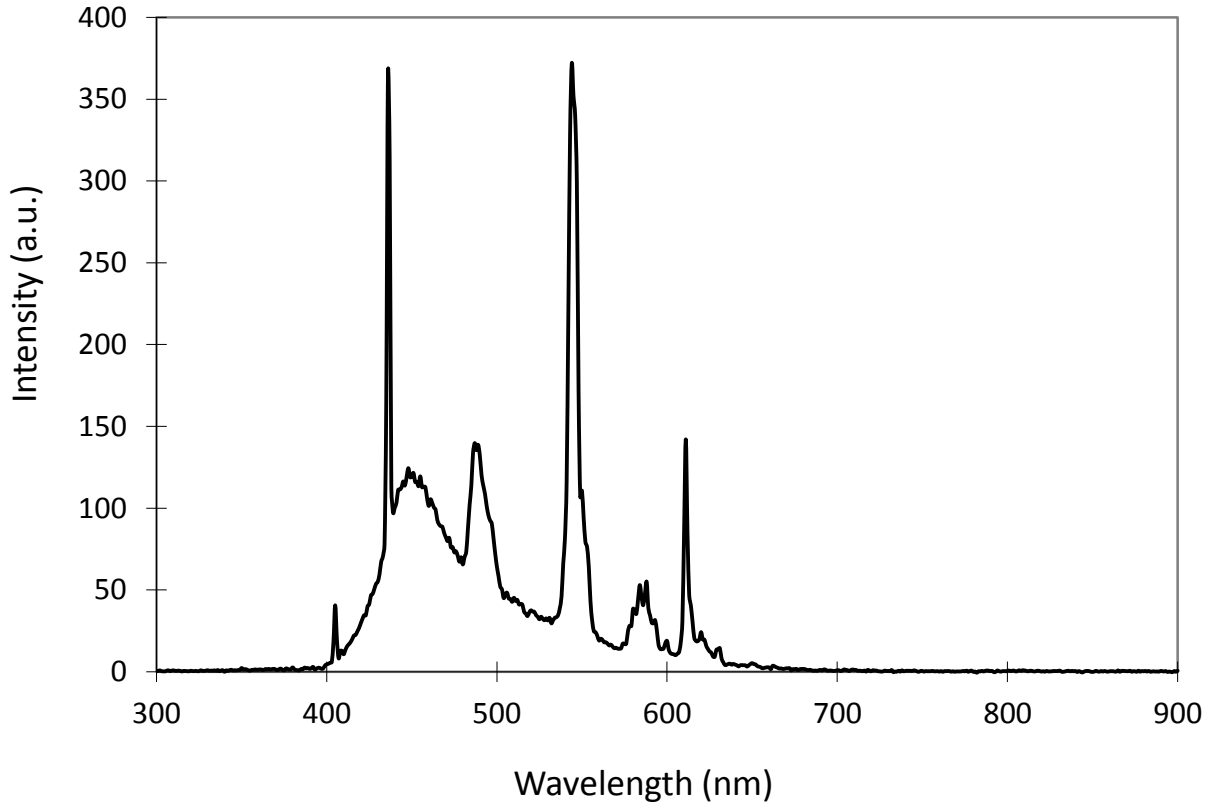

Figure 45. Emission profile of "cool white" tri-phosphor fluorescent bulbs after passage through a UV filter, as employed in antimicrobial experiments.

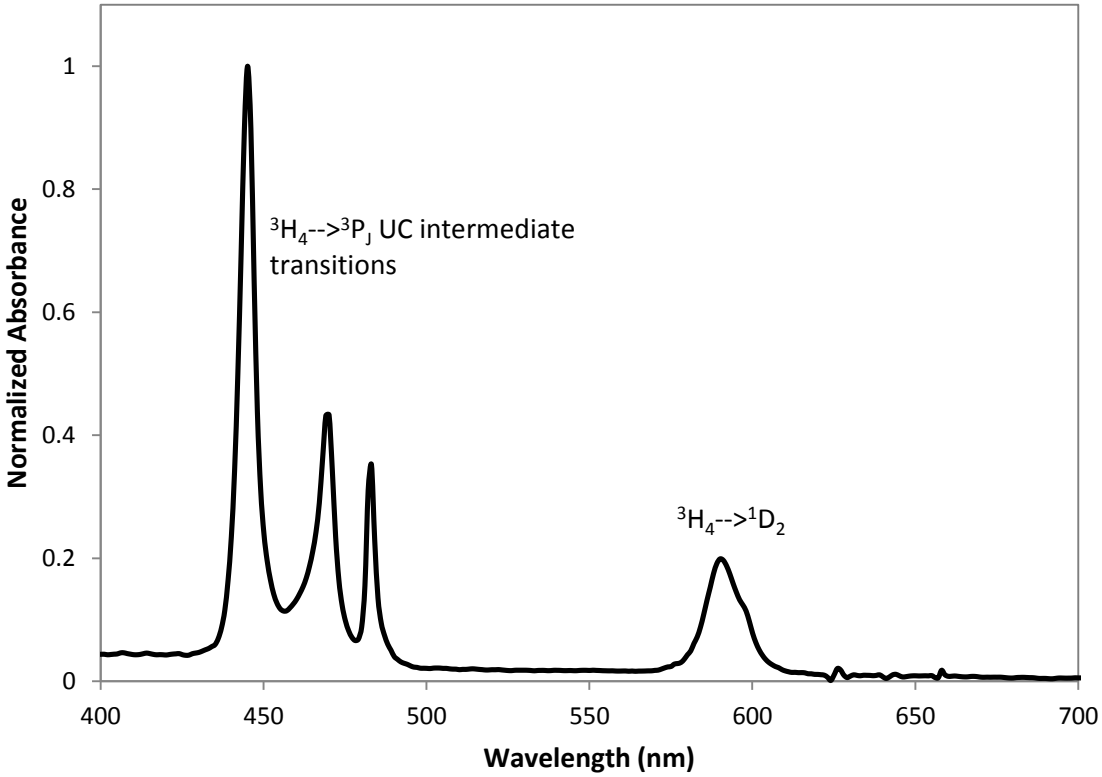

Figure 46. Visible-range normalized ground state absorption spectrum of aqueous $Pr(NO_3)_3$ solution.

for by η. In this fashion, any excitation source spectrum can be employed and the model will estimate the efficiency at which the light will be used.

Multiplication of the integrated useable excitation intensity by η yields the intensity of upconverted radiation emitted by the material. To predict microbial inactivation based on 90% reduction dose requirement (D), the relative antimicrobial efficacy of the emission must be determined. Since UVC inactivation experiments are typically conducted using mercury lamps that emit at 254 nm, all the inactivation dose requirements for various microbes in the literature are technically only applicable when using monochromatic radiation at this wavelength. The radiation emitted by a Pr^{3+} UC-AMS, on the other hand, consists of a variable spectrum across a wide range of UV wavelengths. Thus, to utilize the inactivation doses from the literature in the present model, the emitted intensity at each wavelength should be transformed into an intensity of 254 nm radiation that would result in the same inactivation rate. Such a procedure is somewhat impractical to include in the present analysis, as it requires a detailed UVC action spectrum for the organism in question. Therefore, an equivalence factor (X_{254}) was estimated from measured UC emission spectra of phosphors by considering the fraction of total emission in the UVC range, and the emission maximum wavelength relative to 254 nm and the ideal inactivation wavelength of ~265 nm. Values employed were 0.25 for X2-$Y_2SiO_5:Pr^{3+}$ and 0.60 for $Lu_xO_{x-1}F_{x+2}:Pr^{3+}$.

8.2.2. Pr^{3+} Efficiency Calibration and Model Use

To calibrate the model, data from the biodosimetry experiment in Chapter 4 was inputted, and the equation was solved to yield $\eta = 2.275\times10^{-4}$, when I_E(430-495 nm) = 20 W/m^2 (the condition used in the experiments). To estimate the η under ambient blue light intensity of 0.5 W/m^2 (measured with a radiometer under laboratory light conditions), the above efficiency value was multiplied by 0.1 as a high estimate and 0.001 as a low estimate, based on data from Fischer et al. regarding efficiency change of an Er^{3+} system under different excitation intensities [106]. For sunlight intensity (90 W/cm^2), multiplying factors of 5 (low) and 10 (high) were used. The model was run using the dose-response of *E. coli*, as this organism has a more representative UVC susceptibility (D = 30 W·s/m^2) than *B. subtilis* spores (D = 116 W·s/m^2) [50].

After estimating the *E. coli* t_{90} for the dip-coated $Y_2SiO_5:Pr^{3+},Li^+$ surface under ambient and sunlight conditions, other materials were considered. To predict t_{90} for microcrystalline $Y_2SiO_5:Pr^{3+},Li^+$, the data from Chapter 5 was used, which showed a 45% improvement in efficiency upon increasing the crystallite size into the micron range; thus η was simply increased by 45% to model this material. Previous experiments also showed that a ceramic X2-$Y_2SiO_5:Pr^{3+}$ pellet has approximately twice the efficiency of the powder form (data not shown), so η was again doubled. For the oxyfluoride phosphors, the change in emission spectrum must be considered, in addition to greater efficiency, so X_{254} was adjusted. Finally, a hypothetical high-efficiency UC-AMS was considered, which had an efficiency 500-times greater than $Lu_xO_{x-1}F_{x+2}:Pr^{3+}$. The 500-fold enhancement was chosen to apply optimistic, yet realistic, improvements of 10-fold resulting from a host with minimum phonon energy, 10-fold due to activator dispersal by

beneficial codoping, and 5-fold from reduced reflectance/thick active layer resulting from ceramic materials with larger crystallites.

8.3. Results and Discussion

Table 8 shows the inactivation times for several materials under different conditions as predicted by Eq. 3. Most notable are the differences in inactivation times between ambient light and sunlight conditions. Due to the excitation intensity dependence of UC quantum efficiency, not only is the solar radiation 180 times more intense, but it is estimated that the fraction of that light converted to UV is between 50 and 1000 times greater than the fraction of ambient light converted. These data reveal the importance of available excitation light intensity in applying UC-AMS to real-world use. For sunlight scenarios, the inactivation times appear well within the range for practical applicability to SODIS, wherein according to the high efficiency estimates, complete inactivation might occur in a matter of minutes. Even for the lowest efficiency in sunlight, the predicted 2 h t_{90} for *E. coli* reflects only the microbial kill attributed to UVC and would act in addition to established inactivation by UVA, UVB, and violet light [245-248]. Thus, the UC material might help to significantly reduce the required ~6 h exposure time for SODIS. In ambient light conditions, these data suggest that overall room light

Table 8. Predicted exposure time required for 90% inactivation of *E. coli* on various UC-AMS's under blue light intensities equivalent to ambient light (0.5 W/m^2) and AM-1.5 sunlight (90 W/m^2). Times calculated using both low and high UC efficiency estimates are shown.

	Predicted E. coli t_{90} (hours)			
	Ambient		*Sunlight*	
Material	**Low Efficiency**	**High Efficiency**	**Low Efficiency**	**High Efficiency**
$Y_2SiO_5:Pr^{3+},Li^+$ Dip Coated	193000	19300	2.0	1.0
$Y_2SiO_5:Pr^{3+},Li^+$ Powder	66400	6640	0.7	0.4
$Y_2SiO_5:Pr^{3+}$ Ceramic	33200	3320	0.4	0.2
$Lu_xO_{x-1}F_{x+2}:Pr^{3+}$	2940	294	0.03	0.02
Optimum System	6	0.6	0.00006	0.00003

intensity, specific placement of the material, and lighting spectrum may significantly influence microbial inactivation capability. Design and implementation of room lights that are optimized to offer both acceptable aesthetic light and substantial overlap with the Pr^{3+} UC excitation spectrum is a course of action that would warrant consideration.

While the above model demonstrates interesting relationships between material/environmental considerations and UC antimicrobial efficacy, the potentially large degree of error associated with the specific values in Table 8 cannot be ignored. The most critical limitation of the model is the fact that it was calibrated using data from one experiment – the biodosimetry involving *B. subtilis* spores described in Chapter 4. The UVC dose therein was calculated using an IT curve that was obtained under much greater UVC intensity (Figure 22), and the validity of extrapolating this dose response to lower UVC intensities is unknown. Additionally, translation of the response of *B. subtilis* spores to that of *E. coli* by simply using the ratio of their respective t_{90} values from water disinfection experiments in the literature is an equally invalid procedure. Finally, material parameters from other phosphors from the literature were used to estimate the UC efficiency of the Pr^{3+} phosphors, including absorption coefficient, reflectance, and quantum yield; actual values could differ significantly. At most, the results in Table 8 show that at present time, UC antimicrobial technology deserves additional research as it could potentially be a powerful and sustainable tool in combating pathogens.

The above analysis also did not incorporate absorption of additional photons with wavelengths outside of the ground→intermediate absorption range via ^3P_J→4f5d ESA. This phenomenon was shown to occur in Chapter 6, and it is believed that a range of green wavelengths can contribute to additional UVC emission. Yet, the model was

calibrated using the biodosimetry results from Chapter 4, which also did not consider this effect even though some green light was present from the fluorescent lamp employed; this additional UC emission was thus already accounted for in the calculated UC efficiency. In comparing Figure 44 with Figure 45, however, it is seen that green light makes up a much larger fraction of sunlight, than it does of the fluorescent lamp emission. Therefore, a more complete efficiency prediction model should predict a slightly higher UC efficiency for sunlight excitation than the model employed herein.

CHAPTER 9

SUMMARY, OUTLOOK, AND FUTURE WORK

9.1. Summary of Results

The research described herein has produced a substantial new body of knowledge regarding visible-to-UVC upconversion materials and the concept of UC-AMS. This work was specifically conducted to achieve a new type of antimicrobial technology for preventing microbial disease transfer via fomite contact, though much of the results are likely to benefit the broader field of applied UC materials, particularly with respect to applications involving low power excitation.

It was demonstrated that $Y_2SiO_5:Pr^{3+}$ phosphors can convert visible light into germicidal UVC photons at efficiencies sufficient to cause significant radiation damage to bacteria and spores. Clearly observable biofilm inhibition was observed by coated surfaces placed in aquatic bacterial suspension and exposed to a commercial fluorescent light bulb. The biocidal action resulting from frequency-amplified radiation was able to induce a through-space effect, inactivating and inhibiting bacteria through several micrometers of biofilm substance. Death of bacterial spores was also confirmed on dry $Y_2SiO_5:Pr^{3+}(Gd^{3+})(Li^{+})$ polycrystalline surfaces, though the UC-induced inactivation rate was slow under the excitation conditions employed. *Bacillus subtilis* spores, however,

show considerably lower UVC susceptibility than typical pathogenic bacteria and viruses. Yet the consistent UV dose-response of the spores allowed fitting of a regression curve correlating inactivation to known doses of UVC. This model was used to calculate the dose experienced by spores during UC-AMS experiments and allowed estimation of optical conversion efficiency by $Y_2SiO_5:Pr^{3+}(Gd^{3+})Li^+$ nanocrystalline surfaces on the order of 0.001%.

Results of crystallographic and spectroscopic study of $Y_2SiO_5:Pr^{3+},Li^+$ elucidated materials engineering strategies for maximizing UC efficiency in Pr^{3+} systems. The immediate goal of these experiments was to explain the mechanisms by which UC efficiency was increased upon addition of a Li^+ codopant. It was found that UC was enhanced by formation of larger crystallites, phase change to a preferred host polymorph, and increased inter-ion separation of Pr^{3+} activators. The last mechanism is of particular interest as it reveals a new strategy for maximizing Pr^{3+} UC in virtually any host material. In the case of Li^+-codoped $Y_2SiO_5:Pr^{3+}$, aliovalent substitution of Y^{3+} with smaller Li^+ ions was theorized to result in slight modification of the positions of atoms surrounding Pr^{3+}; this was believed to allow Pr^{3+} to occupy Y^{3+} sites while causing less local distortion of the crystal structure, which is the driving force for detrimental Pr^{3+} clustering. Expanding this technique to a more general strategy for enhancing Pr^{3+} UC thus entails introducing codopant ions that: (1) have lower oxidation state than the host cation; (2) are of smaller ionic radius than the host cation; (3) are optically inactive; and (4) do not possess any chemical qualities that otherwise degrade the phosphor or interfere with its synthesis.

The final set of experiments conducted using $Y_2SiO_5:Pr^{3+},Li^+$ revealed that this UC system – and likely many other systems – is capable of utilizing several different excitation wavelength ranges when irradiated with broad band light. This is due to the fact that the photon energy required for intermediate→upper excited state transitions is lower than that required for ground→intermediate transitions. The material can thus absorb and utilize these lower energy photons to some extent, though it will not be apparent in a UC excitation spectrum measured by scanning monochromatic wavelengths. Results showed that when excited by polychromatic light containing wavelengths within the $^3H_4 \rightarrow {}^3P_J$ absorption range, additional absorption of green light may occur and contribute to upconverted UVC emission. The same effect was observed, though to a much lesser extent, with yellow wavelengths. Such an ability to convert a wider-than-expected portion of the excitation bandwidth is relevant to application of UC materials involving sunlight or ambient light activation and should be taken into consideration by efficiency analyses.

While the $Y_2SiO_5:Pr^{3+}$ system was refined and optimized extensively, the underlying Y_2SiO_5 host was used due to existing reports in the literature [172, 173] and is not a material that is specifically suitable for Pr^{3+} UC. Thus, development of a more efficient visible-to-UVC upconversion phosphor using a bottom-up approach was conducted. The lutetium oxyfluoride system was selected after speculation that this host would yield desirable Pr^{3+} 4f5d band energy while having much lower maximum phonon energy than Y_2SiO_5. Material development efforts involving $Lu_xO_{x-1}F_{x+2}$ resulted in a new UC phosphor showing 4.5 times greater visible-to-UVC conversion efficiency than the previous optimized silicate system. The experiments also showed, however, that

additional work is needed to improve synthetic control over phase purity and activator distribution.

To further solidify UC-AMS technology as a viable option for deterring pathogens in the future, a simple model was developed for predicting antimicrobial efficacy of existing and hypothetical UC materials in advance of additional conclusive research. Simulation results showed that predicted inactivation time was highly sensitive to excitation light intensity and UC efficiency. For low intensity ambient room lighting scenarios, it was found that considerable advances in UC material performance may be required before practical inactivation rates can be expected. For sunlight excitation, however, predicted *E. coli* inactivation time was on the order of only 10^1 min, suggesting that application of visible-to-UVC upconversion to SODIS enhancement may be more achievable at present time than previously thought. However, the methods for making these predictions are subject to an unknown, and likely high, degree of error, and thus the results serve mainly as guidance for future research.

9.2. Outlook

Considering the progress that was made in a less-than-5 year time span since origination of the UC-AMS concept, the outlook for eventually realizing effective and sustainable UC-based technology for preventing disease remains very promising. From the first X1-Y_2SiO_5:Pr^{3+} phosphor material synthesized to the recent development of oxyfluoride ceramics, an approximate 80-fold improvement in UC efficiency has been realized. Furthermore, discovery of the suitability of oxyfluoride host crystals for Pr^{3+}

upconversion opens up a whole class of materials for exploration and phosphor development. Host structure design considerations elucidated in the Li^+ codoping studies are also likely to accelerate these efforts through targeted material engineering.

Aside from achieving additional UC efficiency gains, new methods of assessing antimicrobial efficacy of prepared surfaces also deserves further research. While spore inactivation assays were successfully conducted using the polycrystalline surfaces coated on silica glass via dip-coating, testing of ceramic materials brought difficulties. The ceramic pellet surfaces were water-penetrable due to micro-cracks and channels, which made inoculation with controlled quantities of microorganisms impossible to achieve by pipetting. New, more flexible, procedures for assaying surface-inoculated spores, as well as bacterial cells, are thus needed. It is desirable for the organisms to be in direct contact with the surface or raised less than a few μm using a UVC-transparent barrier; additional separation will result in a lower UVC exposure intensity, providing an underestimate of biocidal action during real implementation. This effect was observed during microbial experiments wherein inoculated fused silica cover slips were placed on top of dip-coated surfaces (data not shown).

The results in Chapter 8 suggest that emitted UVC by UC-AMS's may be substantially more intense under excitation by sunlight, making testing for SODIS applications justifiable. An efficient visible-to-UVC converting layer added to a clear water vessel may reduce the time required to generate potable water under sunlight exposure to more socially accepted durations. Pursuit of UC-incorporating SODIS technology could thus lead to significant quality-of-life improvements for people living without access to safe water. However, the increased average distance between

microbes and the UC surface in a water vessel of typical volume implies much lower exposure intensity.

9.3. Future Work

Continued development of oxyfluoride phosphors with superior performance is a priority for future research efforts. A material capable of 100 times greater visible-to-UVC conversion efficiency would almost certainly make UC-AMS an effective and highly practical technology with considerable advantages over existing antimicrobial concepts. Achieving this steep gain in efficiency is feasible if pursued through multiple converging materials engineering goals. Objectives for near-future phosphor development include:

- Identification of all $Lu_xO_{x-1}F_{x+2}$ Vernier phases that compete with the desired structure via XRD
- Develop strategies for achieving higher phase purity
- Image the various phase regions on phosphor pellets using SEM
- Measure host crystal phonon cutoff frequency using IR spectroscopy
- Compare Pr^{3+}-doped $Lu_xO_{x-1}F_{x+2}$ to undoped crystals to show the effect that the activator ions have on crystal chemistry
- Optimize precise Pr^{3+} concentration for maximum UC and test codopants for positive effects, monitored using PLS
- Test the effect of rapid thermal quenching from annealing temperature

More long-term objectives include expansion of oxyfluoride materials research to encompass other subclasses such as calcium-aluminum oxyfluorides. In addition to the possibility of better UC performance, such hosts have the added benefit of being RE-free, thus lowering material cost. Deviation from the Ln^{3+} UC paradigm is another option for pursuing more drastic gains in UC efficiency. Several inherent limitations of Ln^{3+} materials were discussed previous sections, and new mechanisms of inorganic UC may be awaiting discovery.

Aside from phosphor development, other aspects of UC-AMS technology requiring additional future research include:

- Development of microbial assays applicable to testing a wider range of surface types
- Assessment of inactivation kinetics for other microorganisms, such as *E. coli*, influenza, and norovirus
- Biodosimetric analysis of UC efficiency under simulated solar radiation
- Study of microbial UVC dose-response under known exposure intensities comparable to expected emission from UC surfaces

APPENDIX A

Photoluminescence Spectroscopy Instrument Components

COMPONENT	MAKE/MODEL	SPECIFICATIONS

Lasers

Argon Ion Laser	Modulaser Inc./Stellar Pro-ML 1000	Maximum Power (multiline): 1000 mW Maximum Power (488 nm): 140 mW Beam Diameter ($1/e^2$): 0.75 mm Beam Divergence: 0.95 mrad
Violet 447 nm DPSS Laser	OEM Lasers / BL-447-00100-CWM-SD-05-LED-0	Maximum Power (447±5 nm): 100 mW Beam Diameter: 5 mm Beam Divergence: 1.5 mrad
Yellow 589 nm DPSS Laser (Consumer grade high-power laser pointer)	LaserTo Inc. / 100 mW Wraith Series	Maximum Power (589 nm): 100 mW Battery power replaced with external power supply (3.8 V)

Excitation Filters

488 nm Line Filter	Newport/10LF10-488	Transmission Range: 486-490 nm
600 nm Short Pass Filter	Thorlabs/FES0600	

Dichroic Beam Combiner (1)	Newport/DCM11	Transmission Range: 473-641 nm Reflection Range: 439-458 nm
Dichroic Beam Combiner (2)	Thorlabs/DMLP567	Transmission Range: 584-700 nm Reflection Range: 380-550 nm

Beam Directing Optics

Concave Mirror	Newport/05DC200ER.1	Focal Length: 100 mm
Mirror Mounts	Newport/U50-A	
Plano-Convex Lens	Edmund Optics/48-664	Focal Length: 200 mm

Emission Collection Optics

UV-Antireflective Plano-convex Lens	Edmund Optics/48030	Focal Length: 30 mm

Rejection Filters

400 nm Shortpass	Edmund Optics/49816	
450 nm Longpass	Thorlabs/FEL0450	
475 nm Longpass	Edmund Optics/64617	
600 nm Longpass	Thorlabs/FEL0600	

Detection System		
Monochromator	Newport Oriel/Cornerstone 260 1/4M	Dual Grating RS-232 Communication
Monochromator Grating	Newport Oriel /SP74161-4976	MgF2 Overcoat for high UV throughput Lines/mm: 2400 Blaze: 250 nm
Photomultiplier Tube	Newport Oriel/77348	Wavelength Range: 160-900 nm Maximum Voltage: 1000 V
PMT Housing	Newport Oriel/70107	Side-on configuration
PMT Power Supply	Newport Oriel/70705	
Current Preamplifier	Newport Oriel/70710	Amplification (V/A): 10^6 - 10^9
Digital Lock-in Amplifier	Newport Oriel/70100 Merlin Radiometer	Single Channel RS-232 Communication
Chopper Head	Newport Oriel/75154	
Chopper Wheel	Newport Oriel/75162	2-Aperture Maximum Chop: 160 Hz
Data Acquisition Software	Newport Oriel/TRACQ Basic	

APPENDIX B

Refined Crystallographic Parameters

Selected Rietveld analysis results are shown below for future reference.

X1-Y_2SiO_5:Pr(1.2%)

Space Group: $P2_1/c$

a = 9.037680 b = 6.936106 c = 6.653618

α = 90.0000 β = 106.6493 γ = 90.0000

	Fraction	x	y	z
Y+3	1	0.119935	0.141839	0.4299
Y+3	1	0.524401	0.624284	0.2302
SI+4	1	0.197358	0.590212	0.4683
O-2	1	0.20713	0.413361	0.6544
O-2	1	0.121468	0.464025	0.2452
O-2	1	0.376038	0.617656	0.4935
O-2	1	0.120429	0.76364	0.4644
O-2	1	0.394036	0.393883	0.0955

X2-Y_2SiO_5

Space Group: I2/a

a = 10.426293 b = 6.729462 c = 12.494602

α = 90.0000 β = 102.7622 γ = 90.0000

	Fraction	x	y	z
Y+3	1	0.307281	0.376551	0.141920
Y+3	1	0.427423	-0.255115	-0.037354
SI+4	1	-0.093490	0.181058	0.691
O-2	1	0.303332	-0.281980	0.119292
O-2	1	0.451294	-0.011917	0.093242
O-2	1	0.470046	-0.147268	0.299837
O-2	1	0.263064	0.069450	0.198897
O-2	1	0.377692	0.395942	-0.024108

REFERENCES

1. Harris, S. R.; Feil, E. J.; Holden, M. T. G.; Quail, M. A.; Nickerson, E. K.; Chantratita, N.; Gardete, S.; Tavares, A.; Day, N.; Lindsay, J. A.; Edgeworth, J. D.; de Lencastre, H.; Parkhill, J.; Peacock, S. J.; Bentley, S. D., Evolution of MRSA During Hospital Transmission and Intercontinental Spread. *Science* **2010,** *327*, (5964), 469-474.

2. Eisler, P., Deadly 'superbugs' invade U.S. health care facilities. *USA Today* 2012.

3. Pollack, A., Rising threat of infections unfazed by antibiotics. *New York Times* 2010.

4. CDC, Foodborne Diseases Active Surveillance Network (FoodNet): FoodNet Surveillance Report for 2010 (Final Report). *Atlanta, Georgia: U.S. Department of Health and Human Services, CDC.* **2011**.

5. CDC, No Progress in Salmonella During Past 15 Years. *Press Release, Centers for Disease Control and Prevention, Atlanta, GA.* **2011**.

6. WHO *Facts and Figures on Water Quality and Health* The World Health Organization: Water Sanitation and Health, 2013.

7. Page, K.; Wilson, M.; Parkin, I. P., Antimicrobial surfaces and their potential in reducing the role of the inanimate environment in the incidence of hospital-acquired infections. *Journal of Materials Chemistry* **2009,** *19*, (23), 3819-3831.

8. Appendini, P.; Hotchkiss, J. H., Review of antimicrobial food packaging. *Innovative Food Science & Emerging Technologies* **2002,** *3*, (2), 113-126.

9. Quintavalla, S.; Vicini, L., Antimicrobial food packaging in meat industry. *Meat Science* **2002,** *62*, (3), 373-380.

10. Tiller, J., Antimicrobial Surfaces. In *Bioactive Surfaces*, Börner, H. G.; Lutz, J.-F., Eds. Springer Berlin Heidelberg: 2011; Vol. 240, pp 193-217.

11. Berney, M.; Weilenmann, H. U.; Simonetti, A.; Egli, T., Efficacy of solar disinfection of Escherichia coli, Shigella flexneri, Salmonella Typhimurium and Vibrio cholerae. *Journal of Applied Microbiology* **2006,** *101*, (4), 828-836.

12. Fisher, M. B.; Iriarte, M.; Nelson, K. L., Solar water disinfection (SODIS) of Escherichia coli, Enterococcus spp., and MS2 coliphage: effects of additives and alternative container materials. *Water Research* **2012,** *46*, (6), 1745-1754.

13. Acevedo, A.; Carpio, E. A.; Rodriguez, J.; Manzano, M. A., Disinfection of Natural Water by Solar Photocatalysis Using Immobilized TiO[sub 2] Devices: Efficiency in Eliminating Indicator Bacteria and Operating Life of the System. *Journal of Solar Energy Engineering* **2012,** *134*, (1), 011008-10.

14. Gelover, S.; Gómez, L. A.; Reyes, K.; Teresa Leal, M., A practical demonstration of water disinfection using TiO_2 films and sunlight. *Water Research* **2006,** *40*, (17), 3274-3280.

15. Malato, S.; Blanco, J.; Vidal, A.; Richter, C., Photocatalysis with solar energy at a pilot-plant scale: an overview. *Applied Catalysis B: Environmental* **2002,** *37*, (1), 1-15.

16. Shalev, T.; Gopin, A.; Bauer, M.; Stark, R. W.; Rahimipour, S., Non-leaching antimicrobial surfaces through polydopamine bio-inspired coating of quaternary ammonium salts or an ultrashort antimicrobial lipopeptide. *Journal of Materials Chemistry* **2012,** *22*, (5), 2026-2032.

17. Ragaseema, V. M.; Unnikrishnan, S.; Kalliyana Krishnan, V.; Krishnan, L. K., The antithrombotic and antimicrobial properties of PEG-protected silver nanoparticle coated surfaces. *Biomaterials* **2012,** *33*, (11), 3083-3092.

18. Mansouri, M. D.; Opperman, T. J.; Williams, J. D.; Stager, C.; Darouiche, R. O., In Vitro Potency and In Vivo Efficacy of a Novel Bis-Indole Antimicrobial Compound in Reducing Catheter Colonization. *Antimicrobial Agents and Chemotherapy* **2012,** *56*, (4), 2201-2204.

19. Benn, T. M.; Westerhoff, P., Nanoparticle silver released into water from commercially available sock fabrics. *Environmental Science & Technology* **2008,** *42*, (11), 4133-4139.

20. Tribou, M.; Swain, G., The use of proactive in-water grooming to improve the performance of ship hull antifouling coatings. *Biofouling* **2009,** *26*, (1), 47-56.

21. Schultz, M. P.; Bendick, J. A.; Holm, E. R.; Hertel, W. M., Economic impact of biofouling on a naval surface ship. *Biofouling* **2010,** *27*, (1), 87-98.

22. Tiller, J. C.; Sprich, C.; Hartmann, L., Amphiphilic conetworks as regenerative controlled releasing antimicrobial coatings. *Journal of Controlled Release* **2005,** *103*, (2), 355-367.

23. Fuchs, A. D.; Tiller, J. C., Contact-Active Antimicrobial Coatings Derived from Aqueous Suspensions. *Angewandte Chemie International Edition* **2006,** *45*, (40), 6759-6762.

24. Kalyon, B. D.; Olgun, U., Antibacterial efficacy of triclosan-incorporated polymers. *American Journal of Infection Control* **2001,** *29*, (2), 124-125.

25. Kumar, A.; Vemula, P. K.; Ajayan, P. M.; John, G., Silver-nanoparticle-embedded antimicrobial paints based on vegetable oil. *Nat Mater* **2008,** *7*, (3), 236-241.

26. Pal, S.; Tak, Y. K.; Song, J. M., Does the Antibacterial Activity of Silver Nanoparticles Depend on the Shape of the Nanoparticle? A Study of the Gram-Negative Bacterium Escherichia coli. *Appl. Environ. Microbiol.* **2007,** *73*, (6), 1712-1720.

27. Stefan Loher, O. D. S., Tobias Maienfisch, Stefan Bokorny, Wendelin J. Stark,, Micro-organism-Triggered Release of Silver Nanoparticles from Biodegradable Oxide Carriers Allows Preparation of Self-Sterilizing Polymer Surfaces. *Small* **2008,** *4*, (6), 824-832.

28. Buth, J. M.; Steen, P. O.; Sueper, C.; Blumentritt, D.; Vikesland, P. J.; Arnold, W. A.; McNeill, K., Dioxin Photoproducts of Triclosan and Its Chlorinated Derivatives in Sediment Cores. *Environmental Science & Technology* **2010,** *44*, (12), 4545-4551.

29. Chinnapongse, S. L.; MacCuspie, R. I.; Hackley, V. A., Persistence of singly dispersed silver nanoparticles in natural freshwaters, synthetic seawater, and simulated estuarine waters. *Science of The Total Environment* **2011,** *409*, (12), 2443-2450.

30. Cushnie, T. P. T.; Robertson, P. K. J.; Officer, S.; Pollard, P. M.; Prabhu, R.; McCullagh, C.; Robertson, J. M. C., Photobactericidal effects of TiO_2 thin films at low temperatures—A preliminary study. *Journal of Photochemistry and Photobiology A: Chemistry* **2010,** *216*, (2–3), 290-294.

31. Makal, U.; Wood, L.; Ohman, D. E.; Wynne, K. J., Polyurethane biocidal polymeric surface modifiers. *Biomaterials* **2006,** *27*, (8), 1316-1326.

32. Murata, H.; Koepsel, R. R.; Matyjaszewski, K.; Russell, A. J., Permanent, non-leaching antibacterial surfaces--2: How high density cationic surfaces kill bacterial cells. *Biomaterials* **2007,** *28*, (32), 4870-4879.

33. EPA, U. S., EPA registers copper-containing alloy products. In Pesticides: Topical and Chemical Fact Sheets. U.S. Environmental Protection Agency, 2012.

34. Grass, G.; Rensing, C.; Solioz, M., Metallic Copper as an Antimicrobial Surface. *Applied and Environmental Microbiology* **2011,** *77*, (5), 1541-1547.

35. Karpanen, T. J. P.; Casey, A. L. P.; Lambert, P. A. D.; Cookson, B. D. F.; Nightingale, P. P.; Miruszenko, L. R.; Elliott, T. S. J. D., The Antimicrobial Efficacy of Copper Alloy Furnishing in the Clinical Environment: A Crossover Study. *Infection Control and Hospital Epidemiology* **2012,** *33*, (1), 3-9.

36. Santo, C. E.; Quaranta, D.; Grass, G., Antimicrobial metallic copper surfaces kill Staphylococcus haemolyticus via membrane damage. *MicrobiologyOpen* **2012,** *1*, (1), 46-52.

37. Rai, S. M. D.; Hirsch, B. E. M. D.; Attaway, H. H. M. S. M. B. A.; Nadan, R. R. N.; Fairey, S. B.; Hardy, J. B.; Miller, G. M.; Armellino, D. R. N.; Wilton R. Moran, B. S.; Sharpe, P. P.; Estelle, A. B. S.; Michel, J. H. M.; Michels, H. T. P.; Schmidt, M. G. P., Evaluation of the Antimicrobial Properties of Copper Surfaces in an Outpatient Infectious Disease Practice. *Infection Control and Hospital Epidemiology* **2012,** *33*, (2), 200-201.

38. Schmidt, M. G.; Attaway, H. H.; Sharpe, P. A.; John, J.; Sepkowitz, K. A.; Morgan, A.; Fairey, S. E.; Singh, S.; Steed, L. L.; Cantey, J. R.; Freeman, K. D.; Michels, H. T.; Salgado, C. D., Sustained Reduction of Microbial Burden on Common Hospital

Surfaces through Introduction of Copper. *Journal of Clinical Microbiology* **2012,** *50*, (7), 2217-2223.

39. Espírito Santo, C.; Morais, P. V.; Grass, G., Isolation and Characterization of Bacteria Resistant to Metallic Copper Surfaces. *Applied and Environmental Microbiology* **2010,** *76*, (5), 1341-1348.

40. Fu, G.; Vary, P. S.; Lin, C.-T., Anatase TiO_2 Nanocomposites for Antimicrobial Coatings. *The Journal of Physical Chemistry B* **2005,** *109*, (18), 8889-8898.

41. Kong, H.; Song, J.; Jang, J., Photocatalytic Antibacterial Capabilities of TiO2−Biocidal Polymer Nanocomposites Synthesized by a Surface-Initiated Photopolymerization. *Environmental Science & Technology* **2010,** *44*, (14), 5672-5676.

42. Perni, S.; Piccirillo, C.; Pratten, J.; Prokopovich, P.; Chrzanowski, W.; Parkin, I. P.; Wilson, M., The antimicrobial properties of light-activated polymers containing methylene blue and gold nanoparticles. *Biomaterials* **2009,** *30*, (1), 89-93.

43. Wilson, M., Light-activated antimicrobial coating for the continuous disinfection of surfaces. *Infection control and hospital epidemiology : the official journal of the Society of Hospital Epidemiologists of America* **2003,** *24*, (10), 782-784.

44. Snow, S. D.; Lee, J.; Kim, J.-H., Photochemical and Photophysical Properties of Sequentially Functionalized Fullerenes in the Aqueous Phase. *Environmental Science & Technology* **2012,** *46*, (24), 13227-13234.

45. Ogilby, P. R., Singlet oxygen: there is indeed something new under the sun. *Chemical Society Reviews* **2010,** *39*, (8), 3181-3209.

46. Schaefer, F. C.; Zimmermann, W. D., Self-oxidation of Methylene Blue. *Nature* **1968,** *220*, (5162), 66-67.

47. Lin, G.; Zheng, J.; Xu, R., Template-Free Synthesis of Uniform CdS Hollow Nanospheres and Their Photocatalytic Activities. *The Journal of Physical Chemistry C* **2008,** *112*, (19), 7363-7370.

48. Chen, R. Z.; Craik, S. A.; Bolton, J. R., Comparison of the action spectra and relative DNA absorbance spectra of microorganisms: Information important for the determination of germicidal fluence (UV dose) in an ultraviolet disinfection of water. *Water Research* **2009,** *43*, (20), 5087-5096.

49. Mamane, H.; Shemer, H.; Linden, K. G., Inactivation of E. coli, B. subtilis spores, and MS2, T4, and T7 phage using UV/H_2O_2 advanced oxidation. *Journal of Hazardous Materials* **2007,** *146*, (3), 479-486.

50. Schmelling, D.; Cotton, C.; Mackey, E., Ultraviolet disinfection guidance manual for the final long term 2 enhanced surface water treatment rule. In United States Environmental Protection Agency. EPA 815-R-06-007: Office of Water, Washington, D.C., 2006.

51. Oguma, K.; Katayama, H.; Mitani, H.; Morita, S.; Hirata, T.; Ohgaki, S., Determination of Pyrimidine Dimers in Escherichia coli and Cryptosporidium parvum during UV Light Inactivation, Photoreactivation, and Dark Repair. *Appl. Environ. Microbiol.* **2001,** *67*, (10), 4630-4637.

52. Auzel, F., Upconversion and Anti-Stokes Processes with f and d Ions in Solids. *Chem. Rev.* **2004,** *104*, (1), 139-174.

53. Wang, F.; Liu, X., Recent advances in the chemistry of lanthanide-doped upconversion nanocrystals. *Chemical Society Reviews* **2009,** *38*, (4), 976-989.

54. Ropp, R. C., *Luminescence and the Solid State*. Second ed.; Elsevier: Amsterdam, The Netherlands, 2004.

55. Henderson, B.; Imbusch, G. F., *Optical spectroscopy of inorganic solids*. Oxford: 1989; Vol. 44.

56. Buenzli, J.-C. G.; Piguet, C., Taking advantage of luminescent lanthanide ions. *Chemical Society Reviews* **2005,** *34*, (12), 1048-1077.

57. Wang, F.; Han, Y.; Lim, C. S.; Lu, Y.; Wang, J.; Xu, J.; Chen, H.; Zhang, C.; Hong, M.; Liu, X., Simultaneous phase and size control of upconversion nanocrystals through lanthanide doping. *Nature* **2010,** *463*, (7284), 1061-1065.

58. Zou, W.; Visser, C.; Maduro, J. A.; Pshenichnikov, M. S.; Hummelen, J. C., Broadband dye-sensitized upconversion of near-infrared light. *Nat Photon* **2012,** *6*, (8), 560-564.

59. Bloembergen, N., Solid State Infrared Quantum Counters. *Physical Review Letters* **1959,** *2*, (3), 84-85.

60. Auzel, F., Compteur quantique par transfert d'energie entre de Yb^{3+} a Tm^{3+} dans un tungstate mixte et dans verre germanate. *Compt. Rend. Acad. Sci. Paris B* **1966**.

61. Page, R. H.; Schaffers, K. I.; Waide, P. A.; Tassano, J. B.; Payne, S. A.; Krupke, W. F.; Bischel, W. K., Upconversion-pumped luminescence efficiency of rare-earth-doped hosts sensitized with trivalent ytterbium. *J. Opt. Soc. Am. B* **1998,** *15*, (3), 996-1008.

62. Mai, H.-X.; Zhang, Y.-W.; Sun, L.-D.; Yan, C.-H., Highly Efficient Multicolor Up-Conversion Emissions and Their Mechanisms of Monodisperse $NaYF_4$:Yb,Er Core

and Core/Shell-Structured Nanocrystals. *The Journal of Physical Chemistry C* **2007,** *111*, (37), 13721-13729.

63. Nyk, M.; Kumar, R.; Ohulchanskyy, T. Y.; Bergey, E. J.; Prasad, P. N., High Contrast in Vitro and in Vivo Photoluminescence Bioimaging Using Near Infrared to Near Infrared Up-Conversion in Tm^{3+} and Yb^{3+} Doped Fluoride Nanophosphors. *Nano Letters* **2008,** *8*, (11), 3834-3838.

64. Hilderbrand, S. A.; Shao, F.; Salthouse, C.; Mahmood, U.; Weissleder, R., Upconverting luminescent nanomaterials: application to in vivo bioimaging. *Chemical Communications* **2009**, (28), 4188-4190.

65. Kumar, R.; Nyk, M.; Ohulchanskyy, T. Y.; Flask, C. A.; Prasad, P. N., Combined Optical and MR Bioimaging Using Rare Earth Ion Doped $NaYF_4$ Nanocrystals. *Adv. Funct. Mater.* **2009,** *19*, (6), 853-859.

66. Idris, N. M.; Gnanasammandhan, M. K.; Zhang, J.; Ho, P. C.; Mahendran, R.; Zhang, Y., In vivo photodynamic therapy using upconversion nanoparticles as remote-controlled nanotransducers. *Nat Med* **2012,** *18*, (10), 1580-1585.

67. Wang, L.; Li, Y., Green upconversion nanocrystals for DNA detection. *Chemical Communications* **2006,** *0*, (24), 2557-2559.

68. Jeevan, M. M.; William, M. C.; May, P. S.; QuocAnh, L.; Grant, A. C.; Jon, J. K., Security printing of covert quick response codes using upconverting nanoparticle inks. *Nanotechnology* **2012,** *23*, (39), 395201.

69. Won Jin, K.; Marcin, N.; Paras, N. P., Color-coded multilayer photopatterned microstructures using lanthanide (III) ion co-doped $NaYF_4$ nanoparticles with

upconversion luminescence for possible applications in security. *Nanotechnology* **2009,** *20*, (18), 185301.

70. Schafer, H.; Ptacek, P.; Kompe, K.; Haase, M., Lanthanide-Doped $NaYF_4$ Nanocrystals in Aqueous Solution Displaying Strong Up-Conversion Emission. *Chem. Mater.* **2007,** *19*, (6), 1396-1400.

71. Joubert, M. F.; Guyot, Y.; Jacquier, B.; Chaminade, J. P.; Garcia, A., Fluoride crystals and high lying excited states of rare earth ions. *Journal of Fluorine Chemistry* **2001,** *107*, (2), 235-240.

72. Zhmurin, P. N.; Znamenskii, N. V.; Yukina, T. G.; Malyukin, Y. V., Strong quenching of $Y_2SiO_5:Pr^{3+}$ nanocrystal luminescence by praseodymium nonuniform distribution. *physica status solidi (b)* **2007,** *244*, (9), 3325-3332.

73. Wang, W.; Shang, Q.; Zheng, W.; Yu, H.; Feng, X.; Wang, Z.; Zhang, Y.; Li, G., A Novel Near-Infrared Antibacterial Material Depending on the Upconverting Property of Er^{3+}-Yb^{3+}-Fe^{3+} Tridoped TiO_2 Nanopowder. *The Journal of Physical Chemistry C* **2010,** *114*, (32), 13663-13669.

74. Zhang, Z. Z.; Zhang, J. H.; Zhou, W., Structure and Up-Conversion Luminescence Properties of Er^{3+}-Yb^{3+}Co-Doped TiO_2 Nanocrystals Prepared by Sol-Gel Method. *Advanced Materials Research* **2009,** *66*, 167-170.

75. Sun, Y.; Chen, Y.; Tian, L.; Yu, Y.; Kong, X.; Zhao, J.; Zhang, H., Controlled synthesis and morphology dependent upconversion luminescence of $NaYF_4$:Yb, Er nanocrystals. *Nanotechnology* **2007**, (27), 275609.

76. Liu, G.; Chen, X., Spectroscopic Properties of Lanthanides in Nanomaterials. In *Handbook on the Physics and Chemistry of Rare Earths, K.A. Gschneidner, J.*; *Bünzli, J.-C. G.*; *Pecharsky, V. K.*, Eds. Elsevier: 2007; Vol. 37, pp 100-169.

77. Khan, A.; Yadav, R.; Mukhopadhya, P.; Singh, S.; Dwivedi, C.; Dutta, V.; Chawla, S., Core–shell nanophosphor with enhanced NIR–visible upconversion as spectrum modifier for enhancement of solar cell efficiency. *Journal of Nanoparticle Research* **2011,** *13*, (12), 6837-6846.

78. Lu, Q.; Li, A.; Guo, F.; Sun, L.; Zhao, L., The two-photon excitation of SiO_2-coated Y_2O_3:Eu^{3+} nanoparticles by a near-infrared femtosecond laser. *Nanotechnology* **2008**, (20), 205704.

79. Qian, H.-S.; Zhang, Y., Synthesis of Hexagonal-Phase Core-Shell $NaYF_4$ Nanocrystals with Tunable Upconversion Fluorescence. *Langmuir* **2008,** *24*, (21), 12123-12125.

80. Islangulov, R. R.; Lott, J.; Weder, C.; Castellano, F. N., Noncoherent Low-Power Upconversion in Solid Polymer Films. *Journal of the American Chemical Society* **2007,** *129*, (42), 12652-12653.

81. Singh-Rachford, T. N.; Castellano, F. N., Photon upconversion based on sensitized triplet–triplet annihilation. *Coordination Chemistry Reviews* **2010,** *254*, (21–22), 2560-2573.

82. Islangulov, R. R.; Castellano, F. N., Photochemical Upconversion: Anthracene Dimerization Sensitized to Visible Light by a RuII Chromophore. *Angewandte Chemie* **2006,** *118*, (36), 6103-6105.

83. Singh-Rachford, T. N.; Islangulov, R. R.; Castellano, F. N., Photochemical Upconversion Approach to Broad-Band Visible Light Generation. *The Journal of Physical Chemistry A* **2008,** *112*, (17), 3906-3910.

84. Singh-Rachford, T. N.; Nayak, A.; Muro-Small, M. L.; Goeb, S.; Therien, M. J.; Castellano, F. N., Supermolecular-Chromophore-Sensitized Near-Infrared-to-Visible Photon Upconversion. *Journal of the American Chemical Society* **2010,** *132*, (40), 14203-14211.

85. Singh-Rachford, T. N.; Castellano, F. N., Triplet Sensitized Red-to-Blue Photon Upconversion. *J. Phys. Chem. Lett.* **2010,** *1*, (1), 195-200.

86. Yakutkin, V.; Aleshchenkov, S.; Chernov, S.; Miteva, T.; Nelles, G.; Cheprakov, A.; Baluschev, S., Towards the IR Limit of the Triplet-Triplet Annihilation-Supported Up-Conversion: Tetraanthraporphyrin. *Chem.-Eur. J.* **2008,** *14*, (32), 9846-9850.

87. Baluschev, S.; Yakutkin, V.; Miteva, T.; Avlasevich, Y.; Chernov, S.; Aleshchenkov, S.; Nelles, G.; Cheprakov, A.; Yasuda, A.; Mullen, K.; Wegner, G., Blue-green up-conversion: Noncoherent excitation by NIR light. *Angew. Chem.-Int. Edit.* **2007,** *46*, (40), 7693-7696.

88. Singh-Rachford, T. N.; Haefele, A.; Ziessel, R.; Castellano, F. N., Boron Dipyrromethene Chromophores: Next Generation Triplet Acceptors/Annihilators for Low Power Upconversion Schemes. *Journal of the American Chemical Society* **2008,** *130*, (48), 16164.

89. Singh-Rachford, T. N.; Castellano, F. N., Supra-Nanosecond Dynamics of a Red-to-Blue Photon Upconversion System. *Inorganic Chemistry* **2009,** *48*, (6), 2541-2548.

90. Monguzzi, A.; Tubino, R.; Meinardi, F., Multicomponent Polymeric Film for Red to Green Low Power Sensitized Up-Conversion. *J. Phys. Chem. A* **2009,** *113*, (7), 1171-1174.

91. Miteva, T.; Yakutkin, V.; Nelles, G.; Baluschev, S., Annihilation assisted upconversion: all-organic, flexible and transparent multicolour display. *New Journal of Physics* **2008,** *10*.

92. Turshatov, A.; Busko, D.; Baluschev, S.; Miteva, T.; Landfester, K., Micellar carrier for triplet-triplet annihilation-assisted photon energy upconversion in a water environment. *New Journal of Physics* **2011,** *13*.

93. Kim, J. H.; Deng, F.; Castellano, F. N., High Efficiency Low-Power Upconverting Soft Materials. *Chemistry of Materials* **2012,** *24*, (12), 2250-2252.

94. Merkel, P. B.; Dinnocenzo, J. P., Low-power green-to-blue and blue-to-UV upconversion in rigid polymer films. *Journal of Luminescence* **2009,** *129*, (3), 303-306.

95. Wohnhaas, C.; Turshatov, A.; Mailander, V.; Lorenz, S.; Baluschev, S.; Miteva, T.; Landfester, K., Annihilation Upconversion in Cells by Embedding the Dye System in Polymeric Nanocapsules. *Macromolecular Bioscience* **2011,** *11*, (6), 772-778.

96. Monguzzi, A.; Frigoli, M.; Larpent, C.; Tubino, R.; Meinardi, F., Low-Power-Photon Up-Conversion in Dual-Dye-Loaded Polymer Nanoparticles. *Adv. Funct. Mater.* **2012,** *22*, (1), 139-143.

97. Zhao, W.; Castellano, F. N., Upconverted emission from pyrene and di-tert-butylpyrene using Ir(ppy)(3) as triplet sensitizer. *J. Phys. Chem. A* **2006,** *110*, (40), 11440-11445.

98. Singh-Rachford, T. N.; Castellano, F. N., Low Power Visible-to-UV Upconversion. *J. Phys. Chem. A* **2009,** *113*, (20), 5912-5917.

99. Liu, Q.; Yang, T. S.; Feng, W.; Li, F. Y., Blue-Emissive Upconversion Nanoparticles for Low-Power-Excited Bioimaging in Vivo. *Journal of the American Chemical Society* **2012,** *134*, (11), 5390-5397.

100. Singh-Rachford, T. N.; Lott, J.; Weder, C.; Castellano, F. N., Influence of Temperature on Low-Power Upconversion in Rubbery Polymer Blends. *Journal of the American Chemical Society* **2009,** *131*, (33), 12007-12014.

101. Zhang, C.; Zheng, J. Y.; Zhao, Y. S.; Yao, J. N., Organic core-shell nanostructures: microemulsion synthesis and upconverted emission. *Chemical Communications* **2010,** *46*, (27), 4959-4961.

102. Qin, G.; Qin, W.; Wu, C.; Huang, S.; Zhao, D.; Zhang, J.; Lu, S., Intense ultraviolet upconversion luminescence from Yb^{3+} and Tm^{3+} codoped amorphous fluoride particles synthesized by pulsed laser ablation. *Optics Communications* **2004,** *242*, (1-3), 215-219.

103. Qin, W.; Cao, C.; Wang, L.; Zhang, J.; Zhang, D.; Zheng, K.; Wang, Y.; Wei, G.; Wang, G.; Zhu, P.; Kim, R., Ultraviolet upconversion fluorescence from ^6D_J of Gd^{3+} induced by 980 nm excitation. *Opt. Lett.* **2008,** *33*, (19), 2167-2169.

104. Cates, E. L.; Cho, M.; Kim, J.-H., Converting Visible Light into UVC: Microbial Inactivation by Pr^{3+}-Activated Upconversion Materials. *Environmental Science & Technology* **2011,** *45*, (8), 3680-3686.

105. de Wild, J.; Rath, J. K.; Meijerink, A.; van Sark, W. G. J. H. M.; Schropp, R. E. I., Enhanced near-infrared response of a-Si:H solar cells with β-$NaYF_4$:Yb^{3+} (18%), Er^{3+}

(2%) upconversion phosphors. *Solar Energy Materials and Solar Cells* **2010,** *94*, (12), 2395-2398.

106. Fischer, S.; Goldschmidt, J. C.; Loper, P.; Bauer, G. H.; Bruggemann, R.; Kramer, K.; Biner, D.; Hermle, M.; Glunz, S. W., Enhancement of silicon solar cell efficiency by upconversion: Optical and electrical characterization. *Journal of Applied Physics* **2010,** *108*, (4), 044912-11.

107. Baluschev, S.; Yakutkin, V.; Miteva, T.; Wegner, G.; Roberts, T.; Nelles, G.; Yasuda, A.; Chernov, S.; Aleshchenkov, S.; Cheprakov, A., A general approach for non-coherently excited annihilation up-conversion: transforming the solar-spectrum. *New Journal of Physics* **2008,** *10*, (1), 013007.

108. Bradsher, K., China, citing errors, vows to overhaul rare earth industry. *The New York Times* June 21, 2012, 2012.

109. Ende, B. M. v. d.; Aarts, L.; Meijerink, A., Lanthanide ions as spectral converters for solar cells. *Physical Chemistry Chemical Physics* **2009,** *11*, (47), 11081-11095.

110. Yamaguchi, M., III–V compound multi-junction solar cells: present and future. *Solar Energy Materials and Solar Cells* **2003,** *75*, (1–2), 261-269.

111. Kim, J.; Lee, C. W.; Choi, W., Platinized WO_3 as an Environmental Photocatalyst that Generates OH Radicals under Visible Light. *Environmental Science & Technology* **2010,** *44*, (17), 6849-6854.

112. Zhang, Z.; Wang, W.; Wang, L.; Sun, S., Enhancement of Visible-Light Photocatalysis by Coupling with Narrow-Band-Gap Semiconductor: A Case Study on Bi_2S_3/Bi_2WO_6. *ACS Applied Materials & Interfaces* **2012,** *4*, (2), 593-597.

113. Zhou, T.; Hu, J.; Li, J., Er3+ doped bismuth molybdate nanosheets with exposed {01 0} facets and enhanced photocatalytic performance. *Applied Catalysis B: Environmental* **2011,** *110*, (0), 221-230.

114. Asahi, R.; Morikawa, T.; Ohwaki, T.; Aoki, K.; Taga, Y., Visible-Light Photocatalysis in Nitrogen-Doped Titanium Oxides. *Science* **2001,** *293*, (5528), 269-271.

115. Sato, S., Photocatalytic activity of NO_x-doped TiO_2 in the visible light region. *Chemical Physics Letters* **1986,** *123*, (1–2), 126-128.

116. Burda, C.; Lou, Y.; Chen, X.; Samia, A. C. S.; Stout, J.; Gole, J. L., Enhanced Nitrogen Doping in TiO_2 Nanoparticles. *Nano Letters* **2003,** *3*, (8), 1049-1051.

117. Wang, J.; Tafen, D. N.; Lewis, J. P.; Hong, Z.; Manivannan, A.; Zhi, M.; Li, M.; Wu, N., Origin of Photocatalytic Activity of Nitrogen-Doped TiO_2 Nanobelts. *Journal of the American Chemical Society* **2009,** *131*, (34), 12290-12297.

118. Wu, G.; Nishikawa, T.; Ohtani, B.; Chen, A., Synthesis and Characterization of Carbon-Doped TiO2 Nanostructures with Enhanced Visible Light Response. *Chemistry of Materials* **2007,** *19*, (18), 4530-4537.

119. Yu, J. C.; Ho, W.; Yu, J.; Yip, H.; Wong, P. K.; Zhao, J., Efficient Visible-Light-Induced Photocatalytic Disinfection on Sulfur-Doped Nanocrystalline Titania. *Environmental Science & Technology* **2005,** *39*, (4), 1175-1179.

120. Chen, X.; Burda, C., The Electronic Origin of the Visible-Light Absorption Properties of C-, N- and S-Doped TiO_2 Nanomaterials. *Journal of the American Chemical Society* **2008,** *130*, (15), 5018-5019.

121. Huo, Y. N.; Yang, X. L.; Zhu, J.; Li, H. X., Highly active and stable CdS-TiO(2) visible photocatalyst prepared by in situ sulfurization under supercritical conditions. *Appl. Catal. B-Environ.* **2011,** *106*, (1-2), 69-75.

122. Cho, Y.; Choi, W.; Lee, C.-H.; Hyeon, T.; Lee, H.-I., Visible Light-Induced Degradation of Carbon Tetrachloride on Dye-Sensitized TiO_2. *Environmental Science & Technology* **2001,** *35*, (5), 966-970.

123. Bae, E.; Choi, W., Highly Enhanced Photoreductive Degradation of Perchlorinated Compounds on Dye-Sensitized Metal/TiO_2 under Visible Light. *Environmental Science & Technology* **2002,** *37*, (1), 147-152.

124. Mrowetz, M.; Balcerski, W.; Colussi, A. J.; Hoffmann, M. R., Oxidative Power of Nitrogen-Doped TiO_2 Photocatalysts under Visible Illumination. *The Journal of Physical Chemistry B* **2004,** *108*, (45), 17269-17273.

125. Grätzel, M., Dye-sensitized solar cells. *Journal of Photochemistry and Photobiology C: Photochemistry Reviews* **2003,** *4*, (2), 145-153.

126. Ashwin, C. A.; Aitzol, G.-E.; Hadiseh, A.; Jennifer, A. D., Toward high-efficiency solar upconversion with plasmonic nanostructures. *Journal of Optics* **2012,** *14*, (2), 024008.

127. Trupke, T.; Green, M. A.; Wurfel, P., Improving solar cell efficiencies by up-conversion of sub-band-gap light. *Journal of Applied Physics* **2002,** *92*, (7), 4117-4122.

128. Shockley, W.; Queisser, H. J., Detailed Balance Limit of Efficiency of p-n Junction Solar Cells. *Journal of Applied Physics* **1961,** *32*, (3), 510-519.

129. Chen, S.; Zhou, G.; Su, F.; Zhang, H.; Wang, L.; Wu, M.; Chen, M.; Pan, L.; Wang, S., Power conversion efficiency enhancement in silicon solar cell from solution processed transparent upconversion film. *Materials Letters* **2012,** *77*, (0), 17-20.

130. Chen, Y.; He, W.; Jiao, Y.; Wang, H.; Hao, X.; Lu, J.; Yang, S.-e., β-$NaYF_4$:Er^{3+}(10%) microprisms for the enhancement of a-Si:H solar cell near-infrared responses. *Journal of Luminescence* **2012,** *132*, (9), 2247-2250.

131. Goldschmidt, J. C.; Fischer, S.; Löper, P.; Krämer, K. W.; Biner, D.; Hermle, M.; Glunz, S. W., Experimental analysis of upconversion with both coherent monochromatic irradiation and broad spectrum illumination. *Solar Energy Materials and Solar Cells* **2011,** *95*, (7), 1960-1963.

132. Shalav, A.; Richards, B. S.; Green, M. A., Luminescent layers for enhanced silicon solar cell performance: Up-conversion. *Solar Energy Materials and Solar Cells* **2007,** *91*, (9), 829-842.

133. Shalav, A.; Richards, B. S.; Trupke, T.; Kramer, K. W.; Gudel, H. U., Application of $NaYF_4$:Er^{3+} up-converting phosphors for enhanced near-infrared silicon solar cell response. *Applied Physics Letters* **2005,** *86*, (1), 013505-3.

134. Gibart, P.; Auzel, F.; Guillaume, J. C.; Zahraman, K., Below band-gap IR response of substrate-free GaAs solar cells using two-photon up-conversion. *Jpn. J. Appl. Phys. Part 1 - Regul. Pap. Short Notes Rev. Pap.* **1996,** *35*, (8), 4401-4402.

135. Li, Z. Q.; Li, X. D.; Liu, Q. Q.; Chen, X. H.; Sun, Z.; Liu, C.; Ye, X. J.; Huang, S. M., Core/shell structured $NaYF_4$:Yb^{3+} /Er^{3+} /Gd^{+3} nanorods with Au nanoparticles or shells for flexible amorphous silicon solar cells. *Nanotechnology* **2012,** *23*, (2), 025402.

136. Yuan, C.; Chen, G.; Prasad, P. N.; Ohulchanskyy, T. Y.; Ning, Z.; Tian, H.; Sun, L.; Agren, H., Use of colloidal upconversion nanocrystals for energy relay solar cell light harvesting in the near-infrared region. *Journal of Materials Chemistry* **2012,** *22*, (33), 16709-16713.

137. Wang, F.; Liu, X., Upconversion Multicolor Fine-Tuning: Visible to Near-Infrared Emission from Lanthanide-Doped $NaYF_4$ Nanoparticles. *Journal of the American Chemical Society* **2008,** *130*, (17), 5642-5643.

138. Bernd Ahrens; Philipp Löper; Jan Christoph Goldschmidt; Stefan Glunz; Bastian Henke; Paul-Tiberiu Miclea; Stefan Schweizer, Neodymium-doped fluorochlorozirconate glasses as an upconversion model system for high efficiency solar cells. *physica status solidi (a)* **2008,** *205*, (12), 2822-2830.

139. Schulze, T. F.; Cheng, Y. Y.; Fückel, B.; MacQueen, R. W.; Danos, A.; Davis, N. J. L. K.; Tayebjee, M. J. Y.; Khoury, T.; Clady, R. G. C. R.; Ekins-Daukes, N. J.; Crossley, M. J.; Stannowski, B.; Lips, K.; Schmidt, T. W., Photochemical Upconversion Enhanced Solar Cells: Effect of a Back Reflector. *Australian Journal of Chemistry* **2012,** *65*, (5), 480-485.

140. Wang, J.; Fu-yu, W. E. N.; Zhao-hong, Z.; Xiang-dong, Z.; Zhi-jun, P. A. N.; Lei, Z.; Lei, W.; Liang, X. U.; Ping-li, K.; Peng, Z., Degradation of dyestuff wastewater using visible light in the presence of a novel nano TiO_2; catalyst doped with upconversion luminescence agent. *Journal of Environmental Sciences* **2005,** *17*, (5), 727-730.

141. Feng, G.; Liu, S.; Xiu, Z.; Zhang, Y.; Yu, J.; Chen, Y.; Wang, P.; Yu, X., Visible Light Photocatalytic Activities of TiO_2 Nanocrystals Doped with Upconversion

Luminescence Agent. *The Journal of Physical Chemistry C* **2008,** *112*, (35), 13692-13699.

142. Zu, N.; Yang, H.; Dai, Z., Different processes responsible for blue pumped, ultraviolet and violet luminescence in high-concentrated Er^{3+}:YAG and low-concentrated Er^{3+}:YAP crystals. *Physica B: Condensed Matter* **2008,** *403*, (1), 174-177.

143. Xu, H.; Dai, Z.; Jiang, Z., Luminescence characteristics of ultraviolet upconversion from Er^{3+} :YAG crystal by Ar^{+} laser (488 nm) excitation. *The European Physical Journal D - Atomic, Molecular, Optical and Plasma Physics* **2001,** *17*, (1), 79-83.

144. Qin, W.; Zhang, D.; Zhao, D.; Wang, L.; Zheng, K., Near-infrared photocatalysis based on YF_3:Yb^{3+},Tm^{3+}/TiO_2 core/shell nanoparticles. *Chemical Communications* **2010,** *46*, (13), 2304-2306.

145. Li, Z.-X.; Shi, F.-B.; Zhang, T.; Wu, H.-S.; Sun, L.-D.; Yan, C.-H., Ytterbium stabilized ordered mesoporous titania for near-infrared photocatalysis. *Chemical Communications* **2011,** *47*, (28), 8109-8111.

146. Shannon, R. D.; Prewitt, C. T., Effective ionic radii in oxides and fluorides. *Acta Crystallographica Section B* **1969,** *25*, (5), 925-946.

147. Shi, J.; Ye, J.; Ma, L.; Ouyang, S.; Jing, D.; Guo, L., Site-Selected Doping of Upconversion Luminescent Er^{3+} into $SrTiO_3$ for Visible-Light-Driven Photocatalytic H_2 or O_2 Evolution. *Chemistry – A European Journal* **2012,** *18*, (24), 7543-7551.

148. Fan, N.; Chen, Y.; Feng, Q.; Wang, C.; Pan, K.; Zhou, W.; Li, Y.; Hou, H.; Wang, G., Enhanced photocatalytic activity and upconversion luminescence of flowerlike

hierarchical Bi_2MoO_6 microspheres by Er^{3+} doping. *Journal of Materials Research* **2012,** *27*, (11), 1471-1475.

149. Bingham, S.; Daoud, W. A., Recent advances in making nano-sized TiO_2 visible-light active through rare-earth metal doping. *Journal of Materials Chemistry* **2011,** *21*, (7), 2041-2050.

150. Zongyan, Z.; Qingju, L., Effects of lanthanide doping on electronic structures and optical properties of anatase TiO_2 from density functional theory calculations. *Journal of Physics D: Applied Physics* **2008,** *41*, (8), 085417.

151. Khnayzer, R. S.; Blumhoff, J.; Harrington, J. A.; Haefele, A.; Deng, F.; Castellano, F. N., Upconversion-powered photoelectrochemistry. *Chemical Communications* **2012,** *48*, (2), 209-211.

152. Kim, J.-H.; Kim, J.-H., Encapsulated Triplet–Triplet Annihilation-Based Upconversion in the Aqueous Phase for Sub-Band-Gap Semiconductor Photocatalysis. *Journal of the American Chemical Society* **2012**.

153. Lu, Q.; Guo, F.; Sun, L.; Li, A., Surface Modification of ZrO_2:Er^{3+} Nanoparticles to Attenuate Aggregation and Enhance Upconversion Fluorescence. *The Journal of Physical Chemistry C* **2008,** *112*, (8), 2836-2844.

154. Schafer, H.; Ptacek, P.; Zerzouf, O.; Haase, M., Synthesis and Optical Properties of KYF_4/Yb, Er Nanocrystals, and their Surface Modification with Undoped KYF_4. *Adv. Funct. Mater.* **2008,** *18*, (19), 2913-2918.

155. Vetrone, F.; Naccache, R.; Mahalingam, V.; Morgan, C. G.; Capobianco, J. A., The Active-Core/Active-Shell Approach: A Strategy to Enhance the Upconversion

Luminescence in Lanthanide-Doped Nanoparticles. *Adv. Funct. Mater.* **2009,** *19*, (18), 2924-2929.

156. da Silva, D. M.; Kassab, L. R. P.; Luthi, S. R.; de Araujo, C. B.; Gomes, A. S. L.; Bell, M. J. V., Frequency upconversion in Er^{3+} doped PbO—GeO_2 glasses containing metallic nanoparticles. *Applied Physics Letters* **2007,** *90*, (8), 081913-3.

157. Rai, V. K.; Menezes, L. d. S.; de Araujo, C. B.; Kassab, L. R. P.; da Silva, D. M.; Kobayashi, R. A., Surface-plasmon-enhanced frequency upconversion in Pr^{3+} doped tellurium-oxide glasses containing silver nanoparticles. *Journal of Applied Physics* **2008,** *103*, (9), 093526-4.

158. Zhang, F.; Braun, G. B.; Shi, Y.; Zhang, Y.; Sun, X.; Reich, N. O.; Zhao, D.; Stucky, G., Fabrication of Ag@SiO_2@Y_2O_3:Er Nanostructures for Bioimaging: Tuning of the Upconversion Fluorescence with Silver Nanoparticles. *Journal of the American Chemical Society* **2010,** *132*, (9), 2850-2851.

159. Cates, E. L.; Wilkinson, A. P.; Kim, J.-H., Delineating Mechanisms of Upconversion Enhancement by Li^+ Codoping in Y_2SiO_5:Pr^{3+}. *The Journal of Physical Chemistry C* **2012,** *116*, (23), 12772-12778.

160. Chen, G.; Liu, H.; Liang, H.; Somesfalean, G.; Zhang, Z., Upconversion Emission Enhancement in Yb^{3+}/Er^{3+}-Codoped Y_2O_3 Nanocrystals by Tridoping with Li^+ Ions. *The Journal of Physical Chemistry C* **2008,** *112*, (31), 12030-12036.

161. Huang, Q.; Yu, J.; Ma, E.; Lin, K., Synthesis and Characterization of Highly Efficient Near-Infrared Upconversion Sc^{3+}/Er^{3+}/Yb^{3+} Tridoped $NaYF_4$. *The Journal of Physical Chemistry C* **2010,** *114*, (10), 4719-4724.

162. *Multi-Photon Phosphor Feasibility Research: Advanced Light Source Development*; EPRI, Palo Alto, CA, U.S. Department of Energy, Morgantown, WV, Osram Sylvania, Inc., Beverly, MA, 2003.

163. Hai-Gui, Y.; Zhen-Wen, D.; Zhi-Wei, S., Ultraviolet and visible upconversion dynamics in Er_{3+}:$YAlO_3$ under $^2H_{11/2}$ excitation. *Chinese Physics* **2006**, (6), 1273.

164. Cao, C.; Qin, W.; Zhang, J., Study on up-conversion emissions of Yb^{3+}/Tm^{3+} co-doped GdF_3 and $NaGdF_4$. *Optics Communications* **2010,** *283*, (4), 547-550.

165. Cao, C.; Qin, W.; Zhang, J.; Wang, Y.; Zhu, P.; Wei, G.; Wang, G.; Kim, R.; Wang, L., Ultraviolet upconversion emissions of Gd^{3+}. *Opt. Lett.* **2008,** *33*, (8), 857-859.

166. Zhang, J.; Cao, C.; Lu, S.; Qin, W.-p., Energy transition between Yb^{3+} - Tm^{3+} - Gd^{3+} in Gd^{3+}, Yb^{3+} and Tm^{3+} Co-doped fluoride nanocrystals. *Physics Procedia* **2011,** *13*, (0), 9-13.

167. Lee, L. S.; Rand, S. C.; Schawlow, A. L., Cooperative energy transfer among Pr3+ ions in LaF3. *Physical Review B* **1984,** *29*, (12), 6901.

168. Laroche, M.; Bettinelli, M.; Girard, S.; Moncorgé, R., f-d Luminescence of Pr^{3+} and Ce^{3+} in the chloro-elpasolite Cs_2NaYCl_6. *Chemical Physics Letters* **1999,** *311*, (3-4), 167-172.

169. Laroche, M.; Braud, A.; Girard, S.; Doualan, J. L.; Moncorge, R.; Thuau, M.; Merkle, L. D., Spectroscopic investigations of the 4f5d energy levels of Pr^{3+} in fluoride crystals by excited-state absorption and two-step excitation measurements. *J. Opt. Soc. Am. B* **1999,** *16*, (12), 2269-2277.

170. Nicolas, S.; Descroix, E.; Joubert, M. F.; Guyot, Y.; Laroche, M.; Moncorgé, R.; Abdulsabirov, R. Y.; Naumov, A. K.; Semashko, V. V.; Tkachuk, A. M.; Malinowski,

M., Potentiality of Pr^{3+}- and Pr^{3+}+Ce^{3+}-doped crystals for tunable UV upconversion lasers. *Optical Materials* **2003,** *22*, (2), 139-146.

171. Nicolas, S.; Laroche, M.; Girard, S.; Moncorge, R.; Guyot, Y.; Joubert, M. F.; Descroix, E.; Petrosyan, A. G., 4f2 to 4f5d excited state absorption in Pr^{3+}:$YAlO_3$. *Journal of Physics: Condensed Matter* **1999**, (40), 7937.

172. Hu, C.; Sun, C.; Li, J.; Li, Z.; Zhang, H.; Jiang, Z., Visible-to-ultraviolet upconversion in Pr^{3+}:Y_2SiO_5 crystals. *Chemical Physics* **2006,** *325*, (2-3), 563-566.

173. Sun, C. L.; Li, J. F.; Hu, C. H.; Jiang, H. M.; Jiang, Z. K., Ultraviolet upconversion in Pr^{3+}:Y_2SiO_5 crystal by Ar^+ laser (488 nm) excitation. *The European Physical Journal D - Atomic, Molecular, Optical and Plasma Physics* **2006,** *39*, (2), 303-306.

174. Diallo, P. T.; Boutinaud, P.; Mahiou, R.; Cousseins, J. C., Red Luminescence in Pr^{3+}-Doped Calcium Titanates. *physica status solidi (a)* **1997,** *160*, (1), 255-263.

175. Capobianco, J. A.; Raspa, N.; Monteil, A.; Malinowski, M., Energy transfer upconversion in $Gd_3Ga_5O_{12}$:Pr^{3+}. *Journal of Physics: Condensed Matter* **1993**, (33), 6083.

176. van der Kolk, E.; Dorenbos, P.; Vink, A. P.; Perego, R. C.; van Eijk, C. W. E.; Lakshmanan, A. R., Vacuum ultraviolet excitation and emission properties of Pr^{3+} and Ce^{3+} in MSO_4 (M=Ba, Sr, and Ca) and predicting quantum splitting by Pr^{3+} in oxides and fluorides. *Physical Review B* **2001,** *64*, (19), 195129.

177. Srivastava, A. M.; Doughty, D. A.; Beers, W. W., Photon Cascade Luminescence of Pr^{3+} in $LaMgB_5O_{10}$. *Journal of The Electrochemical Society* **1996,** *143*, (12), 4113-4116.

178. Masalov, A.; Viagin, O.; Ganina, I.; Malyukin, Y., Strong quenching of praseodymium f-f luminescence induced by a surface of $Y_2SiO_5:Pr^{3+}$ nanocrystal. *Journal of Luminescence* **2009,** *129*, (12), 1695-1697.

179. Hirai, T.; Yoshida, H.; Sakuragi, S.; Hashimoto, S.; Ohno, N., Transfer of Excitation Energy from Pr^{3+} to Gd^{3+} in $YF_3:Pr^{3+},Gd^{3+}$. *Jpn. J. Appl. Phys.* **2007,** *46*, 660-663.

180. Rativa, D. J.; Araujo, C. B. d.; Messaddeq, Y., Energy transfer and frequency upconversion involving triads of Pr^{3+} ions in Pr^{3+},Gd^{3+} doped fluoroindate glass. *Journal of Applied Physics* **2006,** *99*, (8), 083505.

181. Bai, Y.; Wang, Y.; Peng, G.; Yang, K.; Zhang, X.; Song, Y., Enhance upconversion photoluminescence intensity by doping Li^+ in Ho^{3+} and Yb^{3+} codoped Y_2O_3 nanocrystals. *Journal of Alloys and Compounds* **2009,** *478*, (1-2), 676-678.

182. Bai, Y.; Wang, Y.; Yang, K.; Zhang, X.; Peng, G.; Song, Y.; Pan, Z.; Wang, C. H., The Effect of Li on the Spectrum of Er^{3+} in Li- and Er-Codoped ZnO Nanocrystals. *The Journal of Physical Chemistry C* **2008,** *112*, (32), 12259-12263.

183. Byeon, S.-H.; Ko, M.-G.; Park, J.-C.; Kim, D.-K., Low-Temperature Crystallization and Highly Enhanced Photoluminescence of $Gd_{2-x}Y_xO_3:Eu^{3+}$ by Li Doping. *Chemistry of Materials* **2002,** *14*, (2), 603-608.

184. Cho, M.; Chung, H.; Yoon, J., Disinfection of Water Containing Natural Organic Matter by Using Ozone-Initiated Radical Reactions. *Appl. Environ. Microbiol.* **2003,** *69*, (4), 2284-2291.

185. Liang, H.; Chen, G.; Liu, H.; Zhang, Z., Ultraviolet upconversion luminescence enhancement in Yb^{3+}/Er^{3+}-codoped Y_2O_3 nanocrystals induced by tridoping with Li^+ ions. *Journal of Luminescence* **2009,** *129*, (3), 197-202.

186. Sun, L.; Qian, C.; Liao, C.; Wang, X.; Yan, C., Luminescent properties of Li^+ doped nanosized Y_2O_3:Eu. *Solid State Communications* **2001,** *119*, (6), 393-396.

187. Kang, H. S.; Kang, Y. C.; Park, H. D.; Shul, Y. G., Y_2SiO_5:Tb phosphor particles prepared from colloidal and aqueous solutions by spray pyrolysis. *Applied Physics A: Materials Science & Processing* **2005,** *80*, (2), 347-351.

188. Saha, S.; Chowdhury, P. S.; Patra, A., Luminescence of Ce^{3+} in Y_2SiO_5 Nanocrystals: Role of Crystal Structure and Crystal Size. *The Journal of Physical Chemistry B* **2005,** *109*, (7), 2699-2702.

189. De, G.; Qin, W.; Zhang, J.; Zhang, J.; Wang, Y.; Cao, C.; Cui, Y., Effect of OH- on the upconversion luminescent efficiency of Y_2O_3:Yb^{3+}, Er^{3+} nanostructures. *Solid State Communications* **2006,** *137*, (9), 483-487.

190. Li, C.; Liu, X.; Yang, P.; Zhang, C.; Lian, H.; Lin, J., LaF_3, CeF_3, CeF_3:Tb^{3+}, and CeF_3:Tb^{3+}@LaF_3 (Core-Shell) Nanoplates: Hydrothermal Synthesis and Luminescence Properties. *The Journal of Physical Chemistry C* **2008,** *112*, (8), 2904-2910.

191. Liang, H.; Zheng, Y.; Chen, G.; Wu, L.; Zhang, Z.; Cao, W., Enhancement of upconversion luminescence of Y_2O_3:Er^{3+} nanocrystals by codoping Li^+-Zn^{2+}. *Journal of Alloys and Compounds* **2011,** *509*, (2), 409-413.

192. Lin, J.; Su, Q.; Zhang, H.; Wang, S., Crystal structure dependence of the luminescence of rare earth ions (Ce^{3+}, Tb^{3+}, Sm^{3+}) in Y_2SiO_5. *Materials Research Bulletin* **1996,** *31*, (2), 189-196.

193. Craik, S. A.; Finch, G. R.; Bolton, J. R.; Belosevic, M., Inactivation of Giardia muris cysts using medium-pressure ultraviolet radiation in filtered drinking water. *Water Research* **2000,** *34*, (18), 4325-4332.

194. Brown, M. R. W.; Foster, J. H. S.; Clamp, J. R., Composition of Pseudomonas aeruginosa slime. *Biochemi. J.* **1969,** *112*, 521.

195. Pier, G. B.; Sidberry, H. F.; Zolyomi, S.; Sadoff, J. C., Isolation and characterization of a high-molecular-weight polysaccharide from the slime of Pseudomonas aeruginosa. *Infect. Immun.* **1978,** *22*, (3), 908-918.

196. Nicholson, W. L.; Galeano, B., UV Resistance of Bacillus anthracis Spores Revisited: Validation of Bacillus subtilis Spores as UV Surrogates for Spores of B. anthracis Sterne. *Appl. Environ. Microbiol.* **2003,** *69*, (2), 1327-1330.

197. Sun, Q.; Zhao, H.; Chen, X.; Wang, F.; Cai, W.; Jiang, Z., Upconversion emission enhancement in silica-coated Gd_2O_3:Tm^{3+}, Yb^{3+} nanocrystals by incorporation of Li^+ ion. *Materials Chemistry and Physics* **2010,** *123*, (2-3), 806-810.

198. Sun, Q.; Chen, X.; Liu, Z.; Wang, F.; Jiang, Z.; Wang, C., Enhancement of the upconversion luminescence intensity in Er^{3+} doped $BaTiO_3$ nanocrystals by codoping with Li^+ ions. *Journal of Alloys and Compounds* **2011,** *509*, (17), 5336-5340.

199. Sun, Z.; Zhou, Y.; Li, M., Effect of $LiYO_2$ on the synthesis and pressureless sintering of Y2SiO5. *Journal of Materials Research* **2008,** *23*, (03), 732-736.

200. Bae, J. S.; Park, S. S.; Hong, T. E.; Kim, J. P.; Yoon, J. H.; Jeong, E. D.; Won, M. S.; Jeong, J. H., Optical and surface analysis of lithium incorporated $GdVO_4$:Eu^{3+} phosphor powders. *Current Applied Physics* **2009,** *9*, (3, Supplement 1), S241-S244.

201. Chen, X.; Liu, Z.; Sun, Q.; Ye, M.; Wang, F., Upconversion emission enhancement in Er^{3+}/Yb^{3+}-codoped $BaTiO_3$ nanocrystals by tridoping with Li^+ ions. *Optics Communications* **2011,** *284*, (7), 2046-2049.

202. Liu, J.; Lian, H.; Shi, C., Improved optical photoluminescence by charge compensation in the phosphor system $CaMoO_4:Eu^{3+}$. *Optical Materials* **2007,** *29*, (12), 1591-1594.

203. Cao, B.; Feng, Z.; He, Y.; Li, H.; Dong, B., Opposite effect of Li^+ codoping on the upconversion emissions of Er^{3+}-doped TiO_2 powders. *Journal of Sol-Gel Science and Technology* **2010,** *54*, (1), 101-104.

204. He, X.; Guan, M.; Li, Z.; Shang, T.; Lian, N.; Zhou, Q., Enhancement of Fluorescence from $BaMoO_4:Pr^{3+}$ Deep-Red-Emitting Phosphor via Codoping Li^+ and Na^+ Ions. *Journal of the American Ceramic Society* **2011,** *94*, (8), 2483-2488.

205. Dhananjaya, N.; Nagabhushana, H.; Nagabhushana, B. M.; Rudraswamy, B.; Shivakumara, C.; Chakradhar, R. P. S., Effect of Li^+-ion on enhancement of photoluminescence in $Gd_2O_3:Eu^{3+}$ nanophosphors prepared by combustion technique. *Journal of Alloys and Compounds* **2011,** *509*, (5), 2368-2374.

206. Larson, A. C.; Von Dreele, R. B. *General structure analysis system (GSAS)*; LAUR 86-748; 1994.

207. Toby, B. H., EXPGUI, a graphical user interface for GSAS. *J. Appl. Cryst.* **2001,** *34*, 210-213.

208. Maksimov, B. A.; Ilyukhin, V. V.; Khariton; Belov, N. V., Crystal structure of yttrium oxyorthosilicate, Y_2O_3 SiO_2=Y_2SiO_5: Dual function of yttrium. *Soviet Physics Crystallography* **1971,** *15*, 806.

209. Wang, J.; Tian, S.; Li, G.; Liao, F.; Jing, X., Preparation and X-ray characterization of low-temperature phases of R_2SiO_5 (R = rare earth elements). *Materials Research Bulletin* **2001,** *36*, (10), 1855-1861.

210. Finger, L. W.; Kroeker, M.; Toby, B. H., DRAWxtl, an open-source computer program to produce crystal structure drawings. *J. Appl. Cryst.* **2007,** *40*, 188-192.

211. Felsche, J., The crystal chemistry of the rare-earth silicates. *Rare Earths* **1973,** *13*, 104-112.

212. Lin, J.; Su, Q.; Wang, S.; Zhang, H., Influence of crystal structure on the luminescence properties of bismuth(III), europium(III) and dysprosium(III) in Y_2SiO_5. *Journal of Materials Chemistry* **1996,** *6*, (2), 265-269.

213. Malyukin, Y.; Minkov, B.; Borisov, R.; Seminozhenko, V.; Znamenskii, N.; Manykin, E.; Marchenko, D.; Petrenko, E., - Low-temperature spectroscopy of nonequivalent Pr^{3+} optical centers in a Y_2SiO_5 crystal. *Low Temperature Physics* **1998,** - *24*, (- 6).

214. Malyukin, Y. V.; Zhmurin, P. N.; Grinev, B. V.; Seminozhenko, V. P.; Znamenskii, N. V.; Manykin, E. A.; Petrenko, E. A.; Yukina, T. G., Microscopic nature of Pr^{3+} optical centers in Y_2SiO_5, Lu_2SiO_5, and Gd_2SiO_5 crystals. *Low Temperature Physics* **2002,** *28*, (10), 774-779.

215. Hegarty, J.; Huber, D. L.; Yen, W. M., Fluorescence quenching by cross relaxation in LaF_3:Pr^{3+}. *Physical Review B* **1982,** *25*, (9), 5638.

216. Yang, M.; Sui, Y.; Wang, S.; Wang, X.; Sheng, Y.; Zhang, Z.; Lü, T.; Liu, W., Enhancement of upconversion emission in $Y_3Al_5O_{12}$:Er^{3+} induced by Li^+ doping at interstitial sites. *Chemical Physics Letters* **2010,** *492*, (1-3), 40-43.

217. Malyukin, Y. V.; Masalov, A. A.; Zhmurin, P. N.; Znamenskii, N. V.; Petrenko, E. A.; Yukina, T. G., Two mechanisms of $^1D_2$ fluorescence quenching of Pr^{3+}-doped Y_2SiO_5 crystal. *physica status solidi (b)* **2003,** *240*, (3), 655-662.

218. Liao, M.; Qin, G.; Yan, X.; Hughes, M.; Suzuki, T.; Ohishi, Y., Evaluating upconversion materials developed to improve the efficiency of solar cells: comment. *J. Opt. Soc. Am. B* **2010,** *27*, (7), 1352-1355.

219. Trupke, T.; Shalav, A.; Richards, B. S.; Würfel, P.; Green, M. A., Efficiency enhancement of solar cells by luminescent up-conversion of sunlight. *Solar Energy Materials and Solar Cells* **2006,** *90*, (18-19), 3327-3338.

220. Tian, W.; Rami Reddy, B., Ultraviolet upconversion in thulium-doped fluorozirconate fiber observed under two-color excitation. *Opt. Lett.* **2001,** *26*, (20), 1580-1582.

221. Krämer, K. W.; Güdel, H. U.; Schwartz, R. N., NIR to VIS upconversion in $LaCl_3$: 1% Er^{3+}: One- and two-color excitations around 1000 and 800 nm. *Journal of Alloys and Compounds* **1998,** *275–277*, (0), 191-195.

222. Bai, X.; Song, H.; Pan, G.; Lei, Y.; Wang, T.; Ren, X.; Lu, S.; Dong, B.; Dai, Q.; Fan, L., Size-Dependent Upconversion Luminescence in Er^{3+}/Yb^{3+}-Codoped Nanocrystalline Yttria: Saturation and Thermal Effects. *The Journal of Physical Chemistry C* **2007,** *111*, (36), 13611-13617.

223. Blatchley, E.; Meeusen, A.; Aronson, A.; Brewster, L., Inactivation of Bacillus Spores by Ultraviolet or Gamma Radiation. *Journal of Environmental Engineering* **2005,** *131*, (9), 1245-1252.

224. Kaminskii, A. A.; Bagayev, S. N.; Ueda, K.; Dong, J.; Eichler, H. J., New passively Q-switched LD-pumped self-Raman laser with single-step cascade SE → SRS wavelength conversion on the base of monoclinic Nd^{3+}:Y_2SiO_5 crystal. *Laser Physics Letters* **2010,** *7*, (4), 270-279.

225. Johnson, A. R.; Lee, S.-J.; Klein, J.; Kanicki, J., Absolute photoluminescence quantum efficiency measurement of light-emitting thin films. *Review of Scientific Instruments* **2007,** *78*, (9), 096101-3.

226. Passuello, T.; Piccinelli, F.; Trevisani, M.; Giarola, M.; Mariotto, G.; Marciniak, L.; Hreniak, D.; Guzik, M.; Fasoli, M.; Vedda, A.; Jary, V.; Nikl, M.; Causin, V.; Bettinelli, M.; Speghini, A., Structural and optical properties of Vernier phase lutetium oxyfluorides doped with lanthanide ions: interesting candidates as scintillators and X-ray phosphors. *Journal of Materials Chemistry* **2012**.

227. De Mello Donegá, C.; Meijerink, A.; Blasse, G., Non-radiative relaxation processes of the Pr^{3+} ion in solids. *Journal of Physics and Chemistry of Solids* **1995,** *56*, (5), 673-685.

228. Chen, D.; Wang, Y.; Zheng, K.; Guo, T.; Yu, Y.; Huang, P., Bright upconversion white light emission in transparent glass ceramic embedding Tm^{3+} Er^{3+} Yb^{3+} YF_3 nanocrystals. *Applied Physics Letters* **2007,** *91*, (25), 251903-251903-3.

229. Fu, Z.; Cui, X.; Cui, S.; Qi, X.; Zhou, S.; Zhang, S.; Jeong, J. H., Uniform Eu^{3+}-doped YF_3 microcrystals: inorganic salt-controlled synthesis and their luminescent properties. *CrystEngComm* **2012,** *14*, (11), 3915-3922.

230. Ma, M.; Xu, C.; Yang, L.; Ren, G.; Lin, J.; Yang, Q., Intense ultraviolet and blue upconversion emissions in Yb^{3+}–Tm^{3+} codoped stoichiometric $Y_7O_6F_9$ powder. *Physica B: Condensed Matter* **2011,** *406*, (17), 3256-3260.

231. Pang, T.; Cao, W.; Xing, M.; Feng, W.; Xu, S., Blue and white upconversion emissions of rare-earth ions-doped oxyfluoride phosphors. *Physica B: Condensed Matter* **2010,** *405*, (9), 2216-2219.

232. Park, S.; Vogt, T., Defect Monitoring and Substitutions in $Sr_{3-x}A_xAlO_4F$ (A = Ca, Ba) Oxyfluoride Host Lattices and Phosphors. *The Journal of Physical Chemistry C* **2010,** *114*, (26), 11576-11583.

233. Wang, J.; Lin, J.; Wu, J.; Huang, M.; Lan, Z.; Chen, Y.; Tang, S.; Fan, L.; Huang, Y., Application of Yb^{3+}, Er^{3+}-doped yttrium oxyfluoride nanocrystals in dye-sensitized solar cells. *Electrochimica Acta* **2012,** *70*, (0), 131-135.

234. Yang, R.; Qin, G.; Zhao, D.; Zheng, K.; Qin, W., Synthesis and upconversion properties of Ln^{3+} doped YOF nanofibers. *Journal of Fluorine Chemistry* **2012,** *140*, (0), 38-42.

235. Grzyb, T.; Lis, S., Structural and Spectroscopic Properties of LaOF:Eu^{3+} Nanocrystals Prepared by the Sol–Gel Pechini Method. *Inorganic Chemistry* **2011,** *50*, (17), 8112-8120.

236. Armelao, L.; Bottaro, G.; Bruno, G.; Losurdo, M.; Pascolini, M.; Soini, E.; Tondello, E., Lanthanum Oxyfluoride Sol−gel Thin Films by a Simple Single-Source Precursor Route. *The Journal of Physical Chemistry C* **2008,** *112*, (37), 14508-14512.

237. Zachariasen, W., Crystal chemical studies of the 5f-series of elements. XIV. Oxyfluorides, XOF. *Acta Crystallographica* **1951,** *4*, (3), 231-236.

238. Mann, A. W.; Bevan, D. J. M., Intermediate fluorite-related phases in the $Y_2O_3 \cdot YF_3$ system—Examples of one-dimensional ordered intergrowth. *Journal of Solid State Chemistry* **1972,** *5*, (3), 410-418.

239. Müller, J. H.; Petzel, T.; Hormann, B., Phase study of the binary system $Lu_2O_3 \cdot LuF_3$ in the temperature range 1000–1750 K. *Thermochimica Acta* **1997,** *298*, (1–2), 109-114.

240. Mann, A. W.; Bevan, D. J. M., The crystal structure of stoichiometric yttrium oxyfluoride, YOF. *Acta Crystallographica Section B* **1970,** *26*, (12), 2129-2131.

241. Wen, T.; Luo, W.; Wang, Y.; Zhang, M.; Guo, Y.; Yuan, J.; Ju, J.; Wang, Y.; Liao, F.; Yang, B., Multicolour and up-conversion fluorescence of lanthanide doped Vernier phase yttrium oxyfluoride nanocrystals. *Journal of Materials Chemistry C* **2013**.

242. Schmid, S., The Yttrium Oxide Fluoride Solid Solution Described as a Composite Modulated System. *Acta Crystallographica Section B* **1998,** *54*, (4), 391-398.

243. Karbowiak, M.; Mech, A.; Bednarkiewicz, A.; Strek, W., Synthesis and properties of solution-processed Eu^{3+}:BaY_2F_8. *Journal of Luminescence* **2005,** *114*, (1), 1-8.

244. Karbowiak, M.; Mech, A.; Bednarkiewicz, A.; Stręk, W., Structural and luminescent properties of nanostructured $KGdF_4$:Eu^{3+} synthesised by coprecipitation method. *Journal of Alloys and Compounds* **2004,** *380*, (1–2), 321-326.

245. Solar Water Disinfection. In Swiss Federal Institute for Aquatic Science and Technology: Dubendorf, Switzerland, 2008, <www.sodis.ch> accessed 5/15/2009.

246. Kapuscinski, R. B.; Mitchell, R., Solar radiation induces sublethal injury in Escherichia coli in seawater. *Appl. Environ. Microbiol.* **1981,** *41*, (3), 670-674.

247. Sinton, L. W.; Hall, C. H.; Lynch, P. A.; Davies-Colley, R. J., Sunlight Inactivation of Fecal Indicator Bacteria and Bacteriophages from Waste Stabilization Pond Effluent in Fresh and Saline Waters. *Appl. Environ. Microbiol.* **2002,** *68*, (3), 1122-1131.

248. Maclean, M.; MacGregor, S. J.; Anderson, J. G.; Woolsey, G. A.; Coia, J. E.; Hamilton, K.; Taggart, I.; Watson, S. B.; Thakker, B.; Gettinby, G., Environmental decontamination of a hospital isolation room using high-intensity narrow-spectrum light. *Journal of Hospital Infection 76*, (3), 247-251.